COMPUTATIONAL OPTICAL COHERENCE TOMOGRAPHY FOR POLARIZATION-SENSITIVE IMAGING, ABERRATION CORRECTION, AND WAVEFRONT MEASUREMENT

BY

FREDRICK A. SOUTH

DISSERTATION

Submitted in partial fulfillment of the requirements
for the degree of Doctor of Philosophy in Electrical and Computer Engineering
in the Graduate College of the
University of Illinois at Urbana-Champaign, 2018

Urbana, Illinois

Doctoral Committee:

Professor Stephen A. Boppart, Chair
Adjunct Professor P. Scott Carney
Professor J. Gary Eden
Assistant Professor Liang Gao

ABSTRACT

In this thesis, multiple longstanding challenges in optical imaging are solved by the development of new computational imaging methods, where computational imaging does not simply refer to simulation or modeling, but to the entirety of an imaging technology in which significant computation is required to achieve the final image. Of the many optical imaging technologies currently in use, optical coherence tomography (OCT) is distinctive in that it provides coherent measurement of optical scattering within bulk biological tissue. Unfortunately, the optical wavefront is often distorted by defocus and aberration, from either the imaging system or the sample itself, leading to poor image quality. Through a careful consideration of the optical theory and imaging hardware, computational imaging methods can correct these distortions through creative data acquisition and processing schemes. Here, new computational OCT methods are developed from theory to implementation to address three related challenges in optical imaging. First, computational OCT is extended to polarization-sensitive imaging. This provides the improved resolution and imaging depth of computational OCT with the enhanced contrast of polarization-sensitive imaging. Second, computational OCT is combined with hardware-based wavefront correction. This addresses the low signal-to-noise ratio (SNR) limitation of computational OCT and provides improved performance beyond that of hardware-only correction. Lastly, distortion of the optical wavefront is computationally measured directly from the OCT data. This enables both measurement and correction of the optical wavefront throughout biological samples without additional hardware. Together, these results demonstrate the usefulness of computational OCT across a broad range of important imaging scenarios in biology and medicine.

Whatever you do, work heartily, as for the Lord and not for men

- Colossians 3:23

ACKNOWLEDGMENTS

This thesis is the fruit of several years of dedicated work, not only from myself, but also many dear friends and collaborators. Most importantly, Professor Stephen Boppart has been steadfast in his intellectual, financial, and emotional support throughout these years. He has provided me with all the resources I needed to pursue the research topics that I found most interesting, and saw potential in me that I myself did not see.

To that point, I began my graduate studies with little knowledge in optics. Thanks to Professors Scott Carney and Gabriel Popescu for shaping my understanding of optics and building the intellectual foundation upon which this thesis is built; and to Steven Adie who was my mentor throughout my Master's thesis work and helped me translate my knowledge from the textbook to the lab. I also began with very little knowledge in biology. Thanks to Marina Marjanovic and Eric Chaney for educating me in the relevant biological systems and lab work.

Deepest gratitude to my wife and best friend, Kayla, for her support throughout these seven years of graduate work. Thanks for being understanding through all the late nights of work, brewing me hot tea, reading books to me while I worked in the lab, and picking up the slack around the house when I was bogged down with research. She sacrificed much so that I could attend graduate school.

My family has been steadfast in their support throughout my entire life and have permanently shaped my character. My grandfather passed on his love of learning new things to me through many summer work projects. Special thanks to my father, who did anything he could to guarantee my success, regardless of cost to himself. He taught me to roll with the punches, accept failure, and keep pressing on, which are perhaps the most important factors in my completion of the PhD.

Table of Contents

1   INTRODUCTION

1.1   Optical imaging

Since the invention of the microscope in the sixteenth century, light microscopy has become an integral component of both science and medicine [1]. A well-known example is the use of histology in medical diagnosis. Amazingly, new breakthroughs are continually being made in optical imaging, despite its age. Multiple Nobel Prizes have been awarded for developments in microscopy, including the 1953 Nobel Prize in Physics for phase contrast microscopy, the 2008 Nobel Prize in Chemistry for discovery of the green fluorescent protein, and the 2014 Nobel Prize in Chemistry for super resolution imaging. In addition to these breakthroughs, other developments such as confocal microscopy, multiphoton microscopy, quantitative phase imaging, optical coherence tomography, and photoacoustic imaging have opened new fields of research.

Optical coherence tomography (OCT) provides real-time, three-dimensional (3D) images of scattering objects, including biological tissues [2,3]. OCT is a ranging technique, similar to ultrasound, and provides resolution on the scale of microns. However, a direct time-of-flight measurement is not feasible due to the high speed of light relative to the size scales within biological tissue. Therefore, the ranging measurement is performed using interferometry. By performing the ranging measurement across multiple locations, a 3D image of optical backscattering can be generated.

Of the many new optical imaging technologies, OCT is perhaps the most commercially successful. OCT holds approximately 60% market share in the clinical optical imaging market, with the OCT market size estimated to exceed $1 billion by 2019 [4,5]. In particular, ophthalmic OCT is a

substantial market with great humanitarian significance. As stated by OCT pioneer Dr. Carmen Puliafito, "OCT has revolutionized the treatment of eye diseases on a global basis and it is now routinely used to make clinical decisions about treating patients with blinding diseases such as macular degeneration, diabetic retinopathy, and glaucoma [6]."

In addition to becoming the standard of care in ophthalmology, OCT has been developed for application in cardiovascular, gastroesophageal, and cancer imaging [7–9]. It has also found application beyond the medical field, in areas such as metrology, non-destructive testing, microfluidics, and others [10]. A timeline showing the rapid increase in funding and applications of OCT is shown in Figure 1.1.
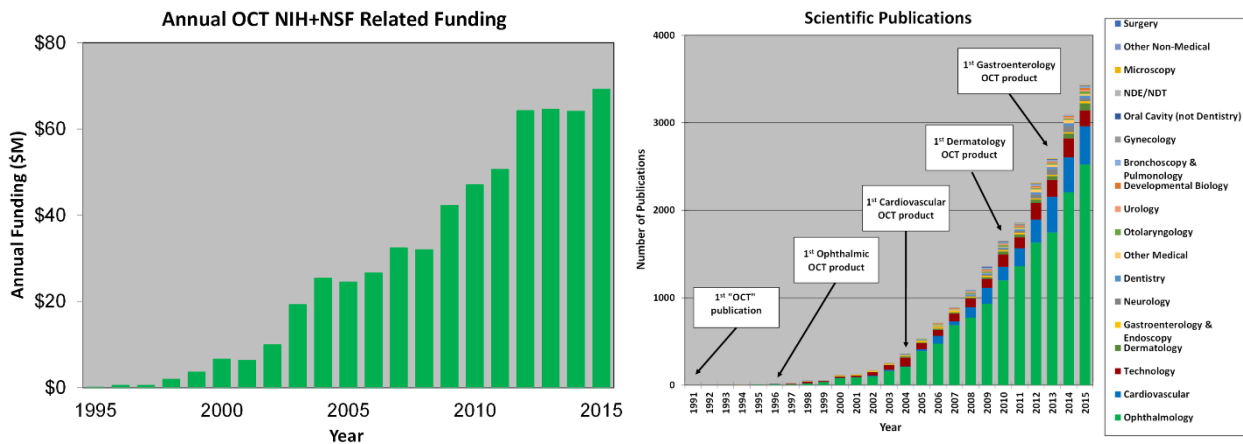
Figure 1.1. Progress in OCT. Government funding and commercialization to new applications has increased dramatically since the invention of OCT. Adapted from [3].

Much of the work in this thesis is applicable to interferometric imaging methods in general. However, the work has been thoroughly developed for OCT due to its power to generate 3D images for many biologically and medically important applications.

1.2 Computational optical imaging

Computational imaging refers to methods where computation plays an integral role in the image formation process [11]. Following a historical trend seen in other modalities, optical imaging is becoming increasingly computational. Historical precedents include the evolution of X-ray projections into computed tomography [12,13], nuclear magnetic resonance into magnetic resonance imaging [14], and radar imaging into synthetic aperture radar (SAR) [15,16]. These computational optical imaging methods have recently become capable of reconstructing *in vivo* data, providing high-resolution aberration-free imaging of living biological tissues beyond what was previously achievable by standard OCT imaging alone [17,18].

The use of computational imaging techniques has been inspired by two inherent limitations ubiquitous in optical imaging—restricted depth-of-field and wavefront aberrations. Limited depth-of-field reduces the usable imaging range, while optical aberrations of both the imaging system and the sample itself limit the achievable resolution and signal-to-noise ratio (SNR). Various hardware solutions have been proposed to overcome these challenges. In particular, the trade-off between resolution and depth-of-field has been addressed in hardware by focus shifting [19] and multiple beam imaging [20]. Alternatively, a non-Gaussian imaging beam, such as a Bessel beam, can be used to extend the depth-of-field [21,22]. Inspired by developments in astronomy [23,24], hardware adaptive optics (HAO) has been used to correct aberrations in microscopy through the use of a wavefront sensor and deformable mirror to sense and negate wavefront distortions [25-27]. However, HAO systems have not seen widespread use due to their inherent cost and complexity.

It is desirable to achieve high-resolution, aberration-free volumetric imaging without the need for additional hardware. Interferometric detection provides access to both the amplitude and the phase

of the backscattered light. Access to this phase information provides computational control of the full complex wavefront, enabling refocusing and correction of higher-order optical aberrations. Computational depth-of-field solutions include numerical refocusing [28–30], depth-encoded synthetic aperture microscopy [31,32], holoscopy [33,34], and interferometric synthetic aperture microscopy [35]. Aberration correction can also be performed through manipulation of the spatial frequency data. This has been previously achieved in digital holographic microscopy for imaging of thin samples [36,37], and recently in thick tissue samples using computational adaptive optics [38,39].

Interferometric synthetic aperture microscopy (ISAM) is a solution to the inverse problem for optical microscopy that provides depth-independent transverse resolution, overcoming the traditional depth-of-field limitation without the need for additional hardware [35,40–42]. ISAM reconstruction achieves this through a Fourier domain resampling which provides 3D defocus correction. ISAM is a point-scanning method, which avoids the cross-talk artifacts inherent in related full-field techniques [30,34,43]. It has been shown to be robust with respect to motion through the use of high scanning speeds or motion correction algorithms, and is parallelizable for real-time processing on a graphics processing unit (GPU) [17,44]. Together, these features have contributed to the successful *in vivo* application of the ISAM technique.

Computational adaptive optics (CAO) extends the ISAM model to include optical aberrations which can be corrected through manipulation of the complex interferometric data [38]. This is achieved by multiplication with a phase-only aberration correction filter which negates the wavefront aberrations. In this way, volumetric aberration-free imaging can be achieved. This flexible processing method can be used to correct for arbitrary aberrations of high order [45], and can be optimized for selected sample regions to overcome spatially varying aberrations [46]. CAO

has recently been applied to *in vivo* imaging of the human retina for visualization of the photoreceptor mosaic [18].

1.3   Challenges in computational OCT

It is the goal of this thesis to build upon the foundations of ISAM and CAO to develop new computational imaging methods that address remaining challenges in OCT imaging. Multiple challenges and the proposed strategies for addressing them are briefly summarized below. Appropriate background information for the new methods is covered in Chapter 2.

1.3.1   Polarization-sensitive imaging

Polarization-sensitive optical coherence tomography (PS-OCT) is a variation of OCT developed for imaging birefringent materials and biological tissue [47,48]. In addition to imaging the scattering structure, PS-OCT measures the polarization state of the backscattered light. Samples that exhibit birefringence will cause a change in the measured polarization state.

In biological tissues, form birefringence arises due to the organization of the tissue microenvironment, which provides insight into various biological processes. In particular, PS-OCT has been particularly valuable for imaging disease in birefringent tissues such as muscle, skin, the retina, arterial plaque, and collagen in the breast [49,50].

Like standard OCT imaging, PS-OCT suffers from poor transverse resolution outside the depth-of-field. This limits the resolution and usable imaging range. The standard PS-OCT model does not consider the nature of the focused imaging beam. By a comparison of the PS-OCT and ISAM models, a new reconstruction method was developed to provide the benefits of ISAM for

polarization-sensitive imaging. The new method, termed PS-ISAM, is described and demonstrated in Chapter 3.

1.3.2   Retinal imaging

Imaging the human retina requires imaging through the optics of the eye itself, which are highly aberrated when the pupil of the eye is large. By compensating for these aberrations, it is possible to achieve cellular level resolution. Both hardware adaptive optics (HAO) and CAO have been demonstrated in the human retina [18,51].

HAO physically modifies the optical wavefront using a deformable mirror to tightly focus the imaging beam onto the retina. This allows for high signal even in the presence of strong ocular aberrations. However, HAO typically updates its wavefront correction more slowly than the OCT volume is acquired, and the correction is limited to a single retinal depth. Therefore, image quality is not optimal for much of the acquired volume.

With CAO, the image formation process can continue after data acquisition, and therefore the data need not be aberration-free when acquired, decreasing the complexity of the imaging system. Additionally, the aberration correction can be fine-tuned for spatially and temporally varying aberrations. However, because CAO does not physically modify the wavefront, any signal lost due to the presence of aberrations cannot be recovered using CAO alone.

HAO and CAO were used together to address the shortcomings of each method, and to demonstrate how their strengths can be integrated to provide more complete correction of ocular aberrations and improved visualization of the cellular retinal features. Details of the implementation along with imaging results are presented in Chapter 4.

1.3.3 Aberration measurement

Measurement and correction of aberrations is an important step in achieving high-resolution images in optical microscopy [27]. To date, CAO has primarily been used for aberration correction to improve image resolution. However, it is also important to measure, or "sense," the aberrations to provide knowledge of the imaging system or even aberrations of the sample itself [52].

The appropriate CAO correction can be determined using a variety of methods. Regardless of which method is used, the computational wavefront correction corresponds to the double-pass system point spread function (PSF). In general, this is not identical to the single-pass aberration of the system. However, it may be possible to compute the true aberration from a measurement of the double-pass aberration.

To accomplish this task, the OCT forward model was explored for the case of an aberrated imaging pupil. A computational method was then developed to recover the single-pass aberration from the OCT data using CAO. Theoretical derivation, simulation, and experimental results are presented in Chapter 5.

2 BACKGROUND

2.1 Optical coherence tomography

OCT is a depth ranging imaging technique, where low coherence interferometry (LCI) is used to determine the depth range information. An LCI system is illustrated in Figure 2.1. In LCI, broadband near-infrared light is directed through a beam splitter into two paths known as the reference and sample arms which illuminate a reference mirror and the sample of interest, respectively. Recombining the reflected light from the reference and sample arms at the beam splitter results in an interference pattern that depends on the depth structure of the sample.
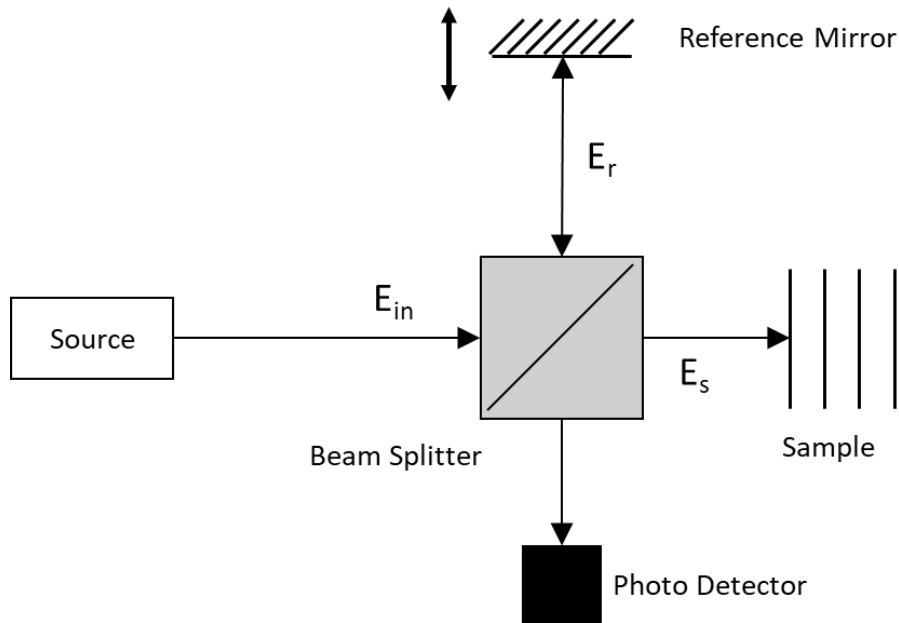
Figure 2.1. Illustration of a low coherence interferometer, the basic concept underlying OCT imaging.

The field at the output of the beam splitter, E_{out}, is the sum of the reflected reference and sample fields, E_R and E_S [53]. The intensity signal detected by the photodiode is given by

$$S = \left\langle E_0 E_0^* \right\rangle = \left\langle \left(E_R + E_S \right) \left(E_R + E_S \right)^* \right\rangle$$
$$= \left\langle E_R E_R^* \right\rangle + \left\langle E_S E_S^* \right\rangle + 2\,\mathrm{Re}\left\{ \left\langle E_R E_S^* \right\rangle \right\} \tag{2.1}$$

where the brackets denote time average. The first two terms in Eq. (2.1) account for autocorrelation

of the reference and sample fields respectively. The final term is the cross-correlation between the

reference and sample fields, and is the term of interest in OCT. Assuming identical illumination

of both sample and reference, for a given path delay $\tau = 2\Delta z / c$ between the reference and sample

arms, the cross-correlation term becomes

$$2\,\mathrm{Re}\left\{ \Gamma\left(\tau \right) \right\}, \tag{2.2}$$

where

$$\Gamma\left(\tau \right) = \left\langle E_R\left(t \right) E_R\left(t + \tau \right) \right\rangle \tag{2.3}$$

is the autocorrelation of the field.

Equation (2.3) can be considered the impulse response of the LCI system due to a perfect reflector.

Therefore, for an arbitrary sample structure the resulting OCT signal is proportional to the

convolution

$$\Gamma_{R,S}\left(\tau \right) = \Gamma\left(\tau \right) * h\left(\tau \right), \tag{2.4}$$

where the depth structure of the sample is encoded in $h(\tau)$. By scanning the reference arm distance,

τ is varied to measure the entire interference pattern. The incident beam is then scanned in two

dimensions over the surface of the sample, providing depth information at each transverse location

to construct 3D datasets.

This interference pattern may be detected in either the time-domain (TD-OCT) or Fourier-domain

(FD-OCT). FD-OCT is usually preferred due to increased SNR and acquisition speed. The FD-

OCT detection is performed by spectrally resolving the output signal using a grating and spectrometer instead of a single photodiode. Alternatively, the signal may be detected using a photodiode as the wavelength of the source is varied over time. This is known as swept-source OCT (SS-OCT). In either case the reference arm remains fixed for FD-OCT. For a perfect reflector in the sample arm, the intensity as a function of frequency ω is given by

$$S(\omega) = |P(\omega)|^2 + |P(\omega)|^2 |H(\omega)|^2 + 2|P(\omega)|^2 |H(\omega)| \cos(\phi(\Delta z)), \qquad (2.5)$$

where

$$\phi(\Delta z) = \omega(z_R - 2z_S)/c \qquad (2.6)$$

is the phase delay due to optical path length difference between the reference and sample arm positions z_R and z_S. The power spectrum of the source is given by $|P(\omega)|^2$ and the frequency response of the sample is $H(\omega)$. The first term can be easily measured and removed using background subtraction, while the second term is typically negligible. Assuming that the magnitude response of the sample arm is uniform over the measured frequencies, taking the Fourier transform of the third term leads to

$$\Gamma_{R,S}(\tau) = \Gamma(\tau) * \{\delta[(z_R - 2z_S)/c] + \delta[(z_R + 2z_S)/c]\}. \qquad (2.7)$$

This matches the result from Eq. (2.4) for a perfect reflector. The symmetry term is a result of the measurement containing only the real component in the frequency domain.

The axial point spread function of the OCT system is given by the auto-correlation of the source spectrum. Assuming a Gaussian spectrum, the full-width-half-max (FWHM) resolution of the auto-correlation function is given in [54] as

$$l_c = \frac{2\ln(2)}{\pi}\frac{\lambda_0{}^2}{\Delta\lambda},\tag{2.8}$$

where $\Delta\lambda$ is defined as the FWHM of the source spectrum. Therefore, an increase in bandwidth will result in an improved axial resolution. The typical axial resolution in OCT ranges from 1-10 µm. Transverse resolution is calculated independently from axial resolution in OCT. Light is focused onto the sample using a standard microscope objective. The transverse resolution is therefore given by Abbe's formula

$$\Delta x = 1.22\frac{\lambda_0}{2\text{NA}_{obj}},\tag{2.9}$$

where NA is the numerical aperture of the OCT microscope [53]. The typical transverse resolution in OCT ranges from approximately 5-20 µm.

Optical imaging of tissue is often performed using wavelengths in the near-infrared in what is known as the biological window. Components of biological tissue such as hemoglobin, melanin, and water are less absorbing in the near-infrared than in the visible range. Common wavelengths used in OCT imaging are 800 nm and 1300 nm, due to windows in the absorption spectra near these wavelengths. It has been shown that the attenuation in dense biological tissues is greater at 800 nm [55]. Therefore, imaging at 1300 nm is often preferred when imaging thick biological tissues such as the human breast. However, this comes with a loss of resolution, as indicated by Eq. (2.8). A wavelength of approximately 1050 nm is best suited for imaging the retina due to low absorption by the vitreous humor [56].

The maximum optical path length difference that can be measured in FD-OCT is determined by the number of points used to sample to spectrum [53]. Sampling the spectrum with N points will result in a maximum imaging range of

$$z_{max} = \frac{1}{4}\frac{\lambda_0}{\Delta\lambda}N.$$

(2.10)

While z_{max} can be several millimeters, or in some cases centimeters, the imaging depth into tissue is limited by multiple scattering to 1-3 mm beneath the surface.
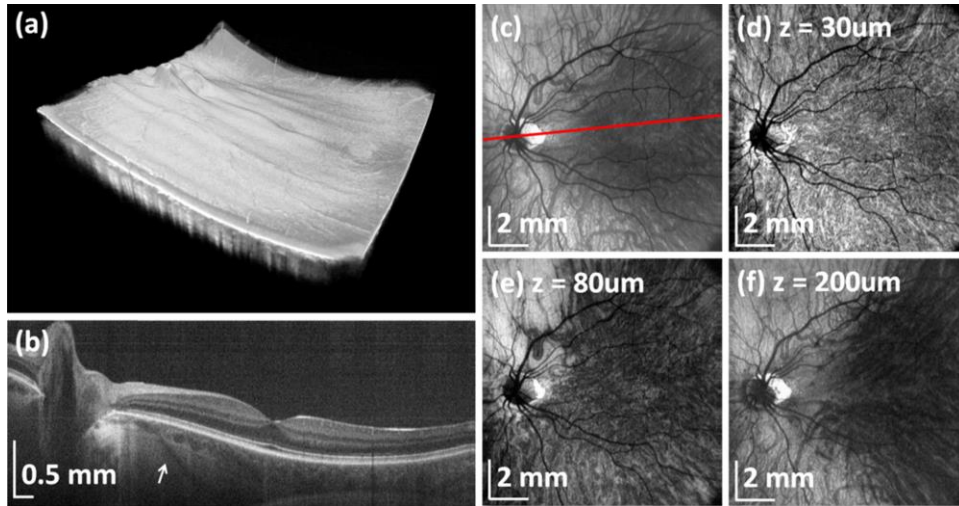
Figure 2.2. OCT dataset of the living human retina. (a) Rendering of volumetric wide-field 3D-OCT data. (b) Virtual (arbitrary) cross-sectional image showing deep image penetration and ability to visualize choroid and sclera. Arrow indicates scleral vessel. (c) *En face* OCT image of the choroid obtained by integrating signal below the retinal pigment epithelium (RPE). Red line indicates orientation of cross section in (b). *En face* OCT images at depths (d) 30, (e) 80, and (f) 200 μm below the RPE showing choroidal layers and sclera. Signal integrated from 40-μm thick slices. Reproduced from [57].

The example OCT dataset in Figure 2.2 shows the living human retina. The data was acquired *in vivo* and demonstrates the powerful capability of OCT to provide depth resolved images in biological tissue.

2.2 Polarization-sensitive OCT

Image contrast in standard OCT is due to variations in backscattering intensity. However, light is a transverse wave and is more completely described by its polarization. Polarization-sensitive optical coherence tomography (PS-OCT) is a functional extension of OCT developed for probing the birefringence of materials and biological tissue [49,58]. In addition to 3D scattering structure,

12

PS-OCT measures the polarization state of the backscattered light. Imaging samples that exhibit birefringence (polarization-dependent refractive index) will cause a change in polarization.

Polarized light may be decomposed into two orthogonal linear polarization states, referred to as horizontal and vertical. The biological tissue is assumed to behave as a linear retarder, similarly to a birefringent crystal, introducing a polarization dependent delay that can be detected by decomposing the interference pattern into two orthogonal polarization states.
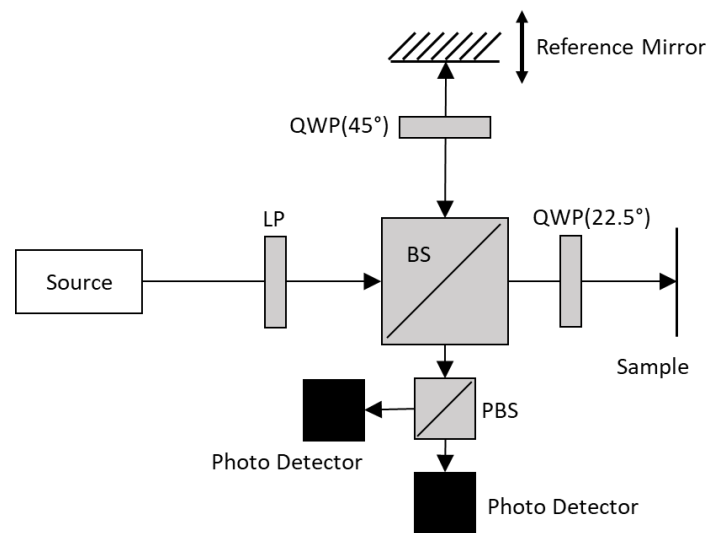
Figure 2.3. Time-domain polarization-sensitive OCT imaging system. Jones calculus is used to represent the polarization state of the light and the optical components. The resulting signal provides a measurement of the change in polarization state caused by the sample. LP: polarizer, BS: beam splitter, QWP: quarter wave plate, PBS: polarizing beam splitter.

A standard free space PS-OCT system is illustrated Figure 2.3. Light from the source is horizontally polarized and split into the reference and sample arms. A quarter-wave plate (QWP) is placed in the reference arm with optic axis at 22.5° relative to the linearly polarized source light, resulting in 45° linearly polarized light exiting the reference arm. This provides equal intensity reference light in both horizontal and vertical polarization states. Sample arm light passes through a QWP at 45° resulting in circularly polarized light incident upon the sample. Circularly polarized

light is desired so that birefringent interaction is guaranteed. If linearly polarized illumination is used, the optic axis of the tissue may match the axis of polarization, giving no useful information.

The interference pattern is split into horizontal and vertical polarization states by a polarizing beam splitter (PBS), and each channel is detected separately. Equation (2.1) then becomes

$$S = \langle E_R E_R^* \rangle + \langle E_S E_S^* \rangle + 2\,\mathrm{Re} \left\{ \begin{matrix} \langle E_{R,H} E_{S,H}^* \rangle \\ \langle E_{R,V} E_{S,V}^* \rangle \end{matrix} \right\}, \tag{2.11}$$

where subscripts H and V denote horizontal and vertical polarizations respectively. To determine the relationship between the sample birefringence and the detected signal, PS-OCT makes use of the Jones vector representation to model the imaging system [59]. This formalism describes each polarization component of the optical system as a Jones matrix, $\mathbf{J}$, which operates upon the electric field Jones vector, $\mathbf{E}$. The resulting signals are given by

$$\begin{aligned} S_H(z) &\propto \sqrt{R(z)} \sin(k_0 z \Delta n) \\ S_V(z) &\propto \sqrt{R(z)} \cos(k_0 z \Delta n), \end{aligned} \tag{2.12}$$

where $R(z)$ is the reflectivity and Δn is the difference in refractive index between the horizontal and vertical channels. The reflectivity may be easily recovered by

$$R(z) = |S_H(z)|^2 + |S_V(z)|^2, \tag{2.13}$$

while the cumulative phase retardation between the polarization channels is

$$\delta(z) = \arctan\left(\frac{|S_H(z)|}{|S_V(z)|} \right). \tag{2.14}$$

In biological tissues, form birefringence arises due to the organization of the tissue microenvironment which provides insight into various biological processes. PS-OCT has been particularly valuable for imaging disease in birefringent tissues such as muscle, skin, the retina,

14

arterial plaque, and collagen in the breast [50,60–64]. PS-OCT is also well-suited for the imaging of birefringent materials such as polymers [65].

The additional information provided by PS-OCT allows for improved contrast in breast cancer imaging. During surgical resection of the breast tumor, it is important to have a negative surgical margin, meaning that there are no tumor cells near the surface of the resected tissue. This is illustrated in Figure 2.4.
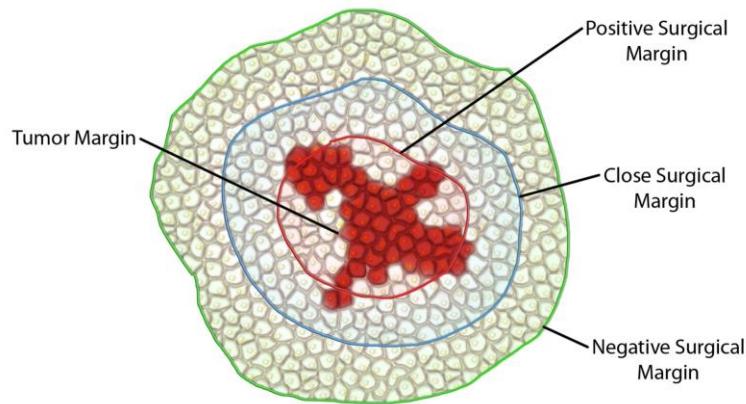
Figure 2.4. Surgically resected tissue specimen containing tumor cells (red) embedded within healthy tissue. Depending upon the thickness of healthy tissue bordering the tumor, the surgical margin is classified as positive, close, or negative. A negative margin gives confidence that the entire tumor has been resected.

OCT has proven useful for looking beneath the tissue surface to determine the status of the surgical margin [9]. However, it is often difficult to distinguish between the dense stroma tissue, which is not cancerous, and solid tumor. Because the stroma is composed mostly of collagen, it is highly anisotropic and birefringent. Therefore, PS-OCT can help distinguish between healthy and cancerous breast tissue by imaging the phase retardation caused by the birefringence of collagen. This is demonstrated in Figure 2.5, where the tissue has been stained for collagen. The presence of collagen causes a change in the polarization state, indicated by color change in the PS-OCT phase retardation image.
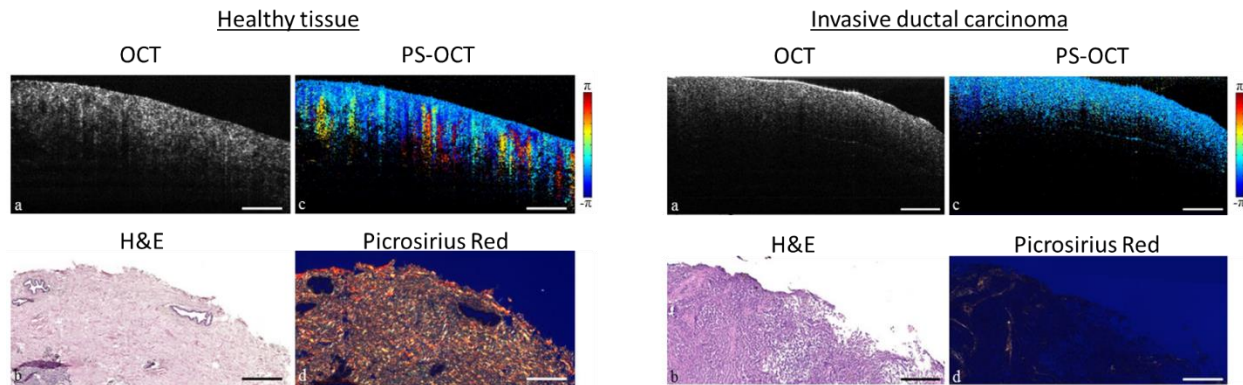
Figure 2.5. OCT and PS-OCT data of healthy and cancerous human breast tissue. Corresponding histology is shown stained with hematoxylin and eosin (H&E) to show cellular composition, and also with picrosirius red which stains collagen. Changes in the PS-OCT signal correspond to changes in polarization state due to tissue birefringence. The dense collagen of the healthy tissue, as seen in the picrosirius red stain, causes strong birefringence. In comparison, the cancerous tissue is devoid of collagen and does not show a change in polarization state. Scale bar represents 500 μm. Adapted from [50].

2.3 Adaptive optics OCT

Measurement and correction of aberrations is often an important step in obtaining high-resolution images in optical microscopy [27]. In some cases, the imaging optics may be imperfect due to physical limitations or design constraints. Additionally, imaging below the surface of biological tissue is complicated by sample-induced aberrations, which arise from the spatially varying refractive index of the tissue. In the case of living or dynamic samples, these aberrations can also be time varying. This is especially important in the human eye, which is highly aberrated at larger pupil diameters and constantly changing [66]. Therefore, it is necessary to somehow determine and compensate for the wavefront aberrations to obtain a diffraction-limited image.

Adaptive optics (AO) involves the use of optical elements which can be dynamically adjusted to compensate for aberrations. This includes the use of a wavefront sensor to determine the aberrations, and a deformable mirror to correct the aberrations based upon this measurement. An illustration of the adaptive optics concept in retinal imaging is given in Figure 2.6.
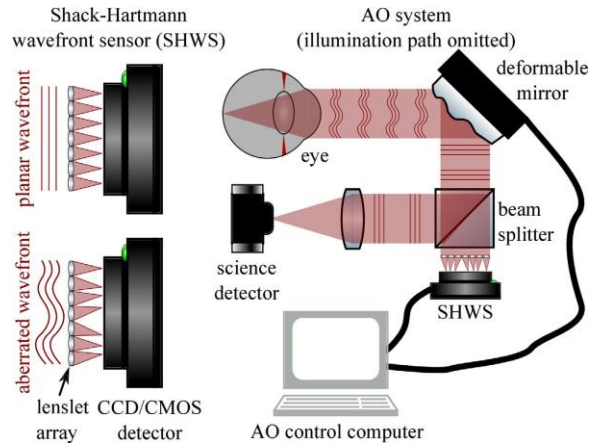
Figure 2.6. The concepts of Shack-Hartmann wavefront sensing (SHWS) and closed-loop AO correction with a deformable mirror. A SHWS works by sampling a wavefront with an array of small lenses (lenslets) such that local wavefront slope—due to aberration—manifests as displacement of the resulting focal spot (left). These displacements can be used directly to drive a corrector such as a deformable mirror (right), or to reconstruct the wavefront. Reproduced from [66].

The most commonly used wavefront sensor is the Shack-Hartmann, which consists of an array of small lenses focused upon a CCD array. A flat wavefront incident on a lenslet will focus to a point at the center of the lenslet, while a tilted wavefront will displace the focal point. In this way, the local tilt of the wavefront can be determined for each lenslet to give the overall shape of the aberrated wavefront. The deformable mirror consists of a metallic membrane suspended over many adjustable pistons, allowing the surface of the mirror to take on arbitrary shapes. Using a closed-loop feedback system, the wavefront sensor measurement can be used to update the deformable mirror shape such that the sensor measures a flat wavefront.

The deformable mirror may also be operated without the wavefront sensor. This method is termed sensorless AO [67]. The shape of the mirror is adjusted to maximize a metric which is associated with the beam quality, such as signal intensity. This method is suitable for decreasing the overall cost and complexity of the AO system, but increases the imaging acquisition time. This is because a search must be performed over various mirror shapes to find the optimal aberration correction. In contrast, standard AO provides aberration correction in a single step.

Although not indicated in Figure 2.6, the pupil plane of the eye, deformable mirror surface, and wavefront sensor pupil must all be imaged to one another using a series of "4f" optical systems. This adds significant pathlength to the sample arm, which must be matched in the OCT reference arm. As a result, the system is quite bulky and more susceptible to motion. Maintaining accurate alignment of the 4f system is also quite challenging. For these reasons, AO retinal imaging systems are primarily used in research laboratories.

The wavefront is often represented using Zernike polynomials, which form a basis set over the unit circle [68]. These functions correspond to familiar optical aberrations, and can also be used to generate more exotic wavefront errors. The first ten orders of Zernike polynomials are illustrated in Figure 2.7.
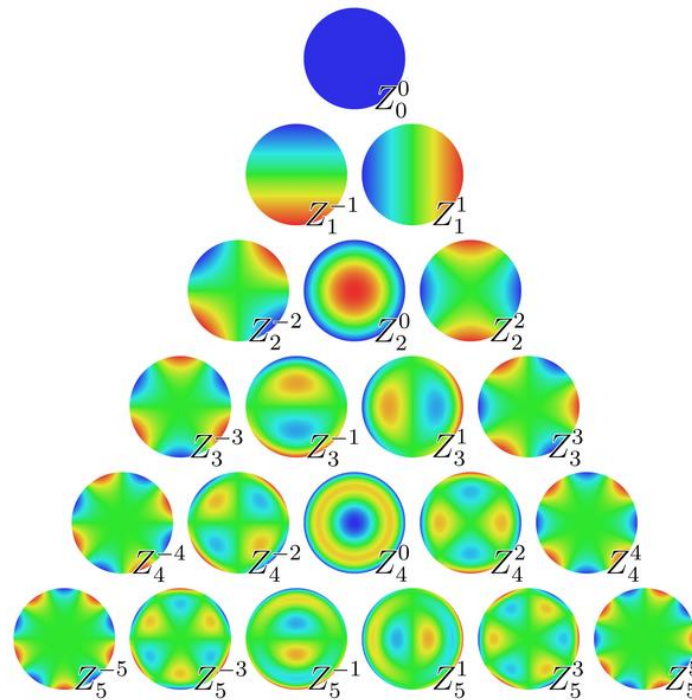
Figure 2.7. Surface plots of the Zernike polynomial sequence up to 10 orders. The name of the classical aberration associated with some of them is also provided. Reproduced from [69].

The cellular composition of the retina is shown in Figure 2.8(a). OCT measures reflections from within and between the cells caused by variations in refractive index. Particularly bright reflections come from the boundaries between certain cell layers, particularly the photoreceptor layer. Labeled retinal OCT layers are shown in Figure 2.8(b), corresponding to the histological layers. Because of the low NA required to image without aberrations, individual cells cannot be resolved. Instead, each layer is identified by a general intensity level and perhaps a unique texture. In contrast, AO-OCT can use a high NA and resolve individual cells throughout the retina, as exemplified in Figure 2.9.

(a)

100 μm

(b)

NFL:	Nerve Fiber Layer	ONL:	Outer Nuclear Layer
GCL:	Ganglion Cell Layer	IS:	Inner Segment
IPL:	Inner Plexiform Layer	OS:	Outer Segment
INL:	Inner Nuclear Layer	RPE:	Retinal Pigment Epithelium
OPL:	Outer Plexiform Layer		
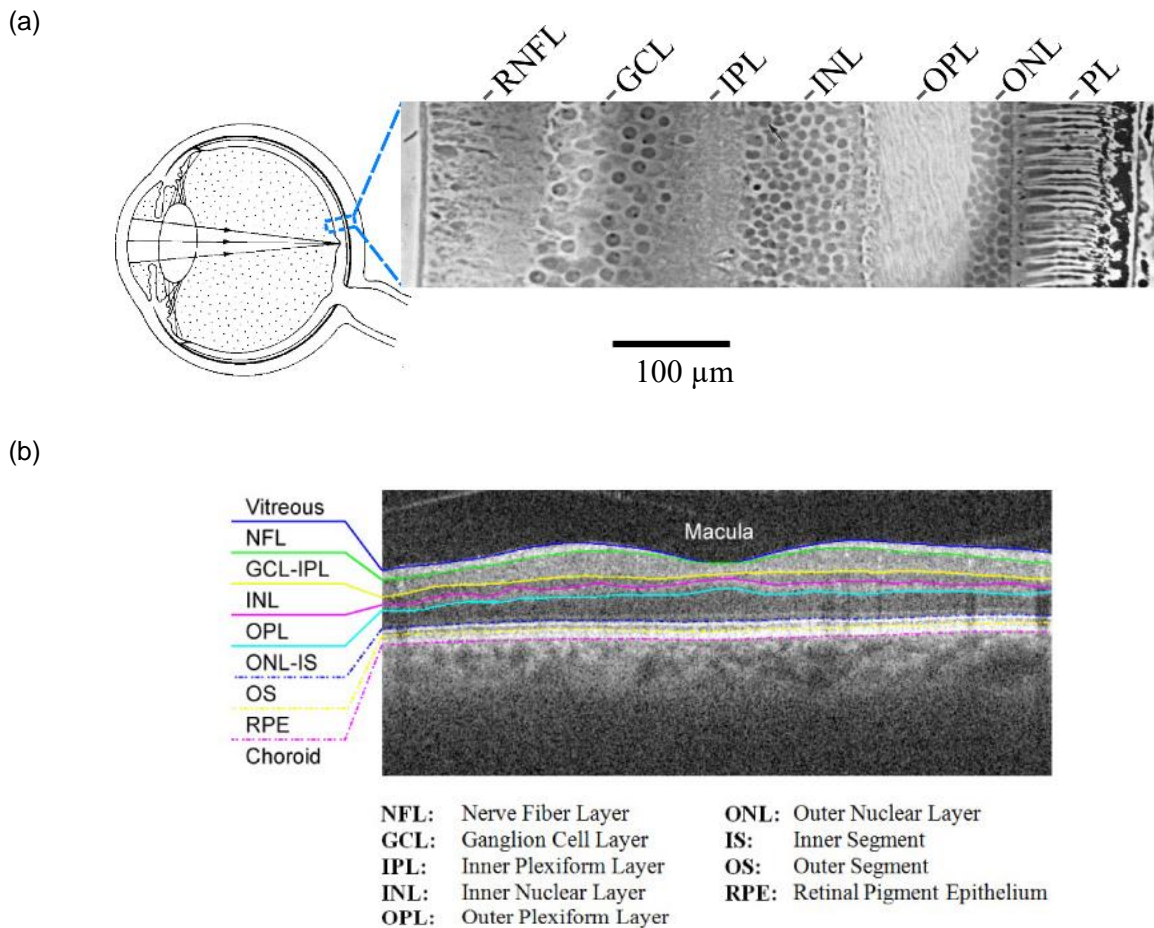
**Figure 2.8.** (a) Histologic cross section of the human retina relative to OCT imaging beam. GCL, ganglion cell layer; IPL, inner plexiform layer; INL, inner nuclear layer; OPL, outer plexiform layer; ONL, outer nuclear layer; PL, photoreceptor layer; RNFL, retinal nerve fiber layer. (b) Automatically segmented cell layers in an OCT cross-sectional image. The varying intensities and textures correspond to the various cell layers. Without adaptive optics, single cells are not resolved. The transverse field-of-view is 6.7 mm. Adapted from [66,70].
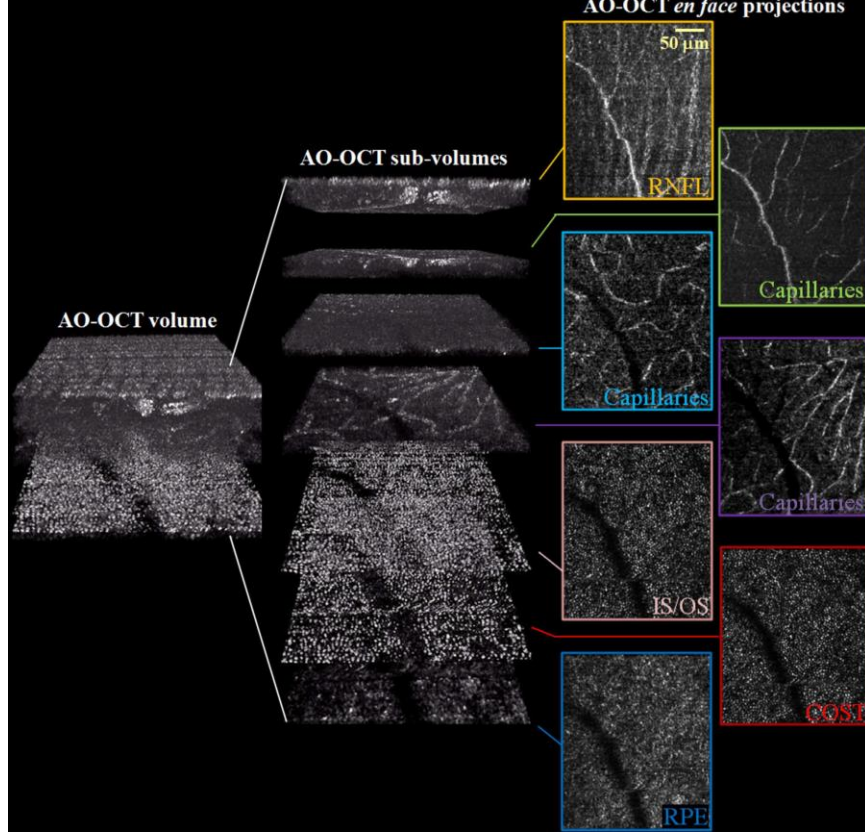
Figure 2.9. Adaptive optics OCT volumes acquired with different focal depths to highlight various cell layers in the retina. Single cells are visible that would otherwise be obscured by aberrations. Reproduced from [66].

2.4 Computational OCT

2.4.1 Coherence and the axial PSF

In FD-OCT, point scanning in the transverse dimension provides a 3D complex dataset $S(x, y; k)$ which is a function of transverse position (*x, y*) and wavenumber *k*. Under the first Born approximation, the measured signal is given by the convolution of the sample scattering potential $\eta(x, y, z)$ with the system point spread function $h(x, y, z; k)$ as

$$S(x, y; k) = \iiint h(x - x', y - y', z'; k)\eta(x', y', z')\,dx'dy'dz'.$$

(2.15)

The point spread function of the system is defined as

$$h(x, y, z; k) = \mu_r k^2 |P(k)|^2 g^2(x, y, z; k), \qquad (2.16)$$

where μ_r is the interferometric power splitting ratio, $|P(k)|^2$ is the power spectral density, and $g^2(x, y, z; k)$ is the product of the identical Gaussian illumination and detection beams. The axial origin of the coordinate system is set as the focal plane $z = 0$ without loss of generality. Using this more complete model of OCT data acquisition, more accurate representations of the scattering sample can be reconstructed.

For interference to take place, the illumination must be spatially and temporally coherent. Nearly all laser sources used in OCT are fiber-coupled using a single-mode fiber. This enforces spatial coherence on the illumination beam, g. The temporal coherence time (or length) is inversely proportional to the width of the power spectral density, $|P(k)|^2$. Therefore, a broad bandwidth will give a short coherence length and accurate depth localization, as discussed in Section 2.1.

There are multiple factors that negatively influence the shape of the coherence function, and therefore the axial PSF. Dispersion mismatch between the sample and reference arms leads to a broadening of the coherence function. Because each wavenumber is measured coherently, the phase is measured and can be computationally adjusted to compensate for the wavelength-dependent path length difference [71,72].

Additionally, the shape of the laser spectrum is often non-Gaussian with multiple peaks [54]. This gives a very poor axial PSF. The spectrum can be apodized, or windowed, prior to Fourier transforming to the spatial domain to smooth the variations in the PSF [73]. Both computational dispersion compensation and spectrum apodization are computational techniques commonly used in standard OCT processing.

2.4.2 Interferometric synthetic aperture microscopy

The solution to the OCT inverse problem, termed interferometric synthetic aperture microscopy (ISAM), uses the information inherent in the OCT data to remove defocus. Using the convolution theorem, Eq. (2.15) can be rewritten in the spatial frequency domain as

$$\tilde{S}\left(Q_x, Q_y; k\right) = \int H\left(Q_x, Q_y, z'; k\right) \tilde{\eta}\left(Q_x, Q_y, z'\right) dz' \; , \tag{2.17}$$

where $(\tilde{\;})$ represents the 2D Fourier transform and Q denotes spatial frequency.

In general, the frequency domain response is depth-dependent. However, using asymptotic approximations for both the near-focus and far-from-focus cases, Eq. (2.17) can be simplified to the forward model

$$\tilde{S}\left(Q_x, Q_y; k\right) = H\left(Q_x, Q_y; k\right) \tilde{\tilde{\eta}}\left(Q_x, Q_y, Q_z\right) \; , \tag{2.18}$$

where $(\tilde{\tilde{\;}})$ represents the 3D Fourier transform and

$$Q_z = -\sqrt{4k^2 - Q_x^2 - Q_y^2} \; . \tag{2.19}$$

The system response $H\left(Q_x, Q_y; k\right)$ takes slightly different forms for the near- and far-from-focus cases, and in theory, it must be inverted to fully recover the scattering potential (a detailed treatment of the system response function can be found in [42]). However, the system response is generally slowly varying within the pass-band and does not introduce significant image distortions [44]. Therefore, Eq. (2.18) can be inverted through a Fourier domain resampling of the data according to the relationship

$$k = \frac{1}{2}\sqrt{Q_x^2 + Q_y^2 + Q_z^2} \; . \tag{2.20}$$

This recovers the unfiltered solution of the scattering potential in the frequency domain

22

$$\tilde{\tilde{\eta}}^{+}\left(Q_{x},Q_{y},Q_{z}\right)=\tilde{S}\left(Q_{x},Q_{y};k\right)\Big|_{k=\frac{1}{2}\sqrt{Q_{x}^{2}+Q_{y}^{2}+Q_{z}^{2}}} \quad, \tag{2.21}$$

which can be returned to the spatial domain by the 3D inverse Fourier transform

$$\eta^{+}\left(x,y,z\right)=F^{-1}\left\{\tilde{\tilde{\eta}}^{+}\left(Q_{x},Q_{y},Q_{z}\right)\right\} \quad. \tag{2.22}$$

The coordinate resampling step in Eq. (2.21) represents the re-phasing of the 3D spatial frequency content, and is comparable to Stolt mapping in synthetic aperture radar [74]. In addition, a helpful analogy can be drawn between ISAM and diffraction tomography [42]. The measured spatial frequency vector $\mathbf{Q}$ is given by the difference of the output and input wave vectors $\mathbf{k}_{out}$ and $\mathbf{k}_{in}$,

$$\mathbf{Q}=\mathbf{k}_{out}-\mathbf{k}_{in} \quad. \tag{2.23}$$

In the far-from-focus approximation, $\mathbf{k}_{out}=-\mathbf{k}_{in}$ and therefore $\mathbf{Q}=-2\mathbf{k}_{in}$. Considering the entire range of illumination angles within the imaging beam, the measured spatial frequencies trace out a wedge of radius $2k$ on the Ewald sphere [75]. Calculation of the square magnitude of $\mathbf{Q}$ gives the relationship

$$Q_{x}^{2}+Q_{y}^{2}+Q_{z}^{2}=4k^{2} \quad, \tag{2.24}$$

which simplifies immediately to the ISAM coordinate resampling as in Eq. (2.20).

The ISAM imaging system is essentially identical to that used in OCT imaging, achieving resolutions of 1-10 µm and imaging depths of 1-3 mm in tissue. The key difference is that the numerical aperture (NA) may be increased without sacrificing depth-of-field, and further, a higher NA is often used to achieve higher transverse resolution. The NA used in ISAM typically ranges from 0.05 to 0.1 [17,35]. Recently, ISAM was demonstrated at 0.6 NA for optical coherence microscopy, removing the need for z-stacking [76].

23

Detailed steps for the implementation of the ISAM reconstruction are listed in Table 2.1. The ISAM simulation for a point-scattering sample shown in Figure 2.10 illustrates the data resampling process. The initial curvature of the data in the spatial frequency domain is corrected through appropriate resampling, resulting in a reconstruction with depth-independent resolution. Note that ISAM processing is in addition to any spectral-domain OCT processing steps such as k-linearization, apodization, and dispersion correction.

TABLE 2.1

3D ISAM PROCESSING STEPS

---

1. Begin with the dataset $S(x,y;k)$.

2. Calculate the 1D inverse Fourier transform to retrieve the complex dataset $S(x,y,z)$, keeping only the positive depths $z>0$.

3. If desired, zero-pad the signal along depth z to improve the subsequent frequency-domain resampling.

4. Circularly shift along depth z to place the focal plane at $z=0$.

5. Calculate the 3D Fourier transform to retrieve $\tilde{S}(Q_x,Q_y;k)$.

6. Resample $\tilde{S}(Q_x,Q_y;k)$ along k according to Eq. (2.20) to retrieve the frequency-domain scattering potential $\tilde{\eta}^+(Q_x,Q_y,Q_z)$.

7. Calculate the 3D inverse Fourier transform of $\tilde{\tilde{\eta}}^+(Q_x,Q_y,Q_z)$ to retrieve the reconstructed scattering potential $\eta^+(x,y,z)$.
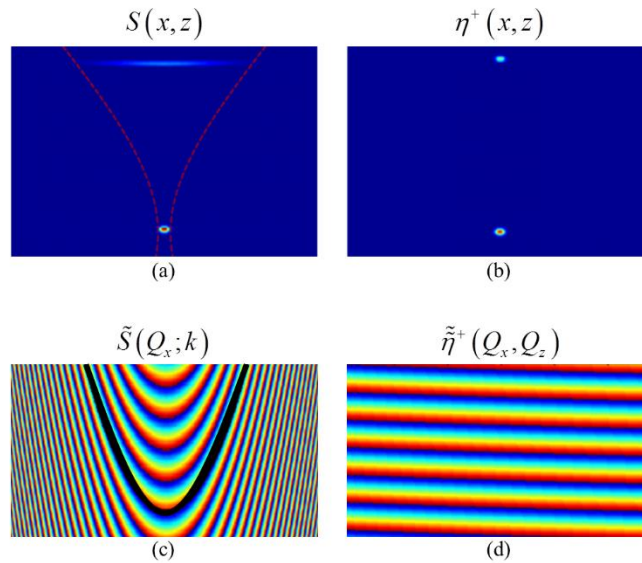
Figure 2.10. Simulation of in focus and far-from-focus scattering particles. (a) Cross section of the standard OCT reconstruction showing strong defocus. (b) ISAM reconstruction showing high resolution throughout depth. (c) Frequency-domain representation of original dataset. Black line illustrates ISAM resampling curve. (d) Resampled frequency-domain data. Adapted from [38].

Alternatively, ISAM can be decomposed into two orthogonal 2D reconstructions for improved processing speed, which enables real-time reconstruction using a graphics processing unit [17,44]. In this scenario, each cross-sectional frame along the fast scanning axis is immediately reconstructed when acquired. Following acquisition of the entire volume, the cross-sectional frames are processed along the slow scanning axis for a complete 3D reconstruction.
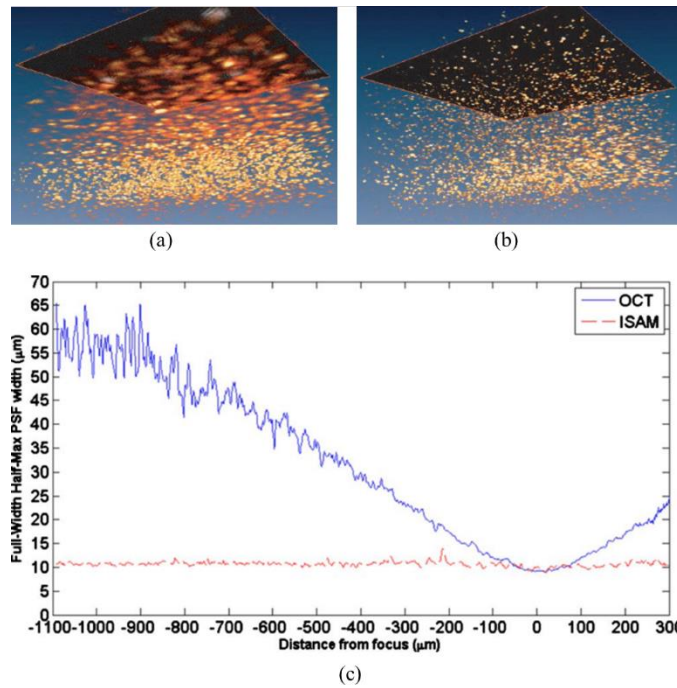
Figure 2.11. Comparison of OCT and ISAM reconstructions of TiO_2 scattering phantom imaged with an 800 nm, 0.05 NA OCT system. Transverse dimensions of the rendered volume are 360 µm by 360 µm. (a) 3D OCT reconstruction. (b) 3D ISAM reconstruction. (c) Transverse resolution throughout depth for OCT and ISAM experimentally demonstrating that ISAM achieves extended depth-of-field. Adapted from [35,77].

ISAM has been validated in both scattering phantoms and biological tissue. OCT and ISAM reconstructions of a TiO_2 scattering phantom are shown in Figure 2.11. The limited depth-of-field is clear in the OCT rendering, while ISAM shows high resolution throughout the volume. A plot of measured transverse resolution over depth is shown in Figure 2.11(c). An *en face* plane approximately eight Rayleigh ranges (450 µm) above the focus was selected for comparison. The beam focus was then moved to the plane of interest and an additional OCT dataset was acquired.

The ISAM reconstruction of the out-of-focus plane was shown to match the structure of the in-focus OCT measurement [77].

ISAM also provides an accurate reconstruction of biological tissue structure. This was demonstrated in *ex vivo* human breast tissue where OCT and ISAM reconstructions were compared to the corresponding histology. Because of the high transverse resolution throughout the entire imaging depth, ISAM showed a stronger correspondence to histology. These results illustrate the improved capability of ISAM to perform volumetric high-resolution imaging in biological tissue [35].

2.4.3 Computational adaptive optics

Aberrations may be modeled as a phase-only linear filter which modifies the objective lens pupil function [38]. Within the volume of stationarity $V(x_0, y_0, z_0)$ centered at position (x_0, y_0, z_0), a particular wavefront description is valid. The corresponding aberration phase filter can be written as $H(Q_x, Q_y; k)\big|_{V(x_0, y_0, z_0)}$. This filter can be applied to the previously derived ISAM model, and Eq. (2.18) can be modified to

$$\tilde{S}_A(Q_x, Q_y; k)\big|_{V(x_0, y_0, z_0)} = H_A(Q_x, Q_y; k)\big|_{V(x_0, y_0, z_0)} \times H(Q_x, Q_y; k)\tilde{\tilde{\eta}}(Q_x, Q_y, Q_z). \qquad (2.25)$$

The aberration effects can be inverted through phase conjugation using the inverse filter

$$H_{AC}(Q_x, Q_y; k)\big|_{V(x_0, y_0, z_0)} = H_A^*(Q_x, Q_y; k)\big|_{V(x_0, y_0, z_0)}, \qquad (2.26)$$

which results in the aberration-free signal

$$\tilde{S}_{AC}(Q_x, Q_y; k)\big|_{V(x_0, y_0, z_0)} = H_{AC}(Q_x, Q_y; k)\big|_{V(x_0, y_0, z_0)} \times \tilde{S}_A(Q_x, Q_y; k)\big|_{V(x_0, y_0, z_0)}. \qquad (2.27)$$

26

If the aberrations can be considered invariant over the transverse field-of-view, the aberration and correction filters can be simplified to $H_A\left(Q_x,Q_y;k\right)\big|_{V(z_0)}$ and $H_{AC}\left(Q_x,Q_y;k\right)\big|_{V(z_0)}$, respectively.

The aberration correction filter $H_{AC}\left(Q_x,Q_y;k\right)\big|_{V(z_0)}$ is related to both the spatial frequency and spectral domains, so it can correct both monochromatic as well as chromatic aberrations [38,42]. Under the assumption of an achromatic system, the *k*-dependence of the 3D aberration correction filter can be simplified to the monochromatic aberration function, $H_{AC}\left(Q_x,Q_y\right)\big|_{V(z_0)}$.

The steps for applying CAO processing are summarized in Table 2.2. It is noted that if the aberrations vary considerably within the transverse field-of-view at a given depth, one can divide the image field into sub-regions and implement processing Steps 2-5 on each sub-region. The aberration corrected sub-regions can then be recombined to retrieve the composite image for each depth [46]. In cases where the dominant aberrations are space-invariant along depth, the same aberration correction filter can be applied to the entire 3D volume to speed up the computation.

TABLE 2.2

CAO PROCESSING STEPS

---

1. Begin with the complex OCT or ISAM dataset $S_A\left(x,y,z\right)$.

2. Calculate the 2D Fourier transform of *en face* image fields at each depth z_i, $\tilde{S}_A\left(Q_x,Q_y,z_i\right)$.

3. Calculate the aberration correction filter $H_{AC}\left(Q_x,Q_y\right)\big|_{z_i}$ for the image field.

4. Apply the aberration correction in the Fourier plane by complex multiplication at each depth
$$\tilde{S}_{AC}\left(Q_x,Q_y,z_i\right)=H_{AC}\left(Q_x,Q_y\right)\big|_{z_i}\times\tilde{S}_A\left(Q_x,Q_y,z_i\right).$$

5. Calculate the 2D inverse Fourier transform of $\tilde{S}_{AC}\left(Q_x,Q_y,z_i\right)$ to retrieve the aberration-free image field, $S_{AC}\left(x,y,z_i\right)$.

6. Stack the *en face* image fields along the depth to obtain the aberration-free volume $S_{AC}\left(x,y,z\right)$.
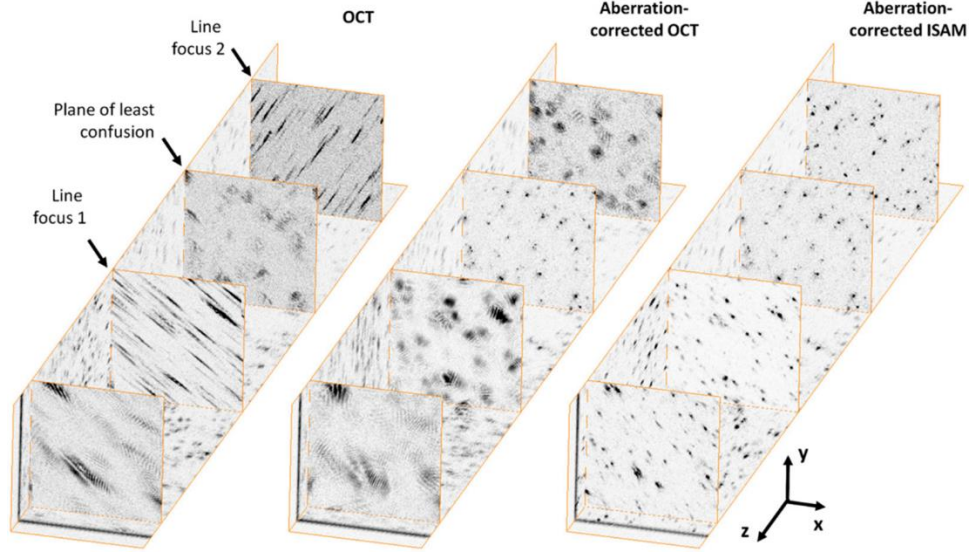
Figure 2.12. Demonstration of aberration correction in a scattering phantom using CAO. Images acquired on a 1300 nm, 0.1 NA OCT system. Select *en face* planes have been rendered to highlight the strong astigmatism. CAO restores the focal plane while ISAM improves the depth-of-field. Transverse dimensions of the rendered volume are 256 µm x 256 µm. Reproduced from [38].

Figure 2.12 demonstrates aberration correction by applying CAO. The dataset was measured from a silicone phantom with subresolution TiO_2 microparticles illuminated by a highly astigmatic beam. *En face* planes using standard OCT processing show the presence of two orthogonal line foci associated with astigmatism, as well as the plane of least confusion located halfway in between. After correcting the astigmatism, the plane of least confusion was restored as the focal plane and the line foci showed a Gaussian-like point spread function (PSF). ISAM was then applied, reconstructing the entire volume with high-resolution. Imaging with the astigmatic beam also gave improved SNR far-from-focus as a result of the dual line foci. This suggests that imaging with an aberrated beam may actually be beneficial when the PSF can be computationally corrected.

Many biological samples have been successfully imaged using CAO such as *ex vivo* human breast tissue, *in vitro* 3D cell cultures, and various *ex vivo* animal tissues. As with ISAM, CAO can also be applied to *in vivo* imaging when stability concerns are considered. Figure 2.13 demonstrates this capability for 3D *in vivo* imaging of human skin. Together, the ISAM and CAO methods

28

complement one another to provide 3D high-resolution images of biological tissue without the need for depth scanning or additional imaging hardware.
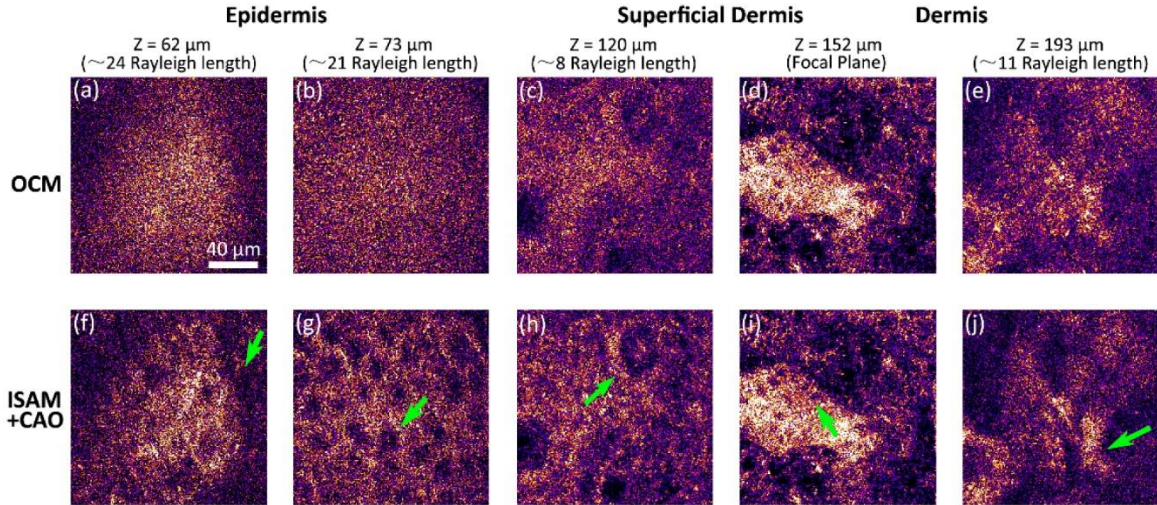
Figure 2.13 High-resolution imaging of *in vivo* human skin acquired using an 860 nm, 0.6 NA OCM system. Arrows indicate (a, f) boundary of the stratum corneum and epidermis, (b, g) granular cell nuclei, (c, h) dermal papillae, (d, i) basal cells, and (e, j) connective tissue. Scale bar indicates 40 µm and applies to all images. Reproduced from [76].

Because the optical aberrations of a particular imaging system are generally unknown, it can be a significant challenge to determine the appropriate correction filter. One solution is similar to sensorless HAO techniques [78]. In sensorless HAO, a sequence of aberration corrections beginning with an initial guess are applied using a deformable mirror. Image metrics are then used to assess the subsequent change of the signal or image quality. Instead of physically altering the wavefront, CAO applies a sequence of computational aberration correction filters which are digitally applied to the complex image. The correction filter $H_{\mathrm{AC}}\left(Q_x, Q_y\right)\big|_z$ can be expressed as a modal term as in Zernike polynomial decomposition, or as a zonal-based wavefront. Several image metrics such as peak intensity, spatial frequency content, and image sharpness have been proposed and demonstrated for use in coherent imaging [79].

A technique termed subaperture correlation has also been proposed to digitally correct the aberrations in OCT data [39]. While CAO mimics the behavior of a deformable mirror, the subaperture technique simulates the operation of the Shack-Harman wavefront sensor by dividing the Fourier plane into several subapertures. The wavefront slopes of each subaperture are calculated from the cross-correlation of the reconstructed subaperture images to the center subaperture reference image. This method has shown image improvement for scattering samples that have a uniform Fourier spectrum, although only low-order aberrations can be corrected.

If the sample contains point-like structures, the so-called "guide-star" method can be used in CAO to correct not only the high-order monochromatic aberrations, but also the chromatic aberrations [45]. A spatial window is used to capture the entire aberrated PSF of the guide-star, and a sub-resolution window is used to crop the guide-star to the desired target PSF. By isolating the signal from a guide-star, the aberrations can be sensed from the phase difference of the measured and desired wavefront in the Fourier domain. The aberration correction filter can then be digitally conjugated in the Fourier domain and applied to the whole image or 3D volume of stationarity containing the guide-star. Finally, after the inverse Fourier transform, the aberration-free data can be retrieved.

2.4.4 Phase stability

Both ISAM and CAO are phase-sensitive techniques and require a certain level of phase stability for the reconstruction to succeed [80]. To ensure phase stable data, it is necessary to both measure and correct the phase instabilities [81,82].
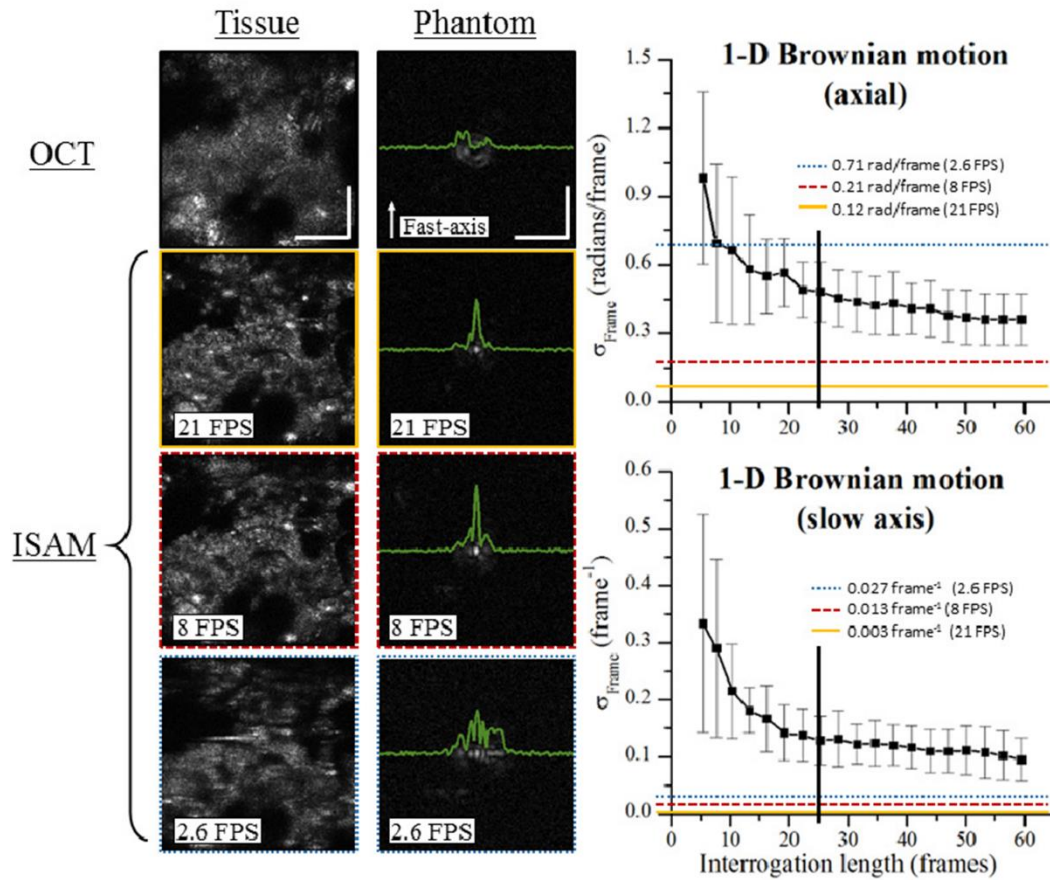
Figure 2.14. ISAM reconstructions of *en face* planes and corresponding stability analysis at various imaging speeds for *ex vivo* tissue and a scattering phantom. Images acquired on an 860 nm, 0.6 NA OCT system. Graphs on the right show calculated stability for each imaging speed (horizontal lines) in comparison to previously determined stability requirements (black squares). The approximate interrogation length is indicated by the vertical black line. The axial motion at 2.6 FPS is above the required threshold, and therefore the corresponding ISAM reconstruction fails. Scale bars represent 85 µm for the tissue and 10 µm for the phantom. Reproduced from [81].

Phase instabilities can be caused by motion of the sample or instability of the imaging system itself. Mechanical instability of the reference arm or scanning mirrors can introduce motion artifacts, and sample motion is often unavoidable in living tissues. In either case, it is necessary that the phase be stable over the interrogation time or interrogation length. The interrogation time is the duration for which the scanning Gaussian beam illuminates or "interrogates" a scattering particle. The interrogation time will be greater for particles far-from-focus, as the beam diameter is larger than at the focus. Therefore, phase stability requirements become stricter farther from focus.

Motion can occur along both the axial and transverse directions. The requirements for the axial dimension are defined in terms of the standard deviation of the phase in units of radians per frame. Requirements in the transverse dimension are defined in terms of transverse resolution elements per frame. The effect of phase instability on computational reconstruction is shown in Figure 2.14 for both *ex vivo* tissue and scattering phantom data. For high scanning speeds, the phase variation is well below the threshold of approximately 0.3 radians per second. However, at the slowest scanning speed, the axial phase instability is too large to achieve an accurate reconstruction. This demonstrates that motion can be largely mitigated using high scanning speeds.
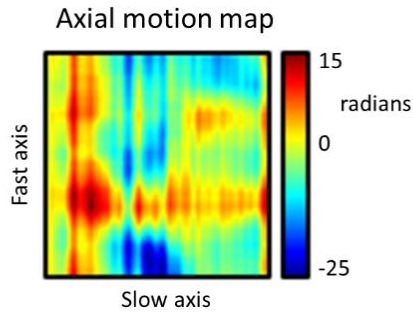
TABLE 2.3

AXIAL MOTION CORRECTION PROCESSING STEPS

1. Begin with the complex OCT dataset $S(x, y, z)$.

2. Calculate the axial phase shift across the slow axis (y) by complex conjugate multiplication of adjacent frames $S(x, y_i, z) \times S^*(x, y_{i+1}, z)$.

3. Depth-average the resulting complex signal over the depth (z) containing the imaging sample, resulting in a two-dimensional axial motion map $A(x, y)$.

4. Set the phase difference to zero for the first frame. Calculate the cumulative sum along the slow axis (y) to convert incremental phase changes to cumulate phase changes.

5. Smooth the axial phase map using a mean filter along the fast axis (x).

6. Apply the motion map correction by complex conjugate multiplication at each depth $A^*(x, y) \times S(x, y, z_i)$.

Both simulation and experiment have demonstrated that computational techniques are most sensitive to phase fluctuations along the axial dimension. The steps for measurement and correction of axial motion are described in Table 2.3 (see [82] for a detailed discussion of transverse motion correction). Calculation of an *en face* axial motion phase map $A(x, y)$ is used to negate the axial motion through complex conjugate multiplication with the complex data $S(x, y, z)$. The result is phase stable data to which various computed imaging techniques can be applied. A representative motion map is shown in Figure 2.15.

Figure 2.15. Axial motion map resulting from the steps outlined in Table 2.3, showing smoothed cumulative phase variations. Adapted from [82].

2.4.5 *In vivo* retinal imaging

Imaging the living human eye is an application where computational OCT could have great impact, but is very difficult in practice. Imaging of the photoreceptors aids the diagnosis and understanding of diseases such as macular degeneration [83,84]. Although it is possible to image the photoreceptors without adaptive optics provided the subject's eye has very low aberrations [25,85], in general this is not the case [86]. As the numerical aperture of the imaging beam is increased, aberrations play an increased role and distort the point spread function [87,88]. Because of this, HAO solutions have been used to achieve diffraction-limited imaging of the retina [66]. However, the cost and complexity of HAO has restricted its wide-spread clinical application. A computational alternative, therefore, is highly desirable.

The eye exhibits frequent and unavoidable motion [89]. This motion poses a significant challenge for computational techniques and must be carefully considered. Unlike the skin, direct physical contact of the imaging hardware with the eye is not clinically feasible. Therefore, high scanning speeds and motion correction techniques must be implemented. Transverse motion correction can be avoided by imaging at cross-sectional frame rates greater than 2.5 kHz [90].

The first CAO images of the living human retina were recently reported using an *en face* OCT imaging system [18]. The use of *en face* OCT allowed for a higher effective frame rate in comparison to typical spectral-domain methods. The system operated at 4,000 *en face* lines per second, which for stability purposes is equivalent to a spectral-domain OCT system operating at a frame rate of 4 kHz. Even at this high imaging speed, axial motion correction was required due to phase instabilities from the acoustic optic modulators and sample motion. The axial motion correction algorithm outlined in Table 2.3 was used, slightly modified to work with *en face* data.
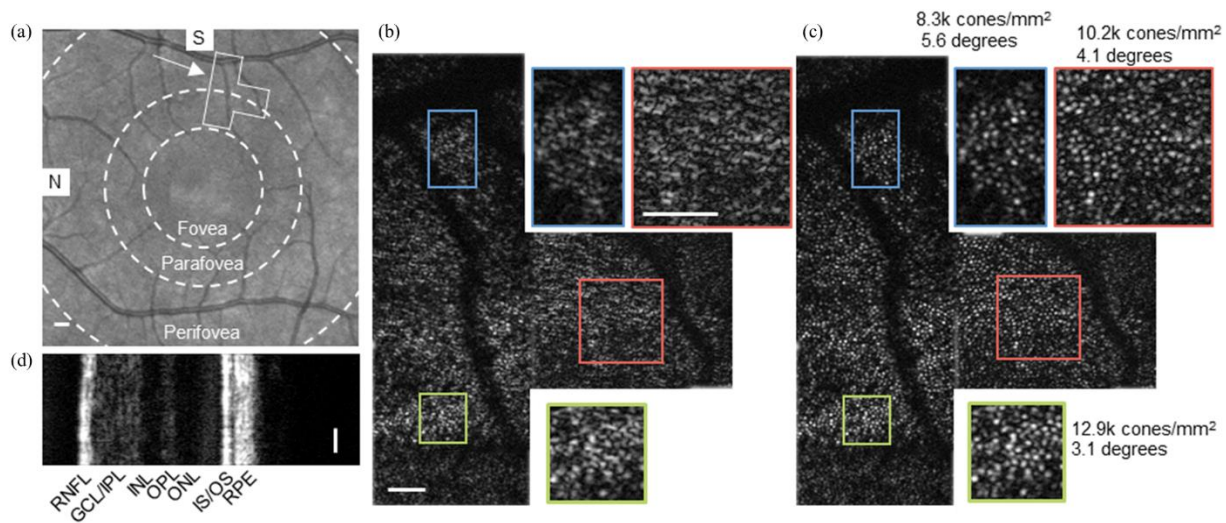

Figure 2.16. Aberration correction in the living human retina using computational adaptive optics. (a) Scanning laser ophthalmoscope image of the retinal surface. N: nasal, S: superior. OCT images taken in the boxed region. (b) Uncorrected *en face* OCT data shows no recognizable features. (c) Aberration corrected data showing individual photoreceptors. (d) Simultaneously acquired cross-sectional OCT data showing the various retinal layers. The *en face* photoreceptor mosaic was acquired at the IS/OS junction. RNFL: retinal nerve fiber layer, GCL/IPL: ganglion cell layer/inner plexiform layer, INL: inner nuclear layer, OPL: outer plexiform layer, ONL: outer nuclear layer, IS/OS: inner segment/outer segment, RPE: retinal pigment epithelium. Colored boxes correspond to the matching zoomed regions. Scale bar represents 1° in (a) and 0.25° in (b-d). Reproduced from [18].

The subaperture and guide-star methods were implemented sequentially to determine the appropriate aberration correction filter for imaging the photoreceptor layer. The subaperture method was used to determine a bulk correction and the individual photoreceptors served as natural guide-stars to fine-tune the correction, modifying the Zernike polynomial terms of the bulk correction by up to 40%. The resulting photoreceptor mosaic is shown in Figure 2.16. The CAO

34

result clearly resolves the individual photoreceptors, gleaning valuable biological information from previously unintelligible data.

Visualization of other retinal layers also benefits from improved resolution. The health of the retinal nerve fiber layer (RNFL) is an important marker for diseases such as glaucoma [91,92] and multiple sclerosis [93,94]. These fibers are densely packed and difficult to resolve without aberration correction. CAO imaging of retinal fiber structure is shown in Figure 2.17, acquired using the same *en face* imaging system. The aberration correction was manually adjusted to maximize the anisotropy image metric, and the previously hidden structure was clearly resolved.

(a)　　　　　　　(b)　　(c)
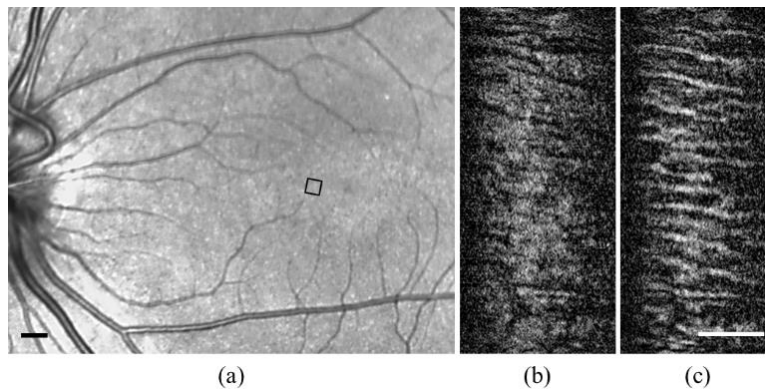
Figure 2.17. Computational adaptive optics of retinal fiber structure. (a) Scanning laser ophthalmoscope image of the retinal surface. The boxed region indicates the approximate OCT imaging location. (b) Uncorrected *en face* OCT data. (c) Data corrected using CAO showing improved resolution of the fiber structure. Scale bar represents approximately 2° in (a) and 0.2° in (b, c). Reproduced from [95].

3 POLARIZATION-SENSITIVE ISAM

3.1 Motivation

Various extensions of OCT have been developed to provide enhanced contrast between tissue types. One such extension is polarization-sensitive OCT (see Section 2.2). Like standard OCT imaging, PS-OCT suffers from limited depth-of-field. This is solved in OCT through the ISAM reconstruction (see Section 2.4.12). The ISAM solution can be expanded to include the vector field to account for polarization [42]. However, complications arise when comparing the ISAM and PS-OCT models.

This chapter highlights and resolves these complications, and demonstrates the extension of ISAM to polarization sensitive imaging, termed polarization-sensitive interferometric synthetic aperture microscopy (PS-ISAM). This technique is the first functionalization of the ISAM method and provides improved depth-of-field for polarization-sensitive imaging. The basic assumptions of polarization-sensitive imaging are explored, and refocusing of birefringent structures is experimentally demonstrated.

3.2 PS-ISAM hybrid model

PS-OCT makes use of the Jones vector representation to model the imaging system [58,59]. This formalism describes each polarization component of the optical system as a Jones matrix, $\mathbf{J}$, which operates upon the electric field Jones vector, $\mathbf{E}$. The Jones vector is composed of the horizontal (H) and vertical (V) polarized fields,

$$\mathbf{E} = \begin{bmatrix} E_H \\ E_V \end{bmatrix}. \tag{3.1}$$

The sample is modeled as a waveplate with arbitrary fast-axis orientation, α, which introduces a phase delay via the Jones matrix

$$\mathbf{J}_{\text{sample}}(z, \Delta n, \alpha) = \mathbf{R}(\alpha) \begin{bmatrix} e^{ikz\Delta n/2} & 0 \\ 0 & e^{-ikz\Delta n/2} \end{bmatrix} \mathbf{R}(-\alpha), \tag{3.2}$$
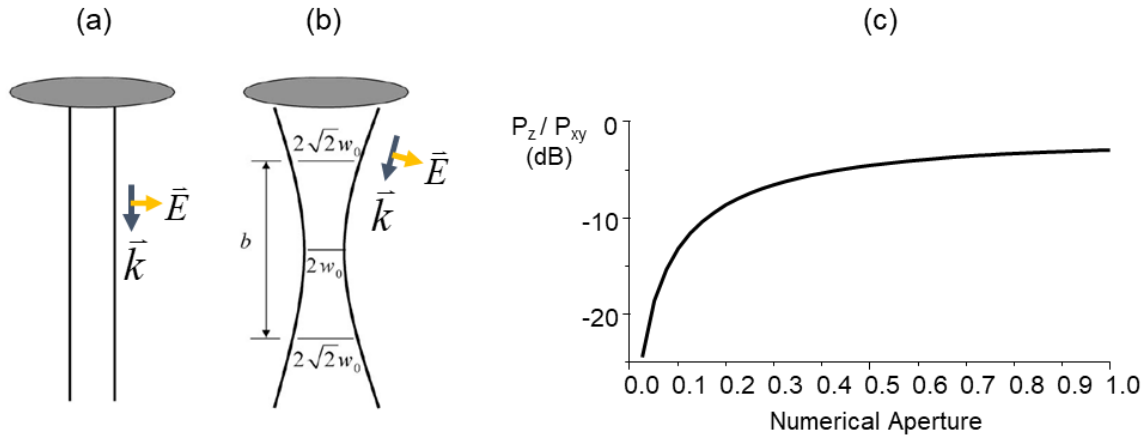
where **R** is the rotation matrix

$$\mathbf{R}(\theta) = \begin{bmatrix} \cos\theta & -\sin\theta \\ \sin\theta & \cos\theta \end{bmatrix}. \tag{3.3}$$

The delay introduced by the waveplate is termed the phase retardation,

$$\delta = kz\Delta n. \tag{3.4}$$

The form birefringence of the sample introduces a phase retardation between the two components of the Jones vector, and is the primary source of contrast in PS-OCT.

Figure 3.1. Electric field polarization for a collimated beam (a), and a focused beam (b). The direction of wave propagation is indicated by k and the electric field by E. The ratio between the total power in the longitudinal, z, and transverse, xy, dimensions is shown for a circularly polarized beam (c). The power in the longitudinal direction increases with numerical aperture.

The use of the Jones calculus assumes the propagation of a collimated, or pencil, beam along the optic axis with the polarization restricted to the transverse plane, as in Figure 3.1(a). In practice, the sample is illuminated with a focused beam. This is taken into account by the ISAM model to

provide high-resolution throughout depth. However, the field polarization of a focusing beam is no longer restricted to the transverse plane, as shown in Figure 3.1(b). At least some of the imaging beam power is along the optic axis. This contradicts the assumptions of the Jones matrix math.

The power ratio between the transverse and longitudinal polarization components of the focused Gaussian beam is shown in Figure 3.1(c). The focused vector beams were simulated for circularly polarized incident light for increasing NA, and the total power was calculated for each dimension [96]. Initially the power is confined to the transverse dimension, as is expected for a collimated beam. As the NA increases, more power is transferred to the longitudinal dimension. However, only at very high numerical aperture is the longitudinal polarization strong enough to allow calculation of the longitudinal susceptibility component of the sample [97]. In the low-NA regime where OCT imaging is typically performed (0.1 NA or lower, see [17] and [35]), the longitudinal polarization is greatly overwhelmed by the power in the transverse polarization. This supports the use of the Jones vector representation at low-NA as in the standard PS-OCT model.

The proposed PS-ISAM method uses a hybrid model, valid in the low-NA regime, which abandons the pencil beam approximation while retaining the transverse polarization approximation. By doing so, both the ISAM resampling equation and the Jones matrix math can be used in the image reconstruction. The ISAM reconstruction is applied to each component of the measured Jones vector through a Fourier domain coordinate resampling of the data according to the relationship of Eq. (2.20). The resampling equation, reproduced here, is

$$k = \frac{1}{2}(Q_x^2 + Q_y^2 + Q_z^2)^{1/2}, \tag{3.5}$$

for wavenumbers $k = 2\pi n / \lambda$ and spatial frequencies Q, where n is refractive index and λ is wavelength. Following this step, the sample reflectivity R and phase retardation δ are calculated for each position in the 3D volume as

$$R(x, y, z) = \left| S_{\mathrm{H}}^{(\mathrm{ISAM})}(x, y, z) \right|^2 + \left| S_{\mathrm{V}}^{(\mathrm{ISAM})}(x, y, z) \right|^2 \tag{3.6}$$

and

$$\delta(x, y, z) = \arctan\left(\frac{\left| S_{\mathrm{H}}^{(\mathrm{ISAM})}(x, y, z) \right|}{\left| S_{\mathrm{V}}^{(\mathrm{ISAM})}(x, y, z) \right|} \right), \tag{3.7}$$

where H and V are the horizontal and vertical components of the measured Jones vector, respectively. Note that Eqs. (3.6) and (3.7) are similar to the PS-OCT calculations of Eqs. (2.13) and (2.14). However, the PS-ISAM equations operate upon the ISAM reconstructed Jones vectors and explicitly reference the 3D coordinate system. This emphasizes the use of a focused imaging beam, as opposed to simply a ranging experiment with a collimated beam.

3.3   PS-ISAM imaging system design and protocol

To demonstrate the PS-ISAM method, a custom spectral domain PS-OCT system was built in collaboration with Thorlabs GmbH. In general, ISAM imaging systems are identical to those used in OCT, with the exception that a higher NA may be used without sacrificing depth-of-field. The system used a traditional free-space PS-OCT design [47,48,62], which built upon the free-space interferometer of the standard Fourier-domain Thorlabs OCT system. An illustration of the system design is given in Figure 3.2.
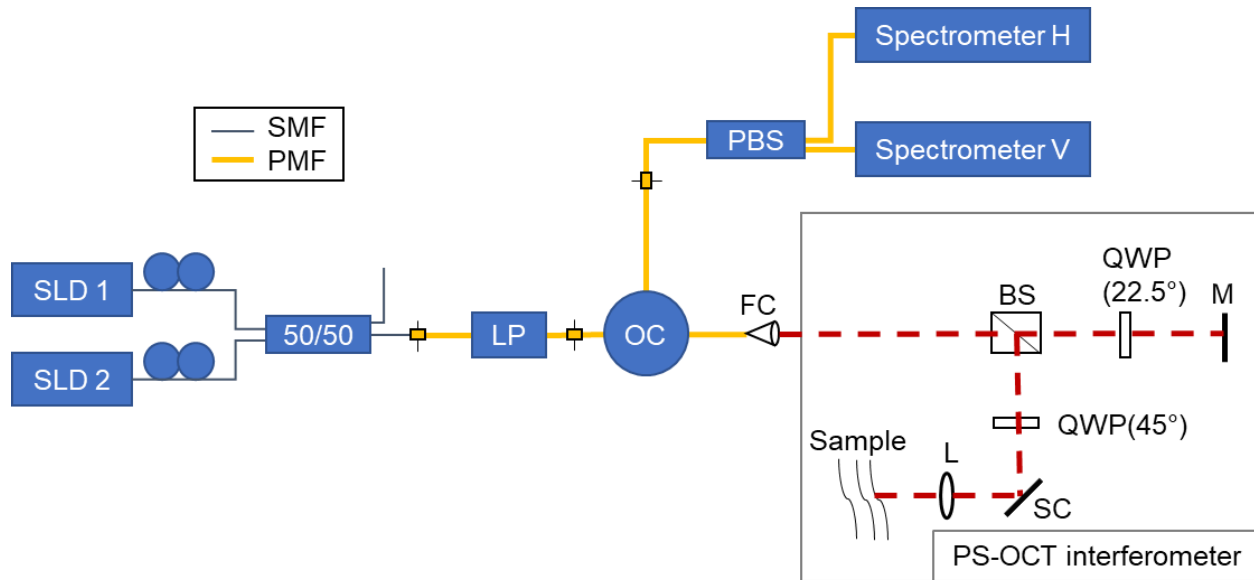
Figure 3.2. Fourier-domain PS-ISAM system. Light is coupled into polarization-maintaining fiber for delivery and collection from the free-space PS-OCT interferometer. The two components of the OCT Jones vector are measured at the spectrometers. SMF: single mode fiber. PMF: polarization-maintaining fiber. SLD: superluminescent diode. LP: linear polarizer. OC: optical circulator. PBS: polarizing beam splitter. FC: fiber collimator. BS: beam splitter. QWP: quarter-wave plate. SC: scanning mirror. L: lens.

The optical source used two Thorlabs superluminescent diodes, coupled together to give a central wavelength of 1300 nm with 100 nm bandwidth (3 dB). Polarization-maintaining (PM) fiber was used to deliver light to and from the free-space PS-OCT interferometer through an in-line linear polarizer (Thorlabs ILP13010PM-APC) and optical circulator (AFW Technologies PMP-13-R-C3N-45-22). An additional 45 meter of PM fiber which was included between the circulator and fiber collimator to displace the ghost images out of the imaging range (see further discussion below). The collected interference signal returned through the circulator to a PM fiber polarizing beam splitter (AC Photonics PBS-13-P-2-2-1-1) for polarization diverse detection. The two polarization components of the Jones vector were measured with two identical spectrometers, each using a 2048-pixel line scan camera (Sensors Unlimited GL2048L). Both the axial and transverse resolution of the system were approximately 7.65 µm full-width-half-maximum (FWHM), or 13 µm ($1/e^2$), giving an NA of 0.065. This was slightly greater than the 0.05 NA of the initial ISAM demonstrations [35]. Three-dimensional datasets were acquired by scanning 512 x 256

transverse points with an isotropic transverse sampling of 3.4 µm to meet the Nyquist sampling requirement.

The additional PM fiber patch cable prior to the PS-OCT interferometer was included to mitigate the effects of cross-talk within the PM fiber [98]. The fast-axis and slow-axis of the PM fiber have different group velocities. In the absence of cross-talk, the fast-axis and slow-axis polarizations travel independently to the spectrometers and the slight difference in arrival time is not an issue. However, cross-talk between the two axes will cause the signals to interfere. This creates copies of the OCT image at a pathlength equal to the difference in optical paths within the PM fiber. The 45 meter patch cable ensured that the optical pathlength mismatch between the fast and slow axes of the PM fiber was well outside the OCT imaging range when the signal reached the optical circulator, where cross-talk occurred. Images acquired with and without the patch cable are shown in Figure 3.3.
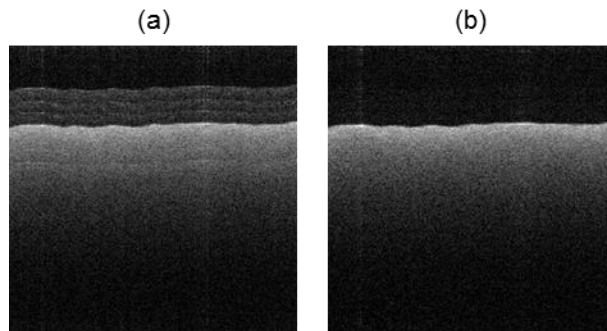
Figure 3.3. Ghost images resulting from PMF cross-talk. (a) Image of a scattering phantom acquired without patch cable, showing several ghost images. (b) Image acquired with the patch cable. Ghost images are no longer visible.

While this mitigated the most severe ghost images, some ghost images remained due to cross-talk at the fiber couplers and within the polarizing beam splitter. These ghost images were only visible for strong signals, such as reflections from the sample surface. These bright reflections were minimized by placing the focus deep into the sample. Coincidentally, this is the ideal scenario for

ISAM imaging. Since depth-of-field is not an issue, the focus can be placed deep within the sample to counteract attenuation and increase signal collection [17].

The quarter-wave plate in the sample arm was adjusted such that circularly polarized light was incident on the sample. Circularly polarized light can be decomposed into two orthogonal linear states with arbitrary orientation, guaranteeing that there will be interactions with both the fast and slow axes of the tissue, regardless of the sample orientation. To calibrate the sample arm waveplate, the reference arm was blocked and a mirror was placed near the focus. When the quarter-wave plate was oriented properly, the linearly polarized light entering the free-space interferometer became circularly polarized after the waveplate. The handedness of the circular polarization will change upon reflection with the mirror at the focus. After returning through the waveplate, the light will be linearly polarized at 90° to the input polarization. In the absence of the waveplate, all reflected power will be in spectrometer H, associated with the input polarization. Therefore, with the waveplate properly oriented, all reflected power will be in spectrometer V.

The quarter-wave plate in the reference arm was adjusted to provide equal power in each spectrometer. This was done by blocking the sample arm and rotating the quarter-wave plate mount until the difference between the spectrometer signals was minimized.

Data from the two spectrometers was processed according to Eqs. (3.6) and (3.7). The OCT and ISAM structural images were generated from the reflectivity, and the PS-OCT and PS-ISAM images from the phase retardation. A two-dimensional median filter of approximately two resolution elements was applied to the phase retardation data to remove random fluctuations for improved visualization.

3.4   Imaging results

3.4.1   Phantom imaging

To demonstrate the capabilities of the PS-ISAM reconstruction, a scattering tissue phantom was imaged consisting of TiO_2 particles, approximately 5 µm in size, suspended in a silicone gel. The results are shown in Figure 3.4. The OCT and ISAM images for an *en face* plane taken from far above focus are shown in Figure 3.4(b) and Figure 3.4(c). The OCT image shows strong blurring caused by the limited depth-of-field, while the corresponding ISAM reconstruction shows clear improvement in the transverse resolution. PS-OCT and PS-ISAM phase retardation images are shown in Figure 3.4(d) and Figure 3.4(e). The valid polarization information is localized to areas with sufficient signal corresponding to the scattering particles in the intensity images, which have phase retardation values near the extremes of the scale corresponding to right-handed and left-handed polarization states [99]. Comparison of the PS-OCT and PS-ISAM images reveals improved localization of the phase retardation information in the PS-ISAM reconstruction due to the improved transverse resolution.

The traces for a single particle shown in Figure 3.4(f) and Figure 3.4(g) highlight the improvement of the PS-ISAM reconstruction over the standard technique. There is a dramatic improvement in the point spread function for ISAM, as expected. The FWHM of the OCT and ISAM point spread functions are overlaid onto the phase retardation trace. This indicates the locations where the phase retardation measurement originates from the point scatterer. Note that although the phase retardation value for the point scatterer is the same for both PS-OCT and PS-ISAM, the measurement is better localized by PS-ISAM. This corresponds to enhanced sharpness in the PS-ISAM phase retardation images.
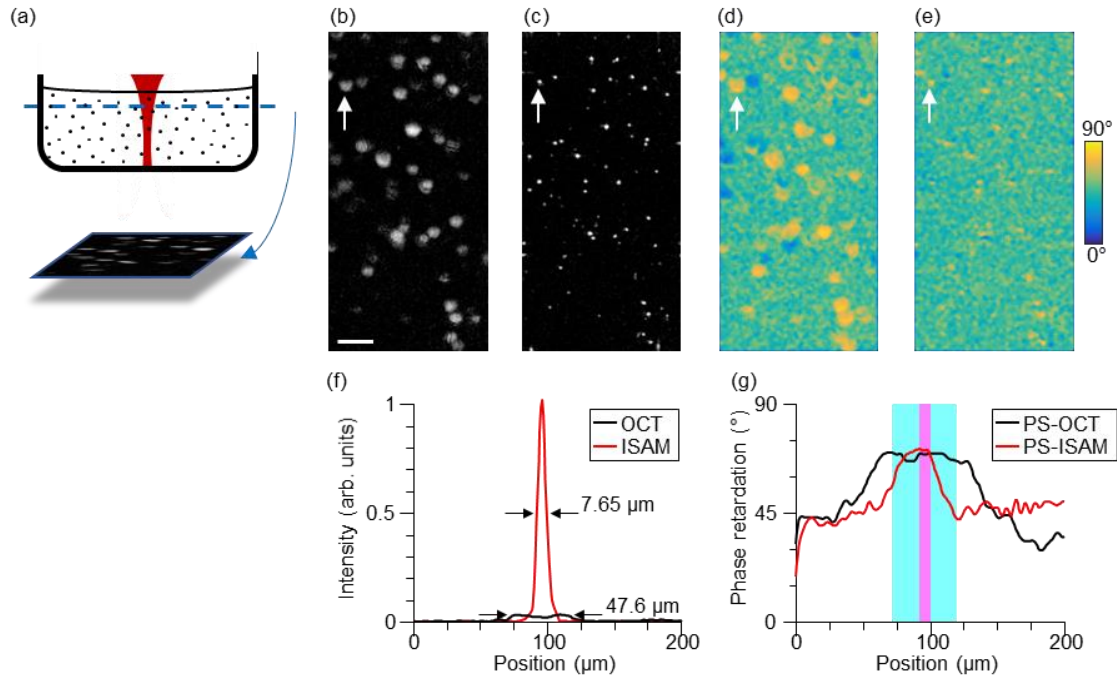
Figure 3.4. PS-ISAM imaging of a scattering tissue phantom. (a) An illustration of the imaging setup which shows the silicone phantom containing sub-resolution microparticles, imaged by a point-scanned focusing beam. *En face* planes are shown from 1502 μm optical distance above focus (10.5 Rayleigh ranges). (b) OCT intensity image. (c) ISAM intensity image. (d) PS-OCT phase retardation image. (e) PS-ISAM phase retardation image. (f) Trace of the OCT and ISAM intensities for a single particle (white arrow) showing the FWHM resolution. (g) Trace of the PS-OCT and PS-ISAM phase retardation for the same particle as in (f). Shaded cyan and magenta areas indicate regions of valid signal from OCT and ISAM intensity measurements respectively, determined from the FWHM measurements in (f). The scale bar indicates 200 μm.

3.4.2 Materials and tissue imaging

Figure 3.5 demonstrates PS-ISAM imaging in a birefringent material. The phantom consisted of small molded plastic pieces suspended in an agarose gel. In more dense scattering samples such as this, the improvement from OCT to ISAM may not be as dramatic due to the relatively uniform scattering structure, as seen in Figure 3.5(b) and Figure 3.5(c). However, the birefringence of the sample causes changes in the polarization state seen as variations in the phase retardation images, Figure 3.5(d) and Figure 3.5(e). This highlights the usefulness of polarization-sensitive imaging as an additional form of contrast. Due to the strong defocus, the phase retardation information in

the PS-OCT image is somewhat indistinct. In contrast, the PS-ISAM reconstruction clearly resolves the polarization patterns throughout the material.

To demonstrate the PS-ISAM technique in biological samples, healthy human breast tissue from a 24-year-old female was imaged *ex vivo*. The focus was placed far below the tissue surface to increase signal collection from deep within the sample. The resulting cross-sectional images are shown in Figure 3.6. Changes in polarization state indicated by the phase retardation measurement in Figure 3.6(d) and Figure 3.6(e) arise due to the aligned collagen fibers in the human breast (see Figure 2.5). These features are more clearly resolved in the PS-ISAM reconstruction, showing fine structure not visible in the PS-OCT data.

To quantitatively demonstrate the improvement in image quality, image metrics were used to assess the sharpness of the phase retardation images. The metrics were calculated for a region of interest in the breast tissue, marked in Figure 3.6(d) and Figure 3.6(e), which contained the changes in polarization state due to sample birefringence. The entire field-of-view was included for assessing the birefringent plastic in Figure 3.5. The PS-ISAM images for both the birefringent phantom and human tissue samples showed improvement over the PS-OCT images in the anisotropy [17,76,100] and Sobel [101] image metrics of greater than 50% and 6.7%, respectively. This improved image quality could potentially benefit the detection of residual cancer in breast tumor margins, where the polarization information can aid in the differentiation between normal and diseased tissue by identifying birefringent regions as collagenous stroma.
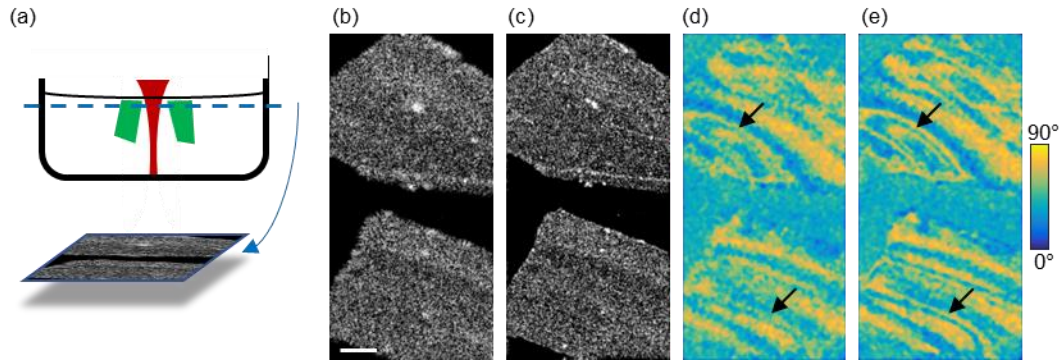
Figure 3.5. PS-ISAM imaging of molded plastic pieces suspended in agarose gel. (a) An illustration of the imaging setup which shows the plastic (green) suspended in the agarose gel, imaged by a point-scanning focused beam. *En face* planes are shown from 1000 µm optical distance above focus (7 Rayleigh ranges). (b) OCT intensity image. (c) ISAM intensity image. (c) PS-OCT phase retardation image. (d) PS-ISAM phase retardation image. The clarity of the phase retardation image is improved (highlighted by arrows). Scale bar indicates 200 µm.
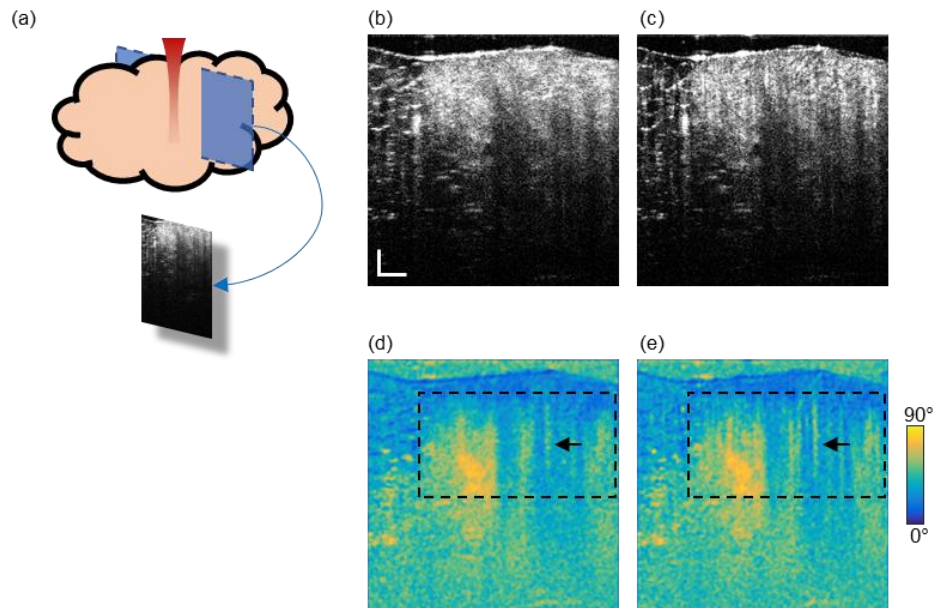
Figure 3.6. PS-ISAM imaging of *ex vivo* human breast tissue. (a) An illustration of the imaging setup which shows the excised tissue sample imaged by a point-scanning focused beam. Cross-sectional planes are shown with the focus placed 1253 µm optical distance below the surface (8.8 Rayleigh ranges). (b) OCT intensity image. (c) ISAM intensity image. (d) PS-OCT phase retardation image. (e) PS-ISAM phase retardation image. Image metrics were calculated over the boxed region in (d,e). The clarity of the phase retardation image is improved (highlighted by arrows). Scale bar indicates 200 µm.

46

4   COMBINED HARDWARE AND COMPUTATIONAL ADAPTIVE OPTICS

4.1   Motivation

As discussed in Section 2.3, imaging the living human retina requires imaging through the optics of the eye itself, which are highly aberrated when the pupil of the eye is large. By compensating for these aberrations using adaptive optics, it is possible to achieve cellular level resolution. Conventionally, this has been achieved using a wavefront sensor and deformable mirror to measure and correct the aberrated optical wavefront [51]. This method is termed hardware adaptive optics (HAO). When combined with optical coherence tomography (OCT), this enables high-resolution, 3D imaging of various cell layers in the retina [26].

However, the HAO correction is optimized for a single depth within the retina. Thus, image quality is not optimal for other depth locations. The wavefront correction may also suffer from limited temporal sampling and inherent measurement or fitting errors. Lastly, successful operation of the HAO system depends upon optimal alignment at the time of imaging. This can be challenging to maintain when acquiring data from human subjects that are not stable, or during an extended imaging session requiring frequent head alignment.

With CAO, the image formation process can continue after data acquisition. This reduces the burden on HAO to provide optimal correction at the time of imaging and the need to maintain optimal subject alignment. Additionally, the aberration correction can be fine-tuned to each depth layer, field position, and time point of acquisition. However, because CAO does not physically modify the wavefront, any photons lost due to the presence of aberrations are not recovered using

CAO. This is particularly true at large pupil diameters, where aberrations are most severe [102]. Previous demonstrations of *in vivo* CAO-only imaging were either performed on undilated subjects [18,90,103], or with large pupil diameters on dilated subjects requiring averaging over tens of datasets to obtain high SNR [104].

This chapter demonstrates the use of HAO and CAO together to address the shortcomings of each method, and to demonstrate how their strengths can be integrated to provide more complete correction of ocular aberrations for *in vivo* retinal imaging.

4.2   HAO+CAO imaging system and protocol

A high-speed HAO-OCT system designed by our collaborator, Prof. Donald Miller, and located at Indiana University, was used to physically correct aberrations and acquire retinal OCT data. Like most HAO systems, the sample arm used mirrors instead of lenses to eliminate back reflections that may interfere with the wavefront measurement. Unfortunately, the use of spherical mirrors introduced strong astigmatism that need to be compensated by placing some mirrors out-of-plane. The Indiana University system was a unique design which used toroidal mirrors to allow for in-the-plane alignment without strong system aberrations [105]. The updated version of the system which was used for these experiments is shown in Figure 4.1. Key differences from the original design include the use of a single deformable mirror and four interleaved spectrometers [106].

A superluminescent diode centered at 790 nm with 47 nm bandwidth was used for both imaging and wavefront sensing, giving an axial resolution in tissue ($n = 1.38$) of 4.2 µm. The pupil size was 6.67 mm at the eye, resulting in a theoretical diffraction limited transverse resolution of 2.4 µm. The spectral domain OCT system used four interleaved spectrometers operating at line rates of 250 kHz each, for an effective line rate of 1 MHz [106]. The HAO system consisted of a

deformable mirror (DM 97, ALPAO) and a custom Shack-Hartmann wavefront sensor, constructed with a 20 x 20 lenslet array in front of a sCMOS camera (Neo, Andor).
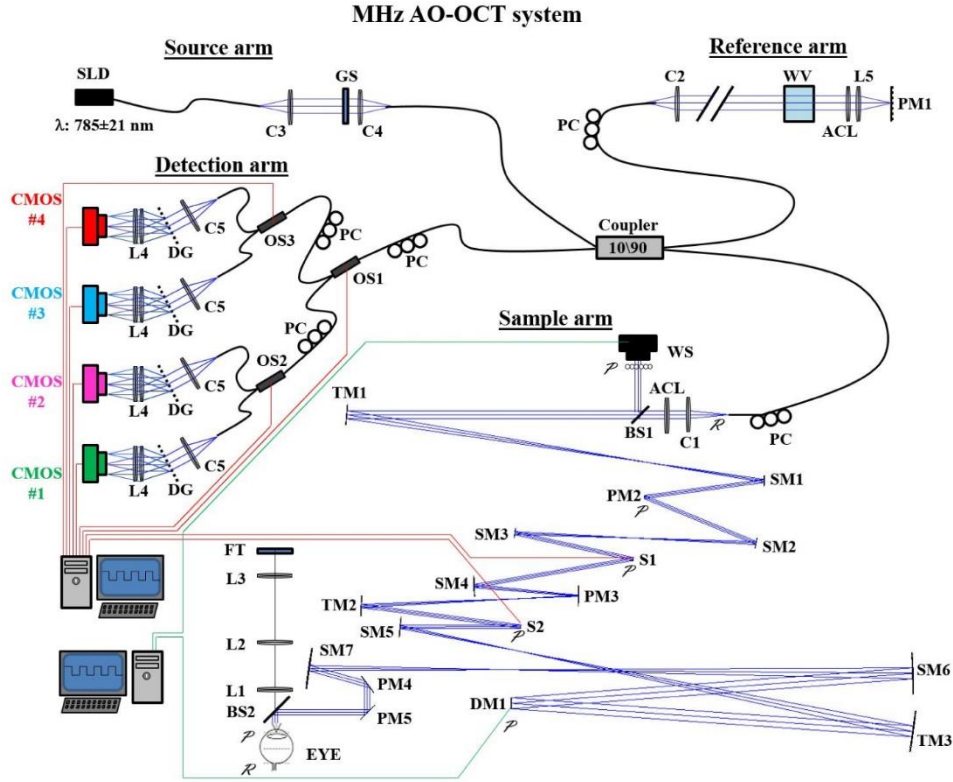
Figure 4.1. Schematic of the MHz HAO-OCT system (located at Indiana University) used in these studies. Key: ACL, achromatizing lens; BS, beam splitter; C, collimator; CMOS, Basler Sprint camera; DG, diffraction grating; DM, deformable mirror; FT, fixation target; GS, glass slide; L, lens; OS, optical switch; PC, polarization controller; PM, planar mirror; P, pupil conjugate plane; R, retinal conjugate plane; S, scanner; SM, spherical mirror; TM, toroidal mirror; WS, wavefront sensor; WV, water vial. Reproduced from [106].

An imaging protocol was developed and tested to achieve both high frame rate and system stability, enabled by the 1 MHz A-line rate. As described in Section 2.4, computational aberration correction requires phase stability within the OCT volume, and it is necessary to image at B-scan frame rates greater than 2.5 kHz due to the rapid involuntary motion of the eye. The imaging protocol operated at a 3.125 kHz frame rate covering a 0.4° x 0.5° field-of-view on the retina (120 µm x 150 µm with transverse step size of 0.5 µm).

Although the scan speed was sufficient to overcome eye motion, it was important to measure the system stability due to the use of galvanometer scanning mirrors at such high frame rates and the fluctuations of the deformable mirror. This was analyzed using a model eye with the HAO system operating with and without closed-loop feedback. Repeated frames were acquired at the same location by fixing the position of the slow-axis scanning mirror. Complex conjugate multiplication was performed between consecutively acquired frames (along the temporal axis), and the result was averaged along both depth and the fast-scanning axis. This canceled out any transverse motion and measured purely axial motion, to which computational OCT is most sensitive. The stability measurement for closed-loop operation is shown in Figure 4.2(a). Following volume phase stabilization (see Table 2.3), the standard deviation of the phase motion was 0.06 radians, well below the previously determined threshold of 0.3 radians.
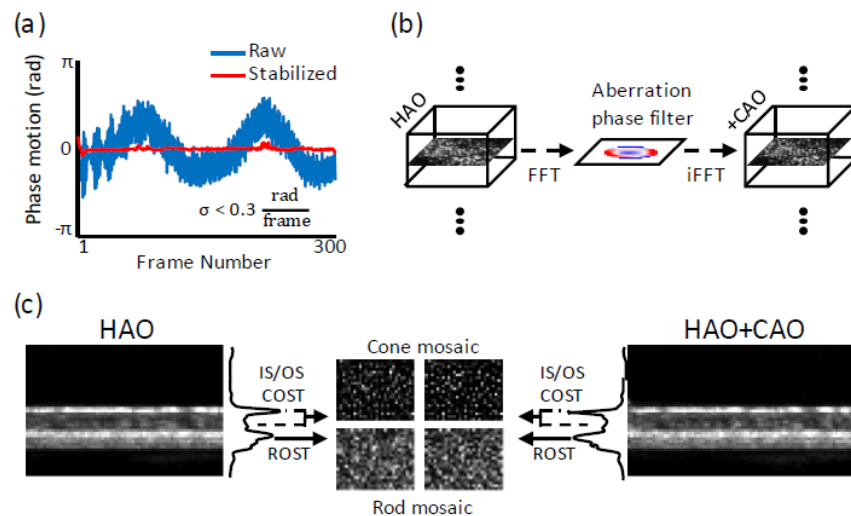
Figure 4.2. (a) Phase stability of the high-speed HAO-OCT scanning protocol acquired from B-M mode data of a model eye. Stabilized data is below the previously determined stability threshold. (b) Illustration of the CAO processing method on a human subject. Each depth plane is optimized independently using an aberration phase filter in the spatial frequency domain. (c) The rod and cone mosaics are extracted from the HAO and HAO+CAO volumes for comparison. The cross-sectional images and depth profiles shown are projections throughout the 3D volume. IS/OS: Inner segment/outer segment junction. COST: Cone outer segment tips. ROST: Rod outer segment tips.

Data was acquired from the right eyes of two healthy male subjects, ages 27 years and 26 years. These are referred to as Subject A and Subject B, respectively. The left eye was covered by a patch, and the right eye was dilated using 0.5% tropicamide. The OCT data was acquired with the HAO system running in closed-loop feedback, and a real-time display was used to place the focus near the cone photoreceptors prior to data acquisition [107]. Imaging was performed at 0.5°, 1°, 3.5°, 7.5°, and 12.5° temporal (T) to the foveal center. All procedures on the subjects adhered to the tenets of the Declaration of Helsinki and were approved by the Institutional Review Board of Indiana University.

Residual aberrations in the HAO-OCT data were corrected using CAO in post-processing. CAO was used to correct each depth layer independently using a phase-only filter in the spatial frequency domain, as illustrated in Figure 4.2(b). Depth layers corresponding to reflections from the photoreceptors were extracted from the HAO and HAO+CAO datasets for direct comparison, as illustrated in Figure 4.2(c). Prior to extracting individual cell layers, the HAO and HAO+CAO data were co-registered to remove any translation introduced by CAO processing, and flattened to remove tip, tilt, and slowly-varying axial eye motion [108,109].

An illustration of the cone and rod photoreceptor cells is shown in Figure 4.3 for reference, corresponding to the cross-sectional images and depth profiles in Figure 4.2(c). OCT measures bright reflections from the cone inner segment/outer segment junction (IS/OS), cone outer segment tips (COST), and rod outer segment tips (ROST). As the IS/OS and COST reflections both originate in the cone photoreceptors, these layers were combined to form a single cone mosaic.
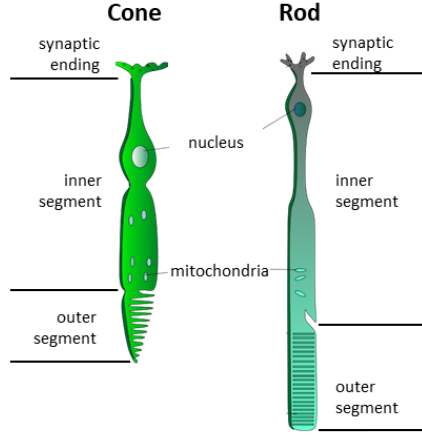
Figure 4.3. Illustration of the cone and rod photoreceptors. OCT reflections originate from the junction of the inner and outer segments of the cone photoreceptor, and the outer segment tips of both the cone and rod photoreceptors. The reflections from the cone IS/OS and COST were combined into a single cone mosaic representing the cone photoreceptor. Modified from [110].

Phase motion in the HAO-OCT dataset was corrected using the axial motion stabilization method outlined in Section 2.4.4, with the modification that the mean is taken along the entire length of the fast-axis. This gives a single phase correction for each fast-axis B-scan. Each depth then underwent additional preprocessing prior to CAO optimization. The Fourier spectrum was centered to remove any linear phase ramp across the *en face* image. This was done by calculating the centroid of the Fourier spectrum. The final preprocessing step was to filter out the remaining phase noise. This was performed sequentially along each dimension by modifying the phase, ϕ_i, at each pixel according to the algorithm

$$\phi_i = \begin{cases} \mathrm{mean}(\phi_{i-1}, \phi_{i+1}), & \text{if } (\phi_i - \phi_{i-1})(\phi_{i+1} - \phi_i) < 0 \\ & \text{and } |\phi_{i-1} - \phi_{i+1}| < \pi \\ \phi_i, & \text{otherwise} \end{cases} . \tag{4.1}$$

The result is a smooth phase profile suitable for CAO processing. The impact of each processing step is demonstrated in Figure 4.4.
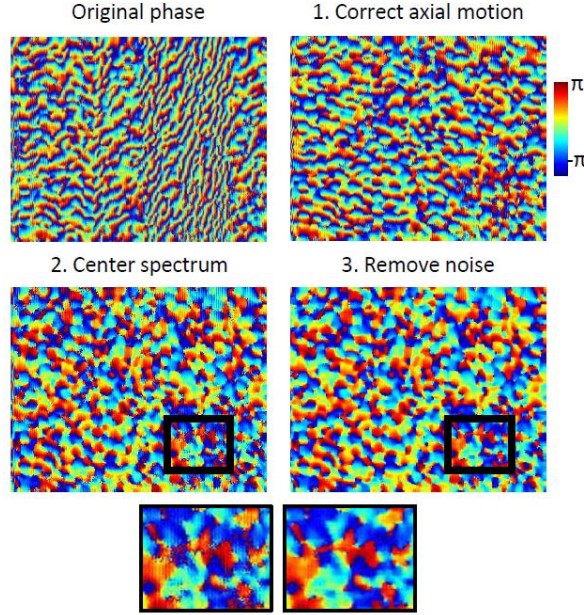
Figure 4.4. Phase of the OCT depth frame for the COST layer at 3.5°T, Subject B, at each of the three CAO preprocessing steps. The original phase data is corrupted by motion and noise. Following the preprocessing steps, motion and noise are corrected to provide phase data suitable for CAO.

The optimal aberration correction filter was determined via stochastic optimization of the image sharpness using the resilient backpropagation procedure outlined in [111]. The CAO phase filter extended to the maximum theoretical cutoff frequency of the confocal system, defined as two times the spatial frequency coverage of the 6.67 mm pupil at the eye [112]. A single correction was used for the entire field-of-view, which is roughly half the size of the expected isoplanatic patch on the retina [113]. The image sharpness metric was calculated from the OCT signal as the sum of the squared intensity,

$$\sum_{x,y}\left[S(x,y)S^*(x,y) \right]^2 . \tag{4.2}$$

The procedure was tested on the COST layer at 12.5°T in Subject B to determine the run time and image improvement for an increasing number of Zernike modes. The maximum Zernike mode was increased from 2nd to 10th order (excluding piston, tip, and tilt), and the optimization was run 10

times at each step. The mean and standard deviation of the run time and image sharpness improvement are shown in Figure 4.5. The optimization was performed on the 300 x 300 pixel image using MATLAB 2015b on an Intel Core i7-6950X processor. Optimization up to 5th order was determined to be a good balance between optimization time and image improvement, and was used as the default setting for processing other retinal datasets.
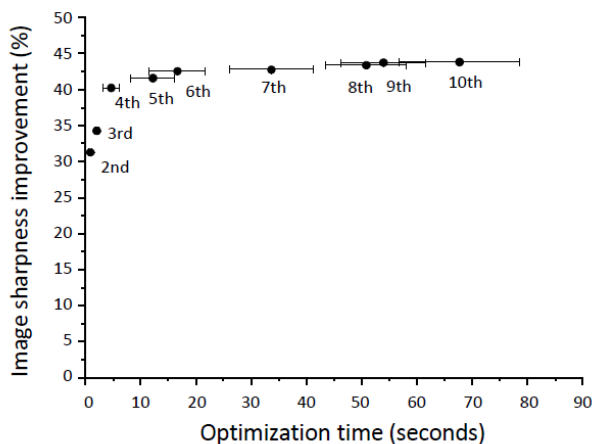
Figure 4.5. Optimization time and image sharpness improvement for different maximum Zernike modes. The mean and standard deviation are shown for 10 trials at each setting.

4.3 Photoreceptor imaging

A representative HAO+CAO dataset is shown in Figure 4.6 which includes all three photoreceptor layers. Because the aberrations of the eye have been corrected, there is both high signal and high resolution throughout the volume.
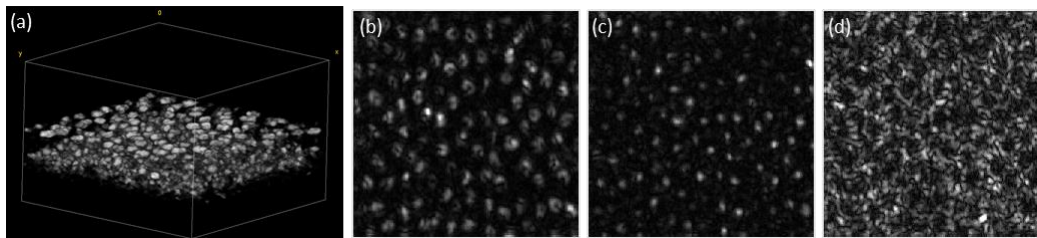
Figure 4.6. Representative HAO+CAO dataset. (a) Volume rendering of the 3D dataset from which the cone inner segment/outer segment junction (b), cone end tip (c), and rod end tip (d) images are extracted.

One of the major benefits of combining HAO+CAO was that the number of collected photons was greatly increased by first physically compensating for aberrations using HAO. Representative images for each variation of HAO and CAO are given in Figure 4.7, showing data at 12.5°T from Subject B, along with the peak SNR in each case. The no-AO image corresponds to a fixed defocus applied to the deformable mirror based upon the subject's glasses prescription (-2 diopter). All images are displayed on a common grayscale to highlight differences in signal level.
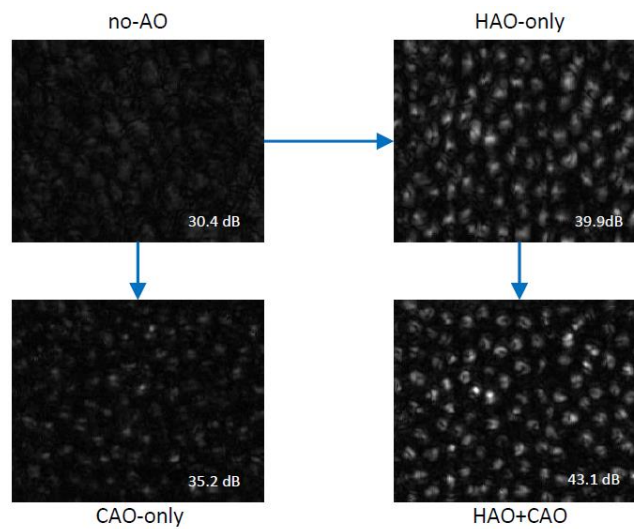
Figure 4.7. Cone mosaic at 12.5°T imaged without adaptive optics, CAO-only, HAO-only, and combined HAO+CAO. All images are displayed on a common grayscale. The peak SNR of each image is given in decibels.

The greatest improvement in SNR came from the addition of HAO, which increased the collected signal by nearly an order of magnitude over the no-AO case. The peak SNR of the CAO and HAO+CAO images was also improved over the no-AO and HAO-only images, respectively, as the computational correction improved the point spread-function (and therefore increased the peak signal). However, the total signal collected remained constant before and after computational correction. While the CAO-only image shows improved resolution, the HAO+CAO image shows both improved resolution and the greatest increase in SNR when compared to the no-AO image, a

12.7 dB increase. Note that in some subjects, the SNR without adaptive optics may be so low that no photoreceptors are visible. In such cases, HAO would be required regardless of CAO use.
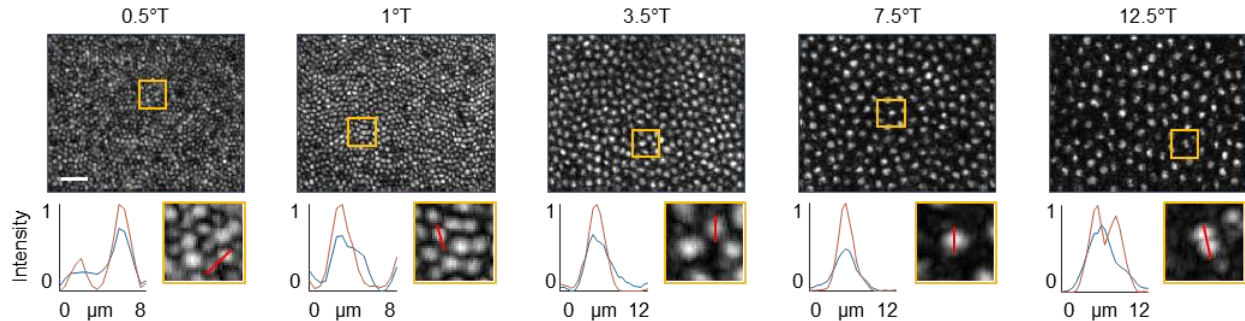
Figure 4.8. HAO+CAO cone photoreceptor mosaic over 0.4° x 0.5° field-of-view at multiple retinal eccentricities from Subject A. The top of each image is toward the fovea (nasal direction), and the fast-scanning axis is along the vertical dimension. Zoomed images correspond to the boxed areas in the cone mosaics. Signal traces are taken through the red lines in the zoomed images. Plots indicate the corresponding HAO (blue) and HAO+CAO (red) signals.

Representative HAO+CAO cone photoreceptor mosaics are shown in Figure 4.8 for each retinal eccentricity, acquired from Subject A. The orientation of the figure is such that top of each image is toward the fovea (nasal direction). Improvement in the visualization of the cones is seen following CAO residual aberration correction. Cones are smallest and most densely packed near the fovea. A signal trace taken through adjacent cones at 0.5°T shows improved resolution with an increase in the peak signal of each cone and a lower minimum between the two cones, a result of improvement in the point spread function and image sharpness. Cones at 1°T, 3.5°T, and 7.5°T show similar improvement, with narrow and symmetric intensity profiles. At greater retinal eccentricities, the IS/OS reflection supports higher-order optical modes [114]. An example of this can be seen in the 12.5°T mosaic, where the higher mode reflection is only revealed following CAO optimization.
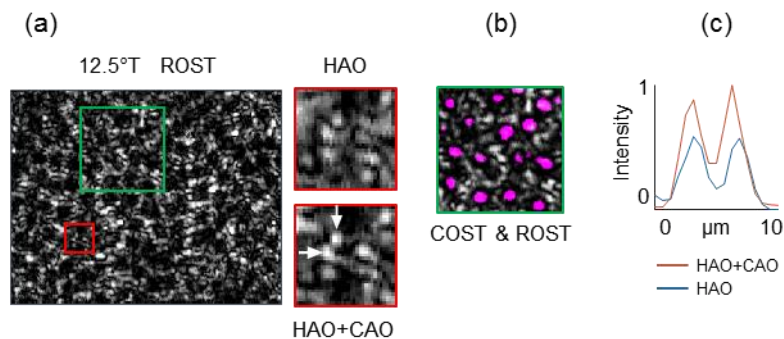
Figure 4.9. (a) HAO+CAO rod photoreceptor mosaic taken at 12.5° temporal to the fovea from Subject A. Zoomed images correspond to boxed areas of corresponding color in the mosaic. Multiple individual rod photoreceptors can be resolved in the HAO+CAO data. (b) Dark patches in the rod mosaic correspond to pseudo-shadows of the cone photoreceptors, demonstrated by presenting the COST in magenta overlay. (c) Trace through the rod photoreceptors indicated by the white arrows in (a).

Because rods are absent near the foveal center and have a density that increases sharply with retinal eccentricity out to between 10° to 20°, these cells were examined at the largest eccentricity imaged (12.5°T). A representative HAO+CAO rod mosaic taken at 12.5°T is shown in Figure 4.9(a), also acquired from Subject A. Following CAO residual aberration correction, multiple individual rods appear resolved as seen in the zoomed region. In addition to the rods themselves, a repeating pattern of dark areas emerges which corresponds to pseudo-shadows of the cone photoreceptors [115,116]. This is confirmed by overlaying the COST layer onto the ROST, shown in Figure 4.9(b), where the COST layer is overlaid in magenta. The trace in Figure 4.9(c) corresponds to the rods highlighted by the white arrows in Figure 4.9(a), indicating that resolution of the rod photoreceptors is improved following CAO. The expected size of the rod photoreceptors is approximately 2 µm, which is slightly below the theoretical diffraction-limited resolution of the imaging system. When imaging objects near the resolution limit with coherent light, interference effects dominate [117]. Consequently, many rods remain obscured by speckle. However, rods which are sufficiently separated appear to be resolved.
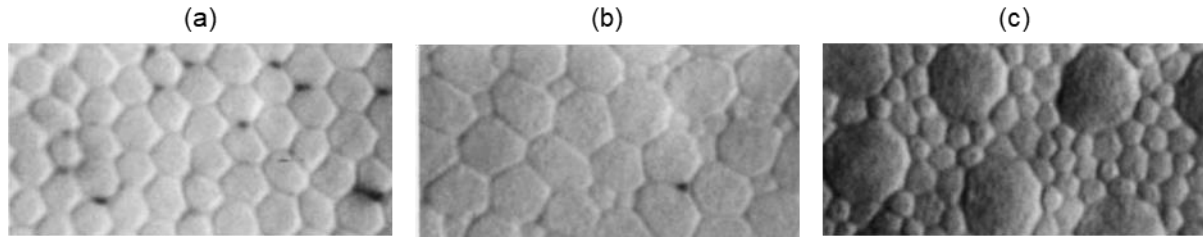
Figure 4.10. Differential interference contrast microscopy photographs of the resected human photoreceptor mosaic at (a) 0.5° from the fovea, (b) 1.5° from the fovea, and (c) far from the fovea. As the eccentricity increases, the size of the cone photoreceptors increases. Rods are more prevalent far from the fovea. The horizontal field of view is 0.125°. Adapted from [118].

Histological sections taken from an excised human retina are shown in Figure 4.10 [113], showing the cones arranged in a densely packed mosaic comparable to the OCT images. As the distance from the fovea increases, the size of the cones also increases as seen in Figure 4.10(a) and Figure 4.10(b). This corresponds to the trend seen in the *in vivo* OCT data of Figure 4.8. Rods are present far from the fovea and fill in gaps in the cone mosaic. There is a strong correspondence between the *in vivo* OCT measurements of Figure 4.9 and the histological images of Figure 4.10(c).

The cone and rod photoreceptor mosaics for Subject B, which are shown in Figure 4.11 and Figure 4.12 for completeness, also follow these trends.
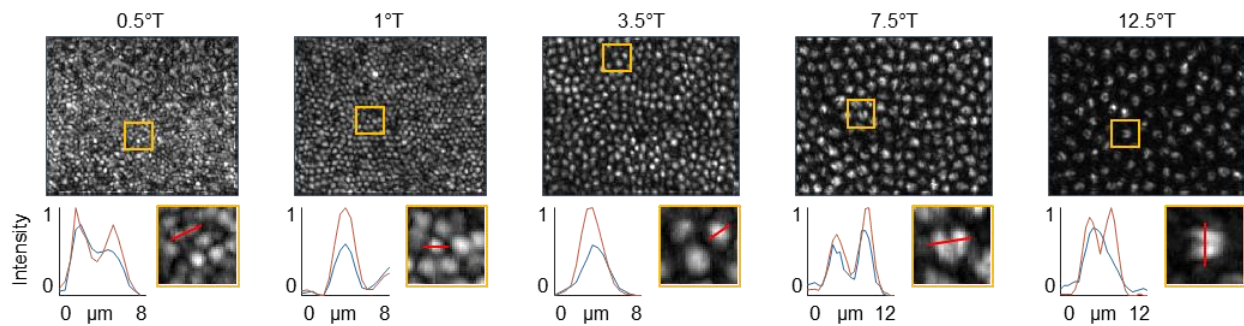
Figure 4.11. HAO+CAO cone photoreceptor mosaic over 0.4° x 0.5° field-of-view at multiple retinal eccentricities from Subject B. The top of each image is toward the fovea (nasal direction), and the fast-scanning axis is along the vertical dimension. Zoomed images correspond to the boxed areas in the cone mosaics. Signal traces are taken through the red lines in the zoomed images. Plots indicate the corresponding HAO (blue) and HAO+CAO (red) signals.
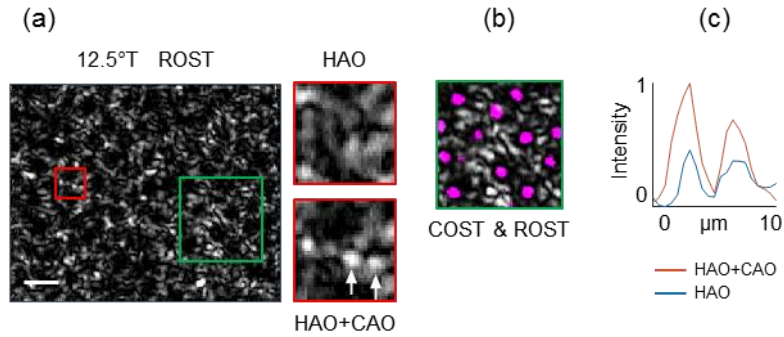
Figure 4.12. (a) HAO+CAO rod photoreceptor mosaic taken at 12.5° temporal to the fovea from Subject B. Zoomed images correspond to boxed areas of corresponding color in the mosaic. Multiple individual rod photoreceptors can be resolved in the HAO+CAO data. (b) Dark patches in the rod mosaic correspond to pseudo-shadows of the cone photoreceptors, demonstrated by presenting the COST in magenta overlay. (c) Trace through the rod photoreceptors indicated by the white arrows in (a).

In addition to being optimized for each eccentricity and depth layer, the CAO correction was also optimized for each time point. Figure 4.13 shows a time sequence of the CAO residual wavefront correction for the peak COST depth layer at 3.5°T, acquired at a volume rate of 10 Hz from Subject B.
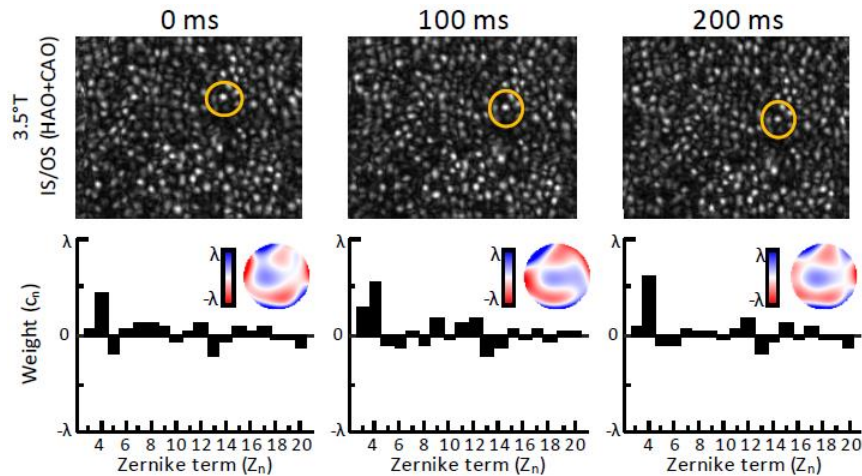
Figure 4.13. Cone photoreceptors at the same location imaged across multiple time-points and the corresponding CAO residual aberration corrections. The optimized CAO Zernike weights (numbered per the ANSI Z80.28 standard [119]) are shown for each time-point, along with the CAO phase filter (without defocus for improved visualization). A single photoreceptor is encircled to aid the reader in tracking the photoreceptor mosaic over time.

The optimized Zernike coefficients reveal temporal dynamics that were left uncorrected by HAO, but corrected with CAO. The residual wavefront corrections appear to vary around a general profile over time. For example, positive defocus (Z_4), negative astigmatism (Z_5), and positive spherical aberration (Z_{12}) are present at each time point. However, the weights vary quite significantly, with many of the other aberrations changing sign as well as strength. The temporal variation in the residual aberration correction is likely due to the temporal dynamics of ocular aberrations [120], which interact with the varying state of the deformable mirror, resulting in a new residual aberration at each time point. Although the exact origin of the dynamic aberrations is uncertain, the magnitude of this variation is dependent on several factors including accommodation and pupil diameter.

The root mean square (RMS) strength of the residual aberrations and the corresponding image sharpness improvement for Figure 4.8 are shown in Table 4.1, corresponding to the peak IS/OS and COST depth layers. The RMS variation was calculated over the spatial frequencies corresponding to the 6.67 mm physical pupil, and is given as a fraction of the central wavelength, λ. Note that there is a non-trivial relationship between residual aberration RMS and sharpness improvement, as each aberration mode has a unique influence upon the value of the metric [121].

TABLE 4.1

RESIDUAL WAVEFRONT RMS AND IMAGE SHARPNESS IMPROVEMENT

	0.5°T	1°T	3.5°T	7.5°T	12.5°T
IS/OS	0.16 λ	0.11 λ	0.27 λ	0.17 λ	0.17 λ
	(9.7%)	(28.3%)	36.6%	45.3%	45.5%
COST	0.14 λ	0.12 λ	0.16 λ	0.12 λ	0.14 λ
	(6.2%)	(17.4%)	36.7%	23.5%	41.2%

The impact of ocular aberrations typically increases with eccentricity, placing a greater burden on the HAO system, which could be shared by CAO. These results follow that general trend, showing more improvement in the image sharpness metric with increasing eccentricity. Another possible influence is the increased difficultly of obtaining optimal alignment of the subject pupil with the HAO system at larger eccentricities.

Improvement in resolution and image sharpness following CAO is not only beneficial for interpretation by human users, but also for automated image analysis. For example, image blur is the primary source of error in automated cone detection algorithms [122]. This is because multiple cones may appear as one due to the broad PSF. Therefore, it was expected that the performance of such algorithms will improve with residual aberration correction. This was tested on the 0.5°T and 1°T cone mosaics from Figure 4.8 using the algorithm of Li and Roorda [123]. The density of cones detected by the automated algorithm increased by 10% and 6.8% at 0.5°T and 1°T from the fovea, respectively. As expected, the increase in detected cones was greatest near the fovea where the cones are most dense.

4.4 Hardware vs. computational actuation

These results were achieved by computationally correcting up to the 20th Zernike mode, while the HAO system corrected up to 70 singular-value modes. Therefore, the residual aberrations do not result from a limited number of modes corrected by HAO but from the accuracy with which the modes are measured and corrected. Calibration error, fitting error, measurement error, and bandwidth error all contribute to the presence of residual aberrations [124]. The computed pupil also has many more adjustable elements, or actuators, than the deformable mirror used in this study, which may partially explain the improvement gained from CAO.

The computed pupil is the spatial frequency domain phase filter used to compensate for aberrations in the OCT data. The number of pixels across the computed pupil is termed the number of computational actuators. The phase of each pixel can be digitally modified using double-precision floating-point numbers, making them equivalent to piston-only actuators with nearly infinite stroke. The computed pupil is circular and extends to the cutoff frequency of the imaging system. Outside this range the CAO filter value is set to one. For the imaging protocol used here, the *en face* image size is 300 x 300 pixels originally acquired with 0.4 x 0.5 µm spacing and 6.67 mm physical pupil. This gives 14,111 piston-only actuators within the computed pupil. For comparison, the Alpao DM 97 used in this study has 97 discrete actuators with approximately Gaussian influence functions, and an inter-actuator stroke of 5 µm.

To achieve equivalent performance using a piston-only corrector, the required number of actuators has been reported to increase by a factor of 10 to 40 depending on pupil size (6 to 7.5 mm) and the extent to which second-order aberrations need correcting [102]. This can be seen in Figure 4.14. The computed pupil has approximately 150 times more actuators than the DM, which is 3.75 to 15 times above what is needed for comparable performance. This suggests the computed pupil will have superior correction performance. However, this should be confirmed in a future study with a direct comparison between HAO and CAO in a controlled setting.
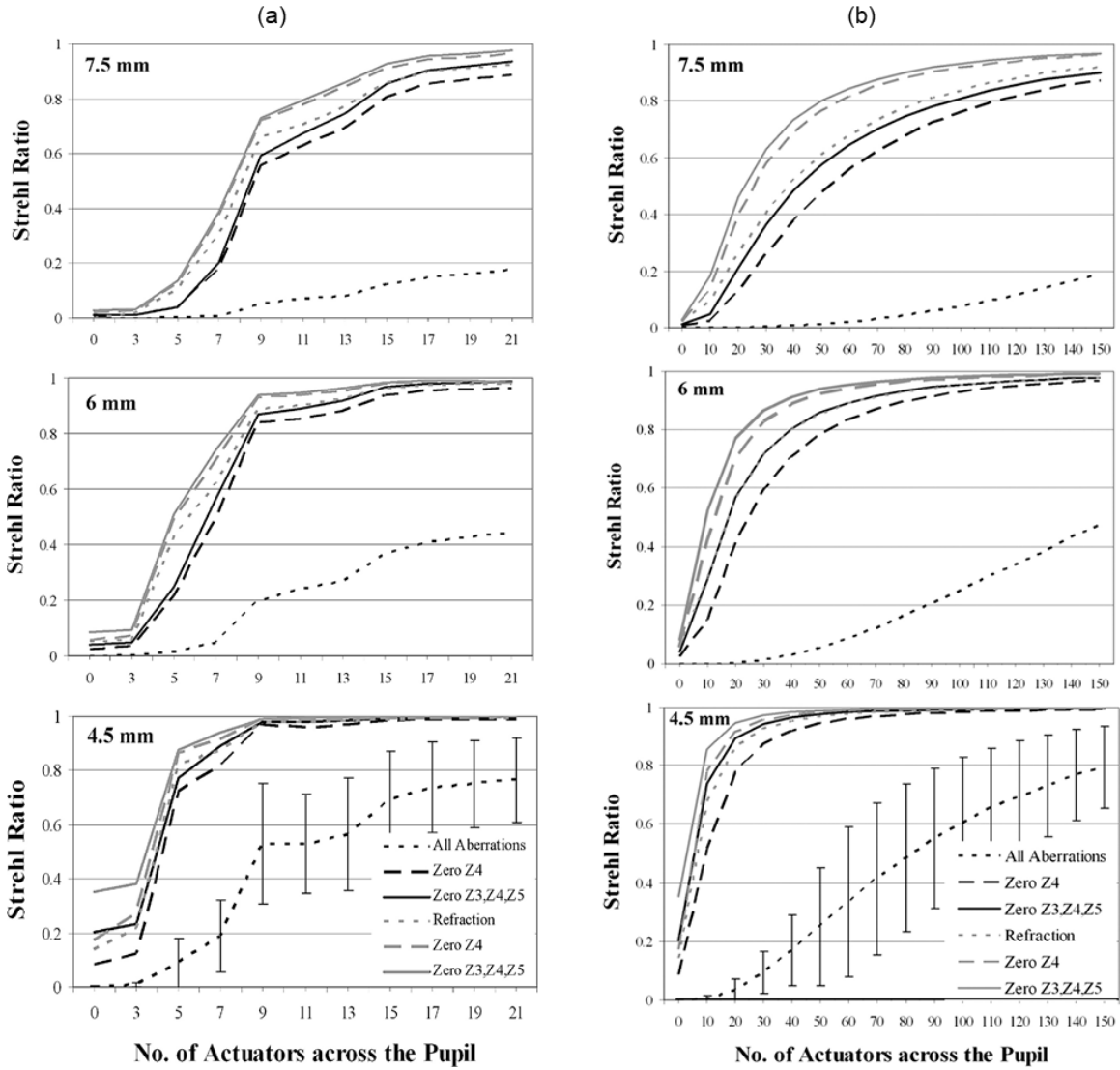
Figure 4.14. Comparison between discrete actuator and piston-only phase correction. (a) Corrected Strehl ratio for discrete actuator deformable mirrors as a function of actuator number across the pupil diameter. (b) Corrected Strehl ratio for piston-only deformable mirrors as a function of actuator number across the pupil diameter. Black curves correspond to data acquired at the University of Rochester. Gray curves correspond to data acquired at Indiana University. The Strehl ratio is a measure of PSF quality, and is equal to 1 for an unaberrated beam. Adapted from [102].

5   COMPUTAIONAL WAVEFRONT MEASUREMENT

5.1   Motivation

In addition to correcting aberrations for improved image resolution, it may also be desirable to measure the aberrations in an image. For example, aberration measurements can be used to determine the flaws in an imaging system design, and 3D mapping of aberrations in biological tissue can be used to optimize system parameters [125]. Wavefront measurement can also be medically relevant, as in aberrometry of the human eye [124], and sample-induced aberrations may prove to be a source of contrast for various tissue types. If the wavefront measurement can be performed computationally, this once again removes the need for a deformable mirror or wavefront sensor.

CAO acts on OCT data in the Fourier domain by a phase-only filter (see Section 2.4.3). However, due to the double-pass nature of the OCT imaging experiment, this CAO correction filter does not directly correspond to the aberrations of the imaging pupil. Previous work has attempted to directly compare the CAO correction filter with the true wavefront measurement acquired with a Shack-Hartmann wavefront sensor [103]. However, the complicated relationship between the pupil wavefront and the CAO correction filter was only explored for defocus, leaving aberrations unaddressed.

This chapter develops and demonstrates new methods for recovering the wavefront aberrations directly from the OCT data itself. These methods have been tested in simulation and experiment to determine sensitivity to induced aberrations, as well as with cross-talk between aberrations. The results are shown to compare favorably with previously published HAO wavefront sensing measurements.

5.2 Computational adaptive optics model

The OCT signal is obtained through interference of backscattered light from the sample with a coherent reference beam, providing complex-valued data for each point within the imaging volume. Detailed derivations can be found in Refs. [42,74], and are followed closely here. Note that the derivation differs slightly from that in Section 2.4, as no asymptotic approximations are yet taken. The complex-valued spectral domain OCT signal is acquired as a function of wavenumber, k, at each transverse scan location, $(x, y) = (\mathbf{r}_{\parallel})$. The focus remains fixed at a certain depth, z_0. The signal $S(\mathbf{r}_{\parallel}, k)$ can then be written as

$$S(\mathbf{r}_{\parallel}, k) = \iint h(\mathbf{r}_{\parallel}' - \mathbf{r}_{\parallel}, z' - z_0, k) \eta(\mathbf{r}_{\parallel}', z') d^2 r_{\parallel}' dz', \tag{5.1}$$

which is the convolution of the system point spread function, $h(\mathbf{r}_{\parallel}, z, k)$, with the sample susceptibility, $\eta(\mathbf{r}_{\parallel}, z)$.

The system point spread function is given as

$$h(\mathbf{r}_{\parallel}, z, k) = k^2 \mid P(k) \mid^2 f(-\mathbf{r}_{\parallel}, z, k) g(-\mathbf{r}_{\parallel}, z, k), \tag{5.2}$$

which is the multiplication of the input and output beam profiles, $f(\mathbf{r}_{\parallel}, z, k)$ and $g(\mathbf{r}_{\parallel}, z, k)$, along with the power spectrum of the laser source, $\mid P(k) \mid^2$. In a standard OCT imaging system, the input and output imaging pupils are the same. The beam profile can be described by a plane wave representation, $G(\mathbf{q}_{\parallel}, k)$. Therefore, both the input and output beam profiles are given by

$$g(\mathbf{r}_{\parallel}, z, k) = \int G(\mathbf{q}_{\parallel}, k) e^{i\mathbf{q}_{\parallel} \cdot \mathbf{r}_{\parallel}} e^{ik_z(\mathbf{q}_{\parallel}, k) z} d^2 q_{\parallel}, \tag{5.3}$$

where

$$k_z(\mathbf{q}_\|, k) = \sqrt{k^2 - \mathbf{q}_\|} \; . \tag{5.4}$$

At the focus ($z = 0$), the beam profile is given by $G(\mathbf{q}_\|, k)$, the Fourier transform of the imaging pupil.

The signal representation in Eq. (5.1) can be simplified by transforming to the spatial frequency domain

$$\tilde{S}(\mathbf{q}_\|, k) = \int \tilde{h}(\mathbf{q}_\|, z' - z_0, k)\eta(\mathbf{q}_\|, z')dz', \tag{5.5}$$

where the (~) denotes the two-dimensional Fourier transform over the lateral scanning dimension. The transfer function is then given as the transverse convolution, denoted as $*_\|$, of the input and output pupil functions in the spatial frequency domain

$$\tilde{h}(\mathbf{q}_\|, z, k) = k^2 \, | \, P(k) \, |^2 \; \tilde{g}(-\mathbf{q}_\|, z, k) *_\| \tilde{g}(-\mathbf{q}_\|, z, k). \tag{5.6}$$

The spatial frequency domain representation of the pupil function is

$$\tilde{g}(\mathbf{q}_\|, z, k) = G(\mathbf{q}_\|, k)e^{ik_z(\mathbf{q}_\|, k)z}, \tag{5.7}$$

which is the imaging pupil $G(\mathbf{q}_\|, k)$ propagated a distance z away from the focus. Aberrations are modeled as phase variations in the imaging pupil, $G(\mathbf{q}_\|, k)$. This leads to an aberrated system transfer function via the auto-convolution operation, as indicated in Eq. (5.6).

In computational adaptive optics, the aberrated system transfer function is corrected by multiplication with a phase-only filter in the spatial frequency domain

$$\tilde{S}_{AC}(\mathbf{q}_\|, k) = H_{AC}(\mathbf{q}_\|, k)\tilde{S}_A(\mathbf{q}_\|, k), \tag{5.8}$$

where

$$H_{AC}(\mathbf{q}_\parallel, k) = e^{-i\phi_h(\mathbf{q}_\parallel, k)}, \tag{5.9}$$

and where subscript "A" indicates the aberrated data, and subscript "AC" indicates the aberration correction filter and aberration corrected data. The phase term $\phi_h(\mathbf{q}_\parallel, k)$ corresponds to the phase of the aberrated system transfer function. Under the assumption that the deviation from the central wavenumber is not too large, meaning $(\Delta k / k_c)^2$ is negligible, the aberration correction filter can be evaluated at the central wavelength and applied at each depth plane, z_i, as

$$\tilde{S}_{AC}(\mathbf{q}_\parallel, z_i) = H_{AC}(\mathbf{q}_\parallel, z_i)\tilde{S}_A(\mathbf{q}_\parallel, z_i), \tag{5.10}$$

where

$$H_{AC}(\mathbf{q}_\parallel, z_i) = e^{-i\phi_h(\mathbf{q}_\parallel, z_i)}. \tag{5.11}$$

This filter can be determined through a variety of procedures including image sharpness optimization, the guide-star method, and the split-aperture method [38,39,45]. These are analogous to sensorless AO, guide-star optimization, and the Shack-Hartmann wavefront sensor in hardware adaptive optics. In any case, the CAO filter corresponds to the double-pass system transfer function.

Through the CAO aberration correction procedure, the phase ϕ_h is obtained. The goal of wavefront measurement is to determine the phase aberrations of the imaging pupil, ϕ_g. The relationship between the pupil and system transfer function is, to within a constant,

$$H(\mathbf{q}_\parallel, z_i) = G(\mathbf{q}_\parallel, z_i) * G(\mathbf{q}_\parallel, z_i), \tag{5.12}$$

where the propagation away from focus in Eq. (5.7) has been absorbed into the single-pass pupil function $G(\mathbf{q}_\parallel, z_i)$. The following section outlines methods for estimating the aberrations of the pupil phase.

5.3 Methods for wavefront measurement

5.3.1 Asymptotic method

A computational method termed interferometric synthetic aperture microscopy (ISAM) solves the OCT inverse problem through asymptotic approximations taken near- and far-from-focus [35,42]. Although these approximations were performed with an unaberrated imaging pupil, it is anticipated that they may hold for small wavefront aberrations. The asymptotic approximations taken in ISAM allow the complex autoconvolution to be represented as a multiplication of stretched pupil functions,

$$H(\mathbf{q}_\parallel, z_i) \approx G\left(\mathbf{q}_\parallel / 2, z_i\right) \times G\left(\mathbf{q}_\parallel / 2, z_i\right). \tag{5.13}$$

For a generic pupil function

$$G(\mathbf{q}_\parallel, z_i) = \left|G(\mathbf{q}_\parallel, z_i)\right| e^{i\phi_g (\mathbf{q}_\parallel, z_i)}, \tag{5.14}$$

the corresponding transfer function under the asymptotic approximation is

$$H(\mathbf{q}_\parallel, z_i) \approx \left|G\left(\mathbf{q}_\parallel / 2, z_i\right)\right|^2 e^{i2\phi_g (\mathbf{q}_\parallel/2, z_i)}. \tag{5.15}$$

The relationship between the strength of aberrations is then simply a factor of two.

The phase aberrations are often represented as a weighted sum of Zernike polynomials [68]. The pupil phase can then be represented by

$$\phi_g(\mathbf{q}_\parallel, z_i) = \sum_n c_n(z_i) Z_n(\mathbf{s}_\parallel), \tag{5.16}$$

where c_n is the root-mean-square (RMS) variation of each corresponding Zernike aberration at depth z_i. Note that for the current model, the pupil aberrations are depth independent, and the propagation away from focus can be approximated using the defocus term Z_4. Therefore, the depth dependence of c_n will be left unnoted for convenience. Also note that the Zernike polynomials exist over the unit circle. Therefore, the coordinates are normalized to extend over the limiting pupil defined by the numerical aperture (NA),

$$\mathbf{s}_\parallel = \left(\frac{\mathbf{q}_\parallel}{k_c \, \mathrm{NA}} \right). \tag{5.17}$$

The transfer function phase determined using CAO with Zernike weights d_n can be similarly represented as

$$\phi_h(\mathbf{q}_\parallel, z_i) = \sum_n d_n Z_n \left(\mathbf{s}_\parallel / 2 \right) \approx \sum_n 2 c_n Z_n \left(\mathbf{s}_\parallel / 2 \right). \tag{5.18}$$

An estimate of the Zernike weights for the pupil aberrations can then be easily obtained as

$$\hat{c}_n = \frac{d_n}{2}. \tag{5.19}$$

This provides a simple relationship between the Zernike weights of the CAO phase filter and imaging pupil.

5.3.2 Autoconvolution method

Instead of relying upon the asymptotic approximations of ISAM, it is possible to retrieve the pupil phase via inverse autoconvolution. In this case, the autoconvolution relationship of Eq. (5.12) still holds. However, the inverse autoconvolution is complicated by the fact that ϕ_h is influenced by

both the amplitude and phase of $G(\mathbf{q}_\parallel)$. Therefore, it is necessary include the pupil function amplitude. Gaussian beam illumination is typical for a point scanned OCT system and will be assumed here, although other amplitude profiles could be used. Passing a Gaussian beam through a limiting circular aperture results in the complex pupil function

$$G(\mathbf{q}_\parallel) = \ \text{circ}(\mathbf{s}_\parallel)\exp\left(-\mathbf{s}_\parallel^2 + i\sum_n c_n Z_n(\mathbf{s}_\parallel)\right). \tag{5.20}$$

Given the phase ϕ_h from the CAO correction and a model for $\left|G(\mathbf{q}_\parallel)\right|$ an optimization procedure can be performed to search for the corresponding pupil phase [126]. The estimated Zernike polynomial weights are calculated by

$$\hat{c}_n = \underset{\phi_g = \sum_n c_n Z_n}{\text{argmin}} \frac{\left\| G(\mathbf{q}_\parallel) * G(\mathbf{q}_\parallel) - \left|G(\mathbf{q}_\parallel) * G(\mathbf{q}_\parallel)\right| e^{i\phi_h} \right\|^2}{\left\| G(\mathbf{q}_\parallel) * G(\mathbf{q}_\parallel) \right\|^2}. \tag{5.21}$$

This finds a pupil function whose autoconvolution has a phase profile that matches the CAO filter.

5.3.3 Forward model method

The above two methods estimate the pupil aberrations from the phase obtained by the CAO image correction. Alternatively, the pupil aberrations can be estimated directly by incorporating the forward model into the CAO procedure. In the absence of aberrations, a group of image metrics known as image sharpness are maximized [79,127,128]. Stated another way, aberrations can only decrease the image sharpness. Therefore, it is possible to determine the appropriate CAO phase filter by maximizing the image sharpness. Here the image sharpness operator is defined as

$$\mathcal{I}\left(S(x,y)\right) = \sum_{x,y}\left[S(x,y)S^*(x,y)\right]^2, \tag{5.22}$$

where (*) indicates the complex conjugate. This operator calculates the sum of the intensity squared across the image.

Typically, the image sharpness is optimized by searching over possible phases ϕ_h, in accordance with Eqs. (5.10) and (5.11). However, it is possible to generate the CAO phase filter via the forward model as

$$H_{AC}(\mathbf{q}_\parallel) = \exp\left(-i\arg[G(\mathbf{q}_\parallel) * G(\mathbf{q}_\parallel)]\right). \tag{5.23}$$

The image sharpness optimization can then be performed by searching over possible phases ϕ_g, providing a direct estimate of the imaging pupil phase

$$\hat{c}_n = \underset{\phi_g = \sum_n c_n Z_n}{\operatorname{argmax}} \mathcal{I}\left(\mathcal{F}^{-1}[S_{AC}(\mathbf{q}_\parallel)]\right). \tag{5.24}$$

where $\mathcal{F}^{-1}$ indicates the inverse Fourier transform to the spatial domain.

5.4 Sensitivity and cross-talk

To determine the effectiveness of each method, OCT data was simulated allowing for the introduction of arbitrary aberrations into the imaging pupil. The data used here was generated using the more exact model of Eqs. (21) and (29) from [42]. Simulated data were generated on a densely spaced 3D grid, then resampled by a non-integer multiple to a coarser grid to mimic data acquisition.

The simulated OCT experiments used a Gaussian spectrum with 1 µm central wavelength and 100 nm bandwidth, and the transverse imaging area was 128 x 128 µm acquired with a 1 µm step size. The numerical aperture was 0.1, matching that of previous computational OCT

experiments [17,38]. The imaging pupil was constructed following Eq. (5.20), with aberrations introduced into the pupil phase using weighted Zernike polynomial functions

$$\phi_g(\mathbf{q}_\parallel, k) = k \sum_n c_n^{(\mu m)} Z_n \left(\mathbf{q}_\parallel / (k\,\mathrm{NA}) \right).$$ (5.25)

Here c_n was defined in units of micrometers (μm), corresponding to optical path length, and the variation in wavenumber was explicitly accounted for in the simulation. The image sharpness optimization and inverse autoconvolution procedures were performed in MATLAB using the Optimization Toolbox.

To determine the sensitivity to each aberration term, as well as the cross-talk between terms, single aberrations were applied in the imaging pupil with increasing RMS. The imaging sample consisted of in-focus unit-amplitude point scatterers, and aberrations up to 4th order were applied (excluding tip/tilt and defocus) with RMS increasing from zero to 0.6 radians at the central wavelength. The applied aberrations were then estimated from the OCT data using each of the three methods.

For the asymptotic and forward model methods, the wavefront was estimated by correcting up to 4th order Zernike terms (excluding tip/tilt). However, as a result of the autoconvolution operation, the phase of the system transfer function is more rapidly varying than that of the imaging pupil. This means that while ϕ_g is described accurately by Zernike terms up to 4th order, ϕ_h may not be. The transfer function phase is represented more accurately as more Zernike modes are used. It was experimentally determined that the CAO optimization performed as the first step in the autoconvolution method must include up to at least 6th order Zernike modes. This provides an approximation of ϕ_h that is sufficiently accurate for performing the inverse autoconvolution operation to 4th order imaging pupil aberrations, and was used for the results presented here.

The sensitivity was defined as the slope of the linear least-squares fit between the estimated weights, c_n corresponding to applied weights, c_n. The cross-talk was defined as the normalized RMS variation in all aberration terms other than the applied term,

$$\frac{\left(\displaystyle\sum_m \hat{c}_{m \neq n}^2\right)^{1/2}}{c_n}, \qquad (5.26)$$

evaluated at the maximum applied aberration. A perfect estimate would result in sensitivity equal to one and cross-talk equal to zero [52].
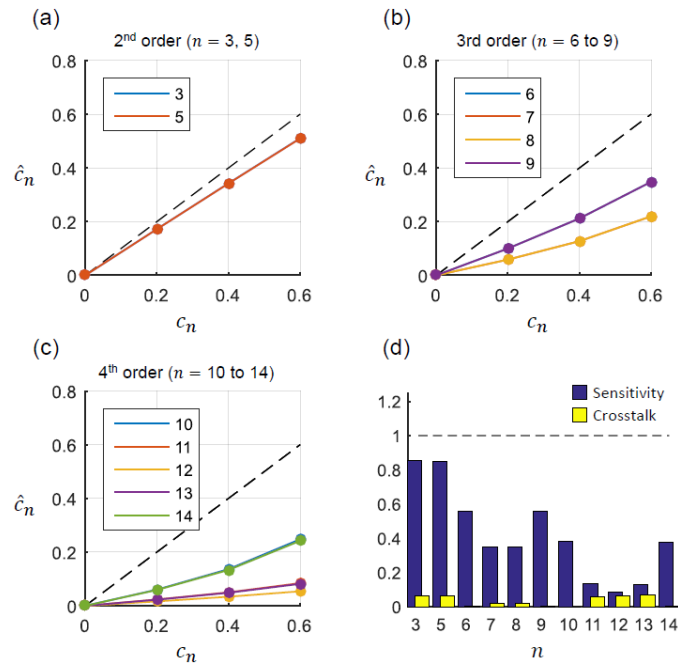
Figure 5.1. Measurement of single aberrations using the asymptotic method. The applied and estimated Zernike weights are shown for 2nd, 3rd, and 4th order aberrations (a-c). The dotted line corresponds to a perfect estimate. All Zernike weights are in radians. The sensitivity and cross-talk were calculated for each applied Zernike term (d).

Aberration estimates obtained using the asymptotic approximation are shown in Figure 5.1. In Figure 5.1(a)-(c), the estimated weights are given for 2nd, 3rd, and 4th order, respectively. An ideal estimate is indicated by the dashed line for reference. Notice that certain Zernike modes are nearly

identical, differing only in their rotation (for example astigmatism terms $n = 3, 5$). Therefore, the estimates for these terms are very close to one another. The sensitivity and cross-talk for each applied term are shown in Figure 5.1(d). There is reasonable performance only for 2nd order aberrations, indicating that the asymptotic approximation is not valid at higher orders.
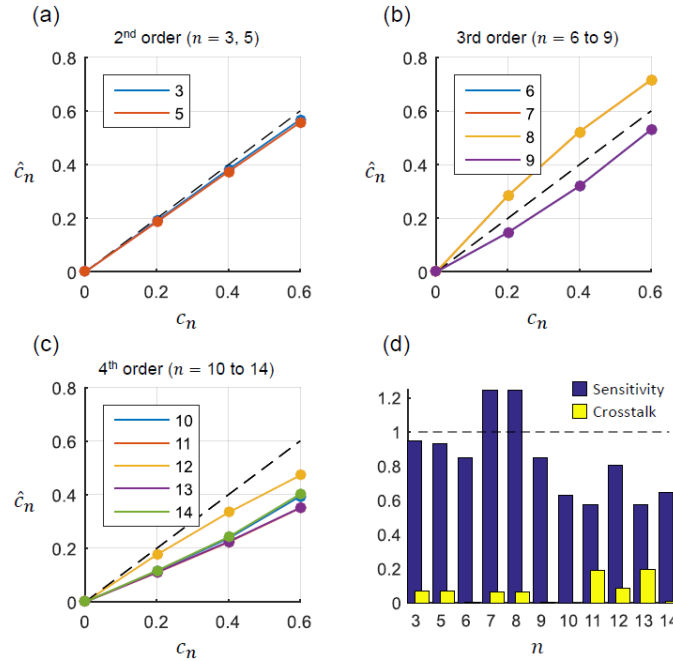
Figure 5.2. Measurement of single aberrations using the autoconvolution method. The applied and estimated Zernike weights are shown for 2nd, 3rd, and 4th order aberrations (a-c). The dotted line corresponds to a perfect estimate. All Zernike weights are in radians. The sensitivity and cross-talk were calculated for each applied Zernike term (d).

The inverse autoconvolution method showed superior sensitivity at all orders when compared with the asymptotic method. The aberration estimates and corresponding metrics are given in Figure 5.2. The sensitivity at 2nd order was 0.95, and remained greater than 0.5 through 4th order. For coma (terms $n = 7, 8$), the method overestimated the applied aberration, but the sensitivity remained within 0.25 of the ideal case.
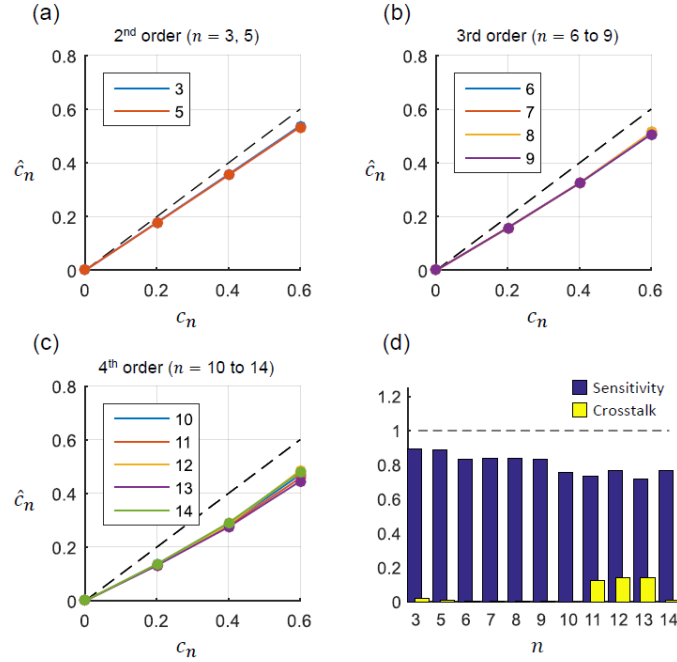
Figure 5.3. Measurement of single aberrations using the forward model method. The applied and estimated Zernike weights are shown for 2nd, 3rd, and 4th order aberrations (a-c). The dotted line corresponds to a perfect estimate. All Zernike weights are in radians. The sensitivity and cross-talk were calculated for each applied Zernike term (d).

Of the three proposed methods, the forward model method had the most consistent performance across all orders as demonstrated in Figure 5.3. Additionally, the method did not overestimate any aberrations. The average sensitivity across all terms was 0.81, while the average cross-talk was equal to 0.04.

The imperfection of the CAO measurement can be partially explained by the fact that it is a phase-only filter. Although the pupil aberrations are phase-only, the autoconvolution of Eq. (5.12) causes the pupil phase to couple into the amplitude of the system transfer function. As a result, the system transfer function cannot be completely corrected using a phase-only CAO filter. In some cases, the amplitude of the system transfer function will have zero values, meaning certain spatial frequencies are not measured.
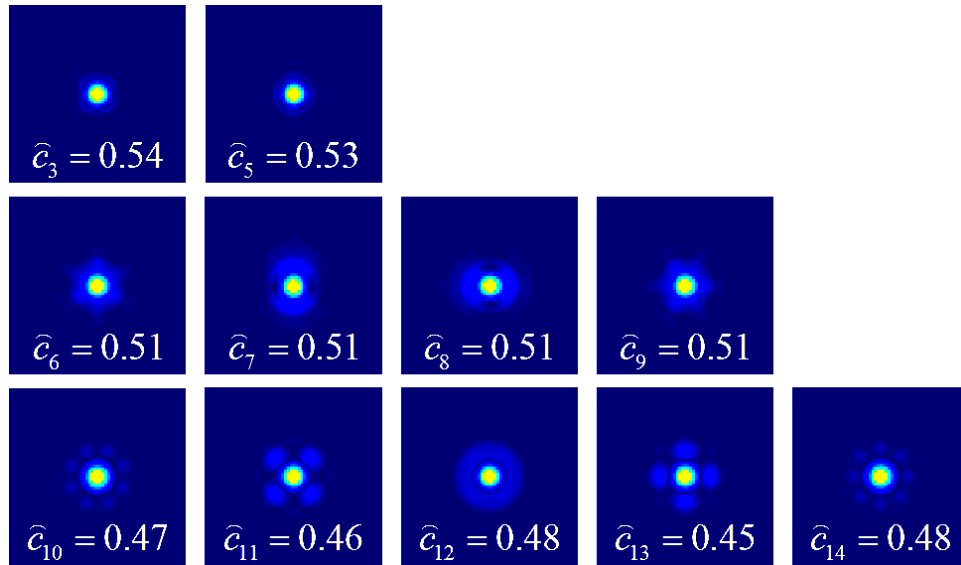
Figure 5.4. Corrected point spread function and measured Zernike weights using the forward model method for applied 0.6 radians RMS. Note that as the aberration order increases, the corrected point spread function retains some sidelobes, and the measurement is less accurate. Image contrast is exaggerated to increase sidelobe visibility.

The corrected point spread function using the forward model method is shown in Figure 5.4. For each Zernike term, the computational correction is imperfect. As the complexity of the aberrations increases, the sidelobes in the corrected PSF are more prominent. This is most severe for Zernike terms 11, 12, and 13, which also have the poorest aberration measurement performance for all three of the proposed method (see Figures 5.1, 5.2, and 5.3). Despite this limitation, phase-only correction is still preferable as it is simpler and does not amplify the noise power. Amplitude correction is significantly more complicated and is only expected to give moderate improvement, as the band-stop effect of the double-pass transfer function cannot be undone even with a regularized inverse.

In a realistic imaging scenario, the data will be corrupted by noise. For OCT this can be modeled by additive complex white Gaussian noise [42,129]. The simulations and measurements of the previous section were repeated with peak signal-to-noise ratio (SNR) varying from 50 dB down to 20 dB, where the peak SNR was defined as

$$\text{SNR}_{\text{peak}} = 10\log_{10}\left(\frac{\max|S(\mathbf{r}_\parallel)|^2}{\sigma_{\text{noise}}^2}\right).$$
(5.27)

The resulting sensitivity and cross-talk for the autoconvolution and forward model methods are shown in Figure 5.5. As the asymptotic method is not sensitive to higher orders, the results are not included. Although the computational wavefront measurement fails below a certain SNR threshold, it is important to note that the computational image correction still succeeds. This is in accordance with previous results [80].

At high SNR, both methods performed similarly to the noise-free case. However, as the SNR decreases, the tails and sidelobes of the point spread function become buried in the noise. Therefore, much of the point spread function shape can be obscured. The performance of the autoconvolution method began to suffer with peak SNR of 30 dB, where cross-talk approached the sensitivity for several aberration terms. At 20 dB peak SNR, the results became unstable with estimated RMS far beyond that which was applied.

The performance of the forward model method remained strong down to 25 dB peak SNR. Here the average sensitivity was 0.81, and average cross-talk was 0.29. A comparable experiment was previously performed using a deformable mirror and Shack-Hartmann wavefront sensor [52]. The average sensitivity and cross-talk were 0.71 and 0.32, respectively, and only included aberrations up to 3rd order. Considering this, the performance of the forward model method was comparable or superior to that of direct hardware measurement.
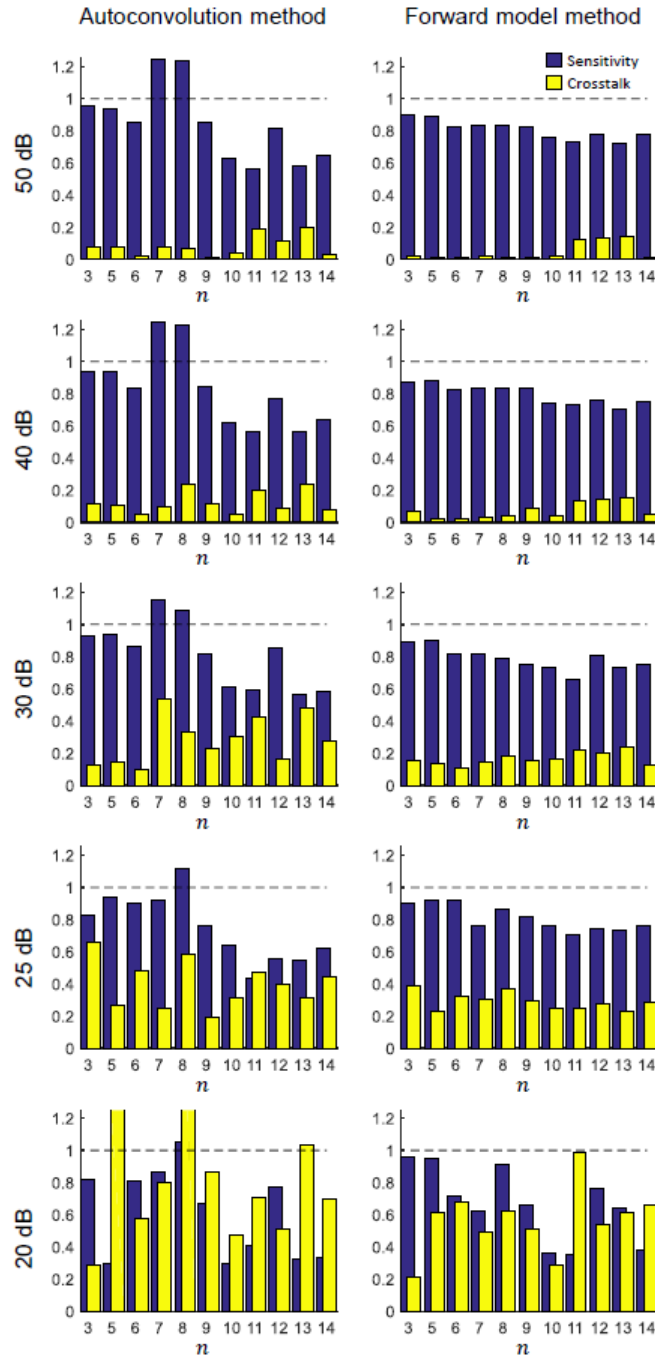
Figure 5.5. Performance of the autoconvolution and forward model methods for decreasing peak SNR. The forward model method shows superior performance in noisy conditions.

5.5　Multiple simultaneous aberrations

Additional simulated experiments were performed with multiple aberrations applied simultaneously in the pupil plane. The aberration weights were randomly generated to have a total wavefront RMS of zero, 0.2, 0.4, and 0.6 radians, with lower-order Zernike terms allowed to take on greater weights. The total wavefront RMS is defined as

$$\sigma = \left(\sum_n c_n^2 \right)^{1/2}. \tag{5.28}$$

A total of ten random wavefronts were generated at each RMS, and OCT data was simulated for each wavefront. The noise level was set to 50 dB peak SNR. Due to its consistent performance across all orders and resilience to noise, the forward model method was used to estimate the applied wavefronts.
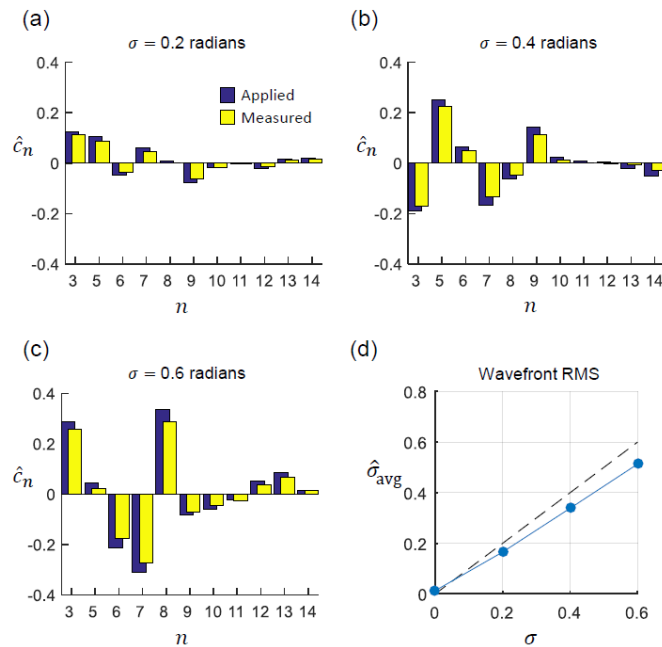
Figure 5.6. Measurement of multiple simultaneous aberrations using the forward model method. The applied and measured Zernike weights are shown for a randomly generated wavefront at 0.2, 0.4, and 0.6 radians RMS (a-c). The average wavefront RMS measured over ten randomly generated wavefronts is shown in (d). The corresponding sensitivity to total wavefront RMS was 0.85.

Example wavefronts and the corresponding computational measurements are shown in Figure 5.6. As seen in Figure 5.6(a)-(c), the measurement closely tracked the applied wavefront. For each wavefront, the total RMS of the measured aberrations was calculated. The average measured RMS across each set of ten wavefronts is shown in Figure 5.6(d). The sensitivity was 0.85, calculated as the least squares slope of the total measured RMS as a function of applied RMS.
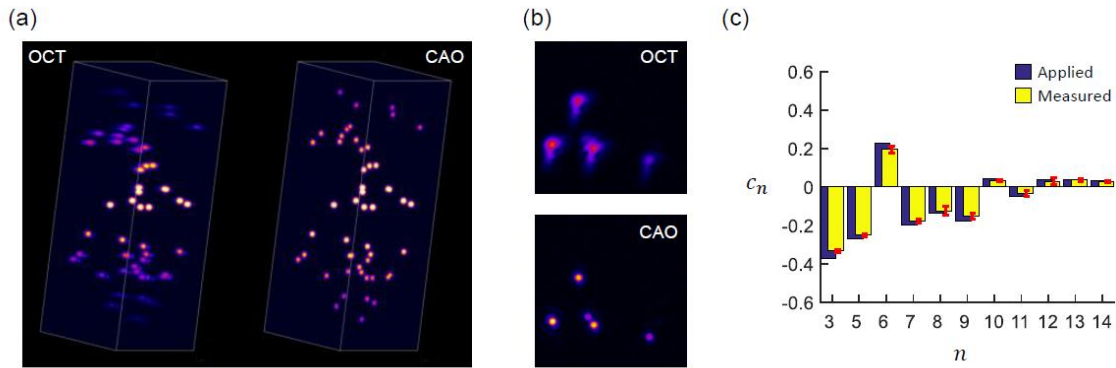
Figure 5.7. Measurement and correction of multiple aberrations in a 3D imaging volume. (a) Volume rendering of aberrated (OCT) and corrected (CAO) data. The dimensions of the volume are 128 x 128 x 640 µm. (b) *En face* images are taken from 150 µm below focus. (c) Applied and measured aberrations at each point scatterer throughout the volume. The error bars correspond to the standard deviation across all 50 measurements. Zernike weights are in radians.

As a demonstration of volumetric aberration measurement and correction, a 3D OCT dataset was generated with 50 randomly located point scatterers. The pupil aberrations were given by a randomly generated wavefront of 0.6 radians total RMS. The forward model method was used to estimate and correct the aberrations throughout the imaging volume. Volume renderings of the aberrated OCT data and CAO corrected data are shown in Figure 5.7(a), along with corresponding *en face* images taken 150 µm below focus. The CAO image demonstrates correction of the point spread function with increased signal amplitude and resolution, and a 3.9 times improvement in image sharpness (see Eq. (5.22)). In this case, the sharpness metric was normalized by the total intensity of each image. While only four points are resolved in this OCT image, a previously obscured fifth point is revealed following wavefront correction. The applied and measured

aberration weights are given in Figure 5.7(c), showing the mean and standard deviation of the wavefront measurement across all 50 scatterers. The average sensitivity to the total wavefront RMS was 0.89.

5.6   Experimental demonstration

5.6.1   Verification using hardware adaptive optics

A hardware adaptive optics OCT system was used to experimentally verify the computational wavefront measurement. The system was previously used for CAO imaging [76], and was modified to include both a deformable mirror (mirao-52e, Imagine Optics) and wavefront sensor (HASO3 First, Imagine Optics). The DM consisted of 52 discrete elements to push and pull a reflective membrane. The wavefront sensor was a Shack-Hartmann design with 40 x 20 lenslets.
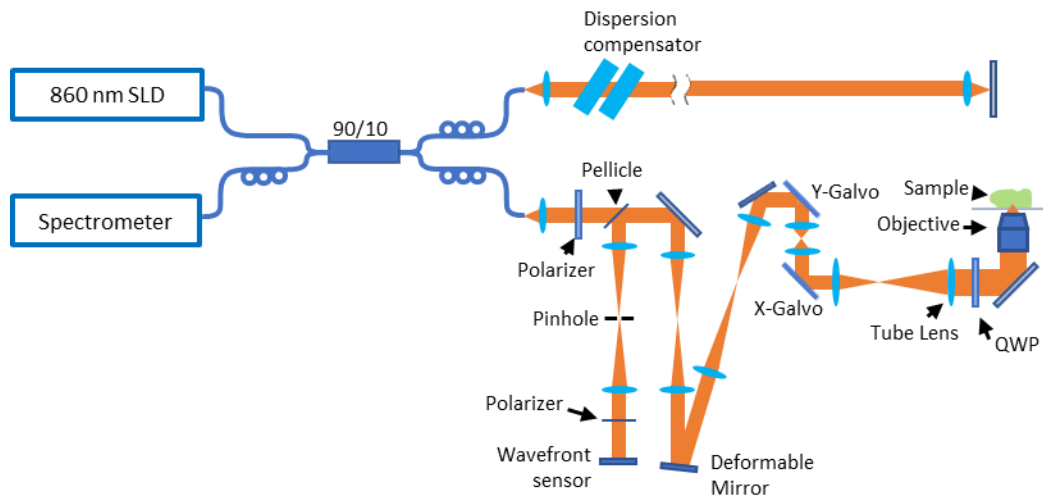
Figure 5.8. Lens-based hardware adaptive optics OCT system. The sample arm includes a deformable mirror and wavefront sensor to measure and correct optical aberrations. A pinhole and polarization control are used to reject backreflections from the lens surfaces.

The HAO-OCT system diagram is shown in Figure 5.8. Most HAO systems, including the system detailed in Section 4.2, are constructed using mirrors rather than lenses. This is because backreflections from lenses can cause a dynamic background signal on the wavefront sensor which

can overpower the weak signal from the sample. However, the disadvantage of a mirror-based system is its complexity. A mirror-based system requires out-of-plane alignment or custom manufactured mirrors to avoid introducing strong aberrations [105]. A lens-based system can be more easily aligned.

Polarization-control was used to reject backreflections from the lenses. The input light was sent through a polarizer, and an orthogonal polarizer was placed immediately in front of the wavefront sensor. Backreflections were polarized identically to the input light, and therefore blocked from reaching the wavefront sensor. To allow sample backreflections to reach the sensor, a quarter-wave plate was placed immediately before the objective lens, oriented at 45° to the input polarization. Assuming no sample birefringence, light reflected from the sample passed through the waveplate a second time and was polarized orthogonal to the input (see discussion in Section 3.3). The backscattered signal from the sample was then able to pass the polarizer at the wavefront sensor.

Unfortunately, there is also a strong backreflection from the objective lens. The physical size of the quarter-wave plate requires that it be placed prior to the objective. Therefore, backreflections from the objective will also have a rotated polarization and be able to pass to the wavefront sensor. To help mitigate this problem, and to block any other reflections not sufficiently removed by polarization control, a pinhole was placed at the focus of the 4f system in the wavefront sensor path. This was adjusted to block as much of the backreflected signal as possible, without blocking the signal from the sample. Lastly, a background wavefront sensor image was taken and subtracted from future measurements.

White printer paper secured to a microscope slide was used as a highly scattering sample to calibrate the HAO system. Using the Imagine Optics control software, the interaction and command matrices describing the relationship between the DM actuators and wavefront sensor measurement were calculated. By using the strongest 75% of the eigenmodes, the HAO system achieved diffraction-limited performance ($< \lambda/14$ wavefront RMS) in closed-loop feedback.

To test the forward model wavefront measurement method, a point-scattering tissue phantom was first imaged with a flat DM profile. The aberrations of this image were measured to provide a reference point for the inherent system and sample aberrations. Second and 3rd order aberrations were then introduced using the Imagine Optics control software with increasing RMS of 0.05 µm, 0.10 µm, and 0.15 µm. The aberrations in each of these images were measured, and the change in Zernike weights from the reference image were calculated, with the exception of the 0.15 µm coma dataset which was excluded due to insufficient SNR. Because the coordinate systems of the HAO system and the OCT data may be rotated with respect to one another, the total RMS in each measured aberration "type" was calculated. For example, the measured astigmatism was calculated as the total RMS change in Zernike terms 3 and 5, corresponding to oblique and vertical astigmatism. This removed the effect of coordinate system rotation.

The results are shown in Figure 5.9. The OCT reference image is shown, along with an example aberrated image. The sensitivity and cross-talk were calculated as defined in Section 5.4, with the exception that defocus was not included in the cross-talk calculation. This is due to the fact that undesired defocus was introduced by the DM. This can be seen in Figure 5.9(b) where defocus is added in addition to the intended 0.10 µm of coma. The difference between the intended and actual applied aberration is attributed to the non-common path relationship between the OCT signal and the wavefront sensor measurement. As shown in Figure 5.8, the wavefront sensor path contains an

additional 4f system not present in the OCT path. Therefore, a flat wavefront at the wavefront sensor does not correspond to a flat wavefront at the OCT sample fiber. While higher-order non-common path aberrations are likely present, the strongest and most likely mismatch is defocus due to inaccuracy in the 4f system alignment. The average cross-talk was 0.53 including defocus and 0.23 excluding defocus.
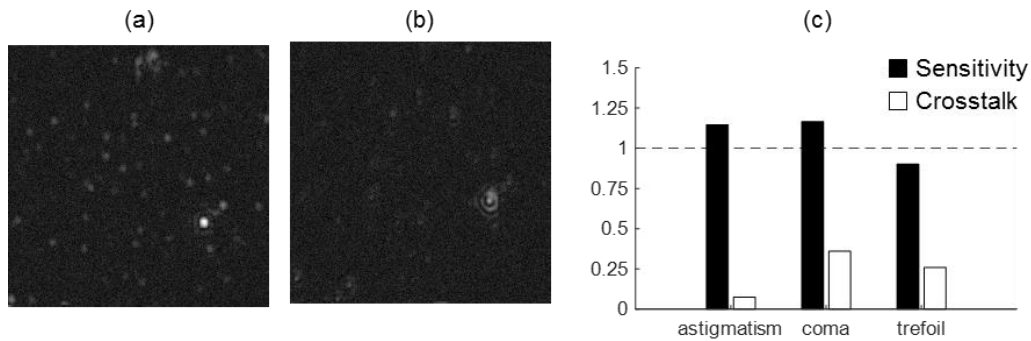
Figure 5.9. Experimental verification of the forward model method. (a) OCT reference image acquired with a flat deformable mirror. (b) Example aberrated OCT image acquired with 0.10 µm of induced coma, showing both coma and defocus aberration. (c) Sensitivity and cross-talk of the aberration measurement using the forward model method. Change in defocus was excluded as a non-common path aberration. Field-of-view is 75 x 75 µm in (a,b).

In contrast with previous simulations, the sensitivity was greater than one, rather than less than one. This can be attributed to an overestimation of the pupil size. A larger pupil size will require larger Zernike weights to generate the same phase profile. Because the imaging sample was composed of subresolution point-scatterers, the NA could be estimated directly from the power spectrum of the image data. The double-pass cutoff frequency was estimated as the -20 dB point, excluding the peak DC value, and was assumed to be twice the single-pass cutoff frequency. This is the best-case scenario for confocal imaging. In reality, the double-pass cutoff may be less than twice the single-pass cutoff, leading to a slight overestimation of the pupil size. Using this method, the average sensitivity was 1.07.

5.6.2 Wavefront measurement in tissue

The forward model wavefront measurement and correction method was then applied in biological tissues. Imaging was performed with a 1300 nm OCT system used in several previous studies [82]. As the sample structure may affect the power spectrum of the data, the nominal NA of 0.075 was used, rather than estimating the NA from the power spectrum.

The local wavefront was estimated within a 200 x 200 µm window. The choice of window size was determined by two factors. First, the window size must be large enough to include the entire aberrated point spread function. Second, it must be large enough to include sufficient structural information such that the sharpness metric is not dominated by speckle nose [128]. A window of 200 µm was experimentally determined to be appropriate for this imaging system across multiple samples of interest. Additionally, negative entropy was used as the image sharpness metric during optimization. A detailed definition and justification of this metric are presented below.
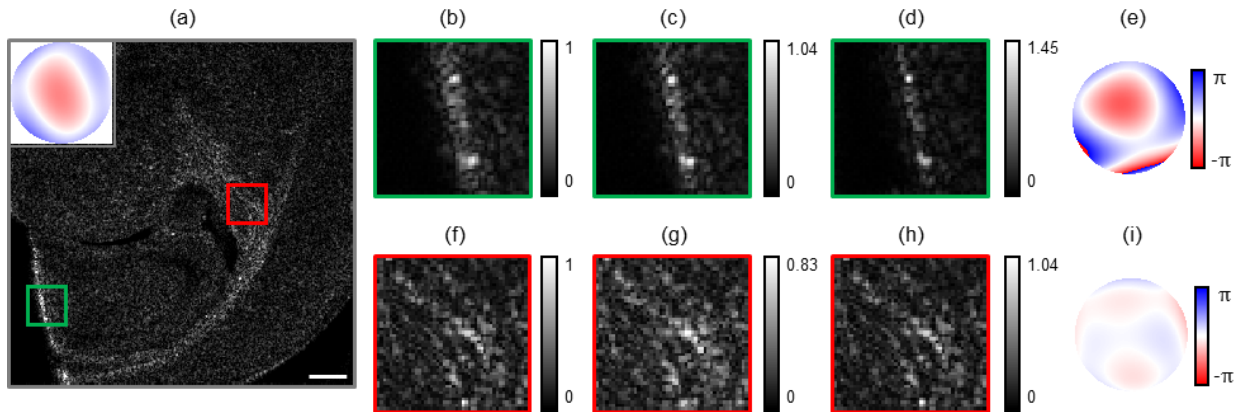
Figure 5.10. Measurement and correction of aberrations in *ex vivo* mouse brain slice. (a) Corrected depth image when CAO is applied to the entire field-of-view. Inset shows the global wavefront. (b,f) Uncorrected OCT subimages 1 (top) and 2 (bottom) corresponding to the boxed regions in (a). Image intensities are normalized to the peak signal of the uncorrected OCT subimages. (c,g) Globally corrected subimages using the wavefront from (a). (d,h) Locally corrected subimages. (e,i) Local wavefront measurements corresponding to the two subimages. Scale bar and subregion widths are 200 µm.

To demonstrate the importance of local wavefront measurement, Figure 5.10 shows global and local aberration correction in the *ex vivo* mouse cortex. Because the aberrations vary across the field-of-view, a global CAO correction may improve one region while degrading another. With a local measurement, each region can be improved independently. This is quantified in Table 5.1, where the improvement in the intensity squared sharpness metric is given for the entire field-of-view and the two subregions indicated in Figure 5.10. Subimage 1 (top), which corresponds to the edge of the hippocampus, is aberrated and out of focus. This biases the global correction to degrade subimage 2 (bottom), which corresponds to myelinated nerve bundles near focus and therefore relatively unaberrated. A local measurement takes this variation into account and achieves a better result for both subimages.

TABLE 5.1

IMAGE SHARPNESS IMPROVEMENT FOR GLOBAL AND LOCAL CORRECTION

	Full FOV	**Subimage 1**	**Subimage 2**
Global correction	10.5%	30.0%	-14.8%
Local correction	--	83.0%	1.3%

This local measurement can be performed across the entire imaging region to generate an aberration map. This provides insight into how the tissue itself impacts the optical wavefront, and therefore the image quality. Figure 5.11 shows the spatial variation of the local wavefront within *ex vivo* chicken breast. This was calculated using a 200 x 200 µm sliding window with 33.6 µm step size, totaling 55 x 55 wavefront measurements. The surface of the muscle tissue was uneven. As a result, the imaging beam at a given depth plane traveled through varying amounts of tissue across the field-of-view. The wavefront RMS is much greater where the beam traveled through more tissue. This can be seen in the gradient of the wavefront RMS in Figure 5.11(c). This demonstrates that different paths through the same tissue type can cause variation in optical wavefront.
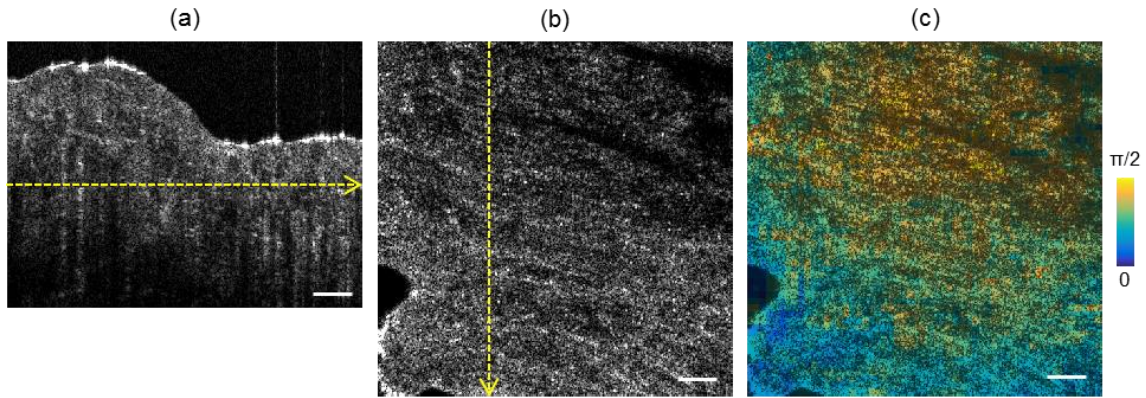
Figure 5.11. Wavefront measurement and correction in *ex vivo* chicken breast. (a) OCT cross-section showing uneven tissue surface. (b) Composite depth image of locally corrected subimages, taken at the depth plane indicated by the yellow line in (a). (c) Map of the local wavefront RMS across the depth image (b). The wavefront RMS is greater where the imaging beam has passed through more tissue. Scale bar is 200 µm.

Wavefront variation can also be caused by differences in tissue type. For example, dense tissues may aberrate the imaging beam more strongly than transparent tissues. This is demonstrated in Figure 5.12, where adipose and muscle tissues are adjacent within the same imaging volume. Here the wavefront RMS is shown without defocus, as defocus is similar across the field-of-view due to the flat surface. Although the sample surface is flat, the wavefront RMS varies across the field-of-view because the highly scattering muscle tissue distorts the imaging beam more than the weakly scattering adipose tissue. This is seen in Figure 5.12(c).
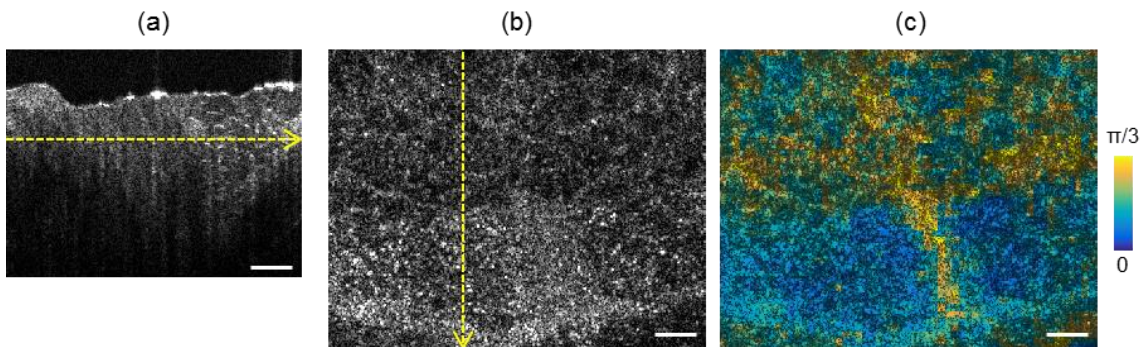
Figure 5.12. Wavefront measurement and correction in *ex vivo* chicken breast. (a) OCT cross-section showing the muscle and adipose tissue types. (b) Composite depth image of locally corrected subimages, taken at the depth plane indicated by the yellow line in (a). (c) Map of the local wavefront RMS across the depth image (b), excluding defocus. The wavefront RMS is greater in the muscle tissue when compared to the adipose tissue. Scale bar is 200 µm.

The choice of image sharpness metric is important when considering the optimization of various image types [79]. For example, the point-scatterer images used in both simulation and experiment in the previous sections have very different optimization characteristics than the dense tissue images presented here. A variety of image sharpness metrics have been proposed, where the intensity is raised to a particular power gamma,

$$\sum_{x,y} I^{\gamma}(x,y). \tag{5.29}$$

While each metric is maximized in the absence of aberrations, the performance of the metrics can vary quite dramatically depending on the characteristics of the image. Images which are expected to have bright point-like features are more easily optimized by image sharpness metrics with large powers, such as $\gamma > 2$. This emphasizes improvement in contrast at high intensities, and performs well for the point-like images of the photoreceptors and scattering phantom. However, images with dark features within a scattering background are better optimized by sharpness metrics with small powers, such as $\gamma < 1$. The negative entropy metric

$$\sum_{x,y} I(x,y)\ln(x,y) \tag{5.30}$$

behaves similarly to the power metric with $\gamma = 1.1$.

Several metrics were tested as the optimization metric for the forward model method on the dataset presented in Figure 5.11. Improvement in the intensity squared metric of the composite image was used as a common standard. The optimization procedure was allowed 10N function evaluations, where N is the number of Zernike weights being optimized (N = 12 including 2nd, 3rd, and 4th order aberrations). Table 5.2 shows the improvement in sharpness and the percent of subimages which converged in the allotted number of function evaluations. The negative entropy metric showed the best performance across all metrics, and was therefore used for each tissue dataset.

TABLE 5.2

IMAGE SHARPNESS IMPROVEMENT AND CONVERGENCE FOR SELECT METRICS

	$\gamma = 4$	$\gamma = 2$	$\gamma = 0.5$	I ln(I)
Sharpness improvement	40%	40%	41%	44%
Convergence	75%	78%	71%	90%

An additional consideration is the impact of speckle in highly scattering and homogenous tissues. With a coherent measurement, the image is corrupted by multiplicative speckle noise [128]. The intensity of the speckle noise can be modeled as a negative-exponential random variable. In a homogeneous tissue region, the sharpness of the underlying image structure will be approximately constant with respect to changing wavefront. Therefore, the image sharpness metric is dominated by the characteristics of the speckle noise. For fully developed speckle, the speckle contrast (and therefore image sharpness) are theoretically independent of phase aberrations [130,131]. This leads to a dramatic variation in the wavefront RMS as the optimization procedure unsuccessfully attempts to sharpen the speckle.
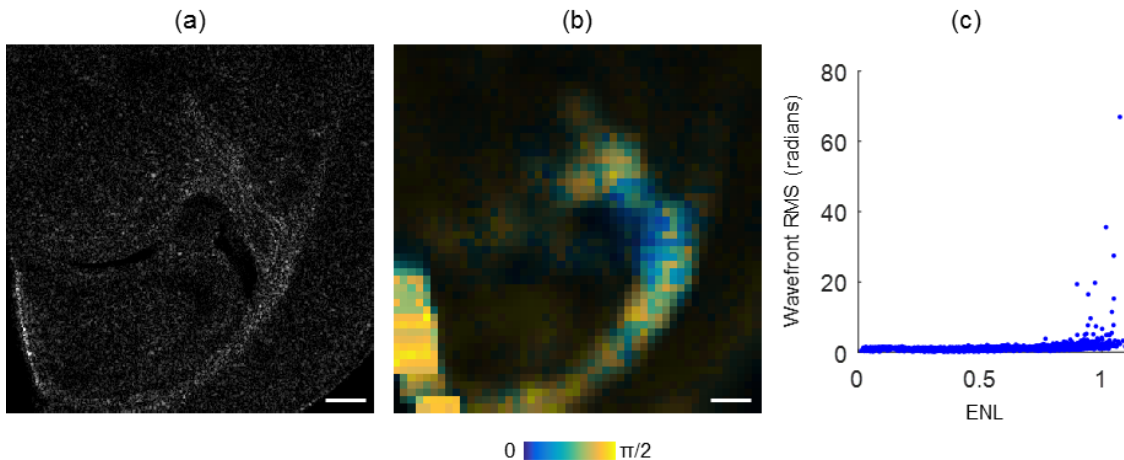
Figure 5.13. Wavefront map for *ex vivo* mouse brain slice. (a) Composite depth image of locally corrected subimages. (b) Corresponding wavefront RMS, with brightness mapped to estimated image sharpness. (c) Equivalent number of looks (ENL), vs. computational wavefront RMS. Scale bars 200 µm.

To determine a level of trust for each subimage, the aberration-free image sharpness can be estimated from the autocorrelation of the subimage [79]. Here the variance of the autocorrelation is used, excluding the DC term and normalized by the total subimage intensity. The sharpness estimate can then be used to mask out areas without significant image features from the wavefront map. This was not necessary for chicken breast data, which had sufficient image structure throughout the dataset. However, the brain slice images contained large areas with low intrinsic sharpness. Such areas can be masked as shown in Figure 5.13. In Figure 5.13(b) the estimated image sharpness is mapped to brightness, and the wavefront RMS to color.

Alternatively, the speckle content can be estimated using the equivalent number of looks (ENL) defined as

$$\text{ENL} = \frac{\mu^2}{\sigma^2}, \tag{5.31}$$

where μ is the mean and σ is the standard deviation of the image intensity [132]. The relation between the ENL and wavefront RMS for each subimage is shown in Figure 5.13(c). Subimages with higher ENL, and therefore greater speckle content, are associated with artificially high wavefront RMS. As such, the computational wavefront measurement for areas with low underlying sharpness or high speckle content should be treated with a healthy skepticism.

6   SUMMARY AND OUTLOOK

6.1   Summary

The work presented in Chapters 3 through 5 expanded both the theory and application of computational OCT. Optical models were developed to identify new image processing and reconstruction methods. Experimental systems were then designed, constructed, and tested to demonstrate the validity and useful application of each method.

With these new computational imaging methods, high-resolution polarization-contrast was demonstrated in bulk biological tissue. Wavefront measurement was also demonstrated in bulk tissue, providing a new form of image contrast through spatial aberration mapping. The primary weakness of computational OCT, low signal strength, was addressed via integration with hardware wavefront correction, which achieved image quality beyond that of hardware or computational methods alone. Each result is simultaneously a significant step forward for optical science, and a starting point for new research.

6.2   Continuing work

6.2.1   Intraoperative PS-ISAM imaging

The imaging system constructed for the demonstration of PS-ISAM (see Section 3.3) has been transferred to a portable cart, shown in Figure 6.1 for imaging of freshly resected breast tissue samples. It is presently being used to image tissue in the operating room and pathology lab at Carle Foundation Hospital in Urbana, IL. This will allow direct correlation between diagnosed histology and PS-ISAM images of various disease types. The numerical aperture of the system has also been increased from 0.1 NA to 0.2 NA. Because of the PS-ISAM reconstruction algorithm, the increase

in numerical aperture will provide higher resolution without loss of depth-of-field. This is expected to improve the ability of PS-ISAM to resolve important biological features, such as ducts, lobules, vessels, and tumors in breast tissue specimens.
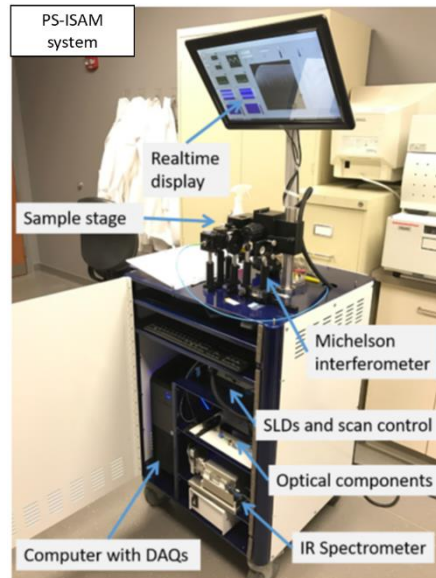
Figure 6.1. Intraoperative PS-OCT imaging cart. Designed and constructed by Darold Spillman and Kelly Mesa of the Biphotonics Imaging Laboratory.

6.2.2 Polarization-sensitive CAO

A natural next step is to extend the CAO method to polarization-sensitive imaging. In this thesis, aberrations were assumed to be polarization-independent. However, it is possible that the system optics or sample will introduce polarization-aberrations which may or may not be dependent upon the input polarization state [133]. Polarization-aberrations may arise from intrinsic birefringence of the imaging optics, stress birefringence of optical mounts, or from thin film coatings on the optics, and have the greatest impact at high NA due to large angle of incidence with the imaging optics or sample [134]. The optical system can be described via a polarization-aberration matrix, or Jones pupil, which describes the change in polarization state between each point in the input

and output object or pupil space. Alternatively, the polarized beam can be propagated in arbitrary optical systems using a matrix method [135].

A common OCT component is the beam splitter, which has a thin-film structure illuminated at a 45° angle that can lead to significant polarization-aberration [136]. Therefore, it is likely that each channel in the PS-OCT system would have a unique CAO optimization even in the case of a non-birefringent sample. As a biological example, the RNFL in the retina is known to be birefringent. Assuming the retina is perpendicular to the direction of beam propagation, the angle of incidence on the retina is limited by the pupil of the eye to approximately 11°, or 0.2 NA. Therefore, it is not anticipated that polarization-aberrations due to Fresnel or thin-film effects will play a significant role in this case. If the tissue is modeled as a waveplate, there may be polarization-dependent spherical aberration due to polarization-dependent optical path length.

Polarization-aberrations are generally an order of magnitude less than the scalar wavefront aberrations. Therefore, detailed calculations should be performed to determine the expected impact of polarization-aberrations for a given imaging scenario before pursuing CAO for polarization-aberration correction.

6.2.3   Computational OCT of diseased eyes

The computational OCT images of the retina presented in this thesis were acquired in healthy eyes. However, the combination of HAO and CAO is most promising for imaging in diseased eyes. Many eye pathologies are associated with age, making imaging of aged retinas a clinical priority. However, elderly subjects often have cataracts, which make it difficult to deliver and receive light from the retina, and ocular aberrations increase with age as well. Using HAO, the deformable mirror could focus the light through the scattering cataracts to obtain a high SNR image.

However, if the retina is diseased and has disorganized structures, such as diabetic macular edema or drusen, the Shack-Hartmann wavefront sensor will perform poorly. This is because the Shack-Hartmann assumes a point-like scatterer, which is approximated in the healthy eye by the bright reflections from the photoreceptors. CAO could be used to overcome the reduced performance of the wavefront sensor. In this way, hardware and computational correction could work in tandem to image the eye in elderly subjects, and/or in diseased eyes.

An example image taken from a diseased eye is shown in Figure 6.2. The dark area corresponds to the drusen caused by macular degeneration, where photoreceptors have been degraded and displaced. The cone photoreceptors are misshapen, indicating that the point spread function could be improved by CAO. However, there was significant subject motion making computational correction impossible. This seems to be a common issue when imaging elderly or diseased subjects, who are either unstable or have difficulty focusing on the fixation target.
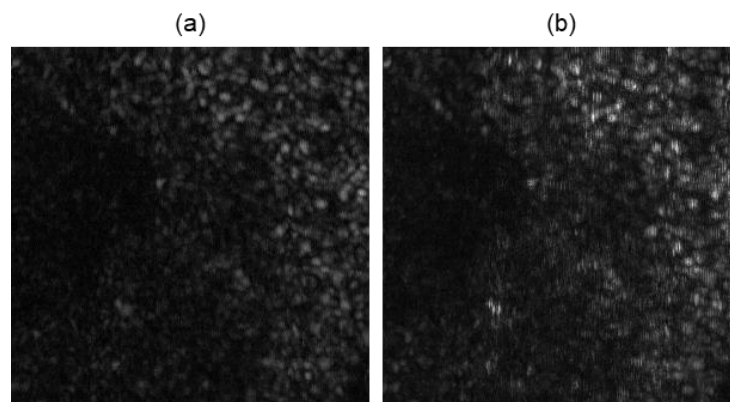
Figure 6.2. Retinal OCT image of drusen using (a) HAO and (b) HAO+CAO. Bright reflections correspond to photoreceptors, and the dark area corresponds to the drusen. Due to phase instability, motion artifacts appear in the HAO+CAO image as dark vertical lines.

An obvious solution is to simply image faster. However, the current frame rate is limited by the scan speed of the galvanometer mirror. Instead, a resonant scanner could be used to image at a higher frame rate. For example, a 4 kHz resonant scanner could increase the frame rate by nearly

30%. The drawback is that the fixed speed of the resonant scanner limits the flexibility of the imaging system, which is used for many other experiments. Alternatively, a high-speed full-field approach can be used, assuming that HAO is integrated into the system to overcome the very low SNR typical of that method [104].

6.2.4 Aberration contrast imaging

Using the methods developed in Chapter 5, it is possible to map the optical aberrations within a tissue sample. Just as PS-OCT provides enhanced contrast between certain tissues, the wavefront map may also serve as a useful source of contrast for diseased tissue. For this to be possible, CAO must demonstrate consistent performance across a wide range of image types, including sparse and dense features, and positive and negative intensity contrast.

When performing CAO on a variety of image types, it is difficult to determine the optimal aberration correction. In an ideal case, one could imagine comparing the corrected image to a gold standard to maximize a measure of similarity between the image and the gold standard. However, in many applications a one-to-one comparison to histology is impossible. For example, it is quite unreasonable to acquire histology from the living human retina for image comparison. There is also the added concern that the source of contrast is not the same between the histology and imaging method. This can sometimes be an advantage when identifying disease, but can make comparison with histology difficult. Representative histology or measures such as photoreceptor density also cannot be used as a gold standard, since there is large variation in photoreceptor density and size across the general population [137], and disease processes disrupt the typical tissue structure.

Alternatively, image metrics can be used to determine the optimal aberration correction. These metrics are known to be optimized in the case of no aberration. Multiple image sharpness metrics were explored in Section 5.6.2, showing that performance of the CAO optimization depends upon the chosen sharpness metric relative to the image features. For example, the standard intensity squared metric was outperformed by the negative entropy metric in the brain tissue image. A poor choice of sharpness metric leads to slow convergence and causes the algorithm to stop at local maxima. This has led researchers to develop designer metrics for various image types [79]. The use of a customized sharpness metric would reduce the convergence time, helping achieve real-time CAO. The metric would also be well behaved and more likely to find the global optimum.

Choosing the appropriate metric is a time-consuming process, as many metrics must be manually tested for each tissue structure. Machine learning could be used to classify the image type to automatically choose the best image metric. For example, images and their best performing metric (determined manually) could be used to generate classes of image types appropriate for each image metric. New OCT images would then be corrected using the appropriate image sharpness metric based upon their classification. In this case, both the choice of image metric and optimization of the metric would be performed in an automated manner.

Instead of choosing between several predetermined sharpness metrics, it is possible that machine learning could be used to create new sharpness metrics. Aberrated and corrected OCT images from a variety of known tissue types could be used as training data to find an optimal sharpness metric for each tissue type. Convergence speed and RMS variation from the known wavefront error could be used as performance measures when searching for a sharpness metric.

Aberration mapping can also be used to answer fundamental questions in optics. It is known that imaging with a higher numerical aperture reduces the useable imaging depth within tissue. Computational wavefront measurement could be used to visualize how the aberrations increase with NA, and to verify that it is in fact aberrations which limit the useful signal. Other limiting factors, such as multiple scattering, could be measured simultaneously using PS-OCT [138]. Perhaps an optimal NA could be determined which balances the impact of aberration and multiple scattering.

6.3 New computational imaging methods

The work in this thesis demonstrates the capability of computational imaging to increase the performance of OCT and expand it to new application areas. This was done by understanding the information content of the OCT signal via the physical model, and then creating new processing and reconstruction schemes to retrieve the desired information. Other optical imaging modalities may likewise be improved through a computational imaging approach.

Alternatively, the computational imaging framework can be used to create entirely new imaging methods. Through an understanding of the underlying physics, an experiment can be designed such that the desired information is encoded in the acquired signal. In this case, directly mapping the signal to an image may not show any useful information. However, computational methods can be used to extract the desired information for sensing or imaging.

An example workflow is suggested here. First, the application-critical information is identified through careful consideration of the imaging application. The imaging sample, either biological or material, interacts with and modifies the optical signal in some way. Intuitive sources of contrast in optics include scattering, absorption, polarization, and phase. The time scale over which this

contrast takes place must also be considered. Second, the application-critical information can be mapped to various dimensions as needed. Each of the sources of contrast mentioned above can be used for this. For example, information can be mapped to orthogonal polarizations, distinct wavelengths, timepoints, or physical locations. Lastly, the inverse problem can be solved to retrieve the desired information. This process results in custom imaging methods tailored to specific applications, which are likely to provide improved performance over more general methods.

As the applications of optical imaging become both more diverse and specialized, the limitations of traditional methods become more apparent. It is anticipated that computational imaging will continue to provide key technological breakthroughs that enable new discoveries in biology and medicine.

REFERENCES

1. D. Evanko, A. Heinrichs, and C. K. Rosenthal, "Nature milestones in light microscopy," Nat. Cell Biol. **11**, S6–S22 (2009).
2. D. Huang, E. A. Swanson, C. P. Lin, J. S. Schuman, W. G. Stinson, W. Chang, M. R. Hee, T. Flotte, K. Gregory, C. A. Puliafito, and J. G. Fujimoto, "Optical coherence tomography," Science **254**, 1178–1181 (1991).
3. J. Fujimoto and E. Swanson, "The development, commercialization, and impact of optical coherence tomography," Investig. Opthalmology Vis. Sci. **57**, OCT1-OCT13 (2016).
4. "Advancing clinical imaging beyond the existing standard of care: Evaluating new optical imaging modalities," https://portal.luxresearchinc.com/research/report_excerpt/18129.
5. "Optical coherence tomography for healthcare and life science: Technology and market trends," http://tematys.fr/Publications/en.
6. E. Swanson, "Estimates of ophthalmic OCT market size and the dramatic reduction in reimbursement payments," http://www.octnews.org/articles/4176266/estimates-of-ophthalmic-oct-market-size-and-the-dr/.
7. J. A. Evans, J. M. Poneros, B. E. Bouma, J. Bressner, E. F. Halpern, M. Shishkov, G. Y. Lauwers, M. Mino-Kenudson, N. S. Nishioka, and G. J. Tearney, "Optical coherence tomography to identify intramucosal carcinoma and high-grade dysplasia in Barrett's esophagus," Clin. Gastroenterol. Hepatol. **4**, 38–43 (2006).
8. I.-K. Jang, G. J. Tearney, B. MacNeill, M. Takano, F. Moselewski, N. Iftima, M. Shishkov, S. Houser, H. T. Aretz, E. F. Halpern, and B. E. Bouma, "*In vivo* characterization of coronary atherosclerotic plaque by use of optical coherence tomography," Circulation **111**, 1551–1555 (2005).
9. F. T. Nguyen, A. M. Zysk, E. J. Chaney, J. G. Kotynek, U. J. Oliphant, F. J. Bellafiore, K. M. Rowland, P. A. Johnson, and S. A. Boppart, "Intraoperative evaluation of breast tumor margins with optical coherence tomography," Cancer Res. **69**, 8790–8796 (2009).
10. D. Stifter, "Beyond biomedicine: A review of alternative applications and developments for optical coherence tomography," Appl. Phys. B **88**, 337–357 (2007).
11. "IEEE Transactions on Computational Imaging information for authors," IEEE Trans. Comput. Imaging **1**, 72–73 (2015).
12. A. M. Cormack, "Representation of a function by its line integrals, with some radiological applications. II," J. Appl. Phys. **35**, 2908–2913 (1964).
13. G. N. Hounsfield, "Computerized transverse axial scanning (tomography): I. Description of system," Br. J. Radiol. **46**, 1016–1022 (1973).
14. P. C. Lauterbur, "Image formation by induced local interactions: examples employing nuclear magnetic resonance," Nature **242**, 190–191 (1973).
15. C. W. Sherwin, J. P. Ruina, and R. D. Rawcliffe, "Some early developments in synthetic aperture radar systems," IRE Trans. Mil. Electron. **MIL-6**, 111–115 (1962).
16. S. W. Lasswell, "History of SAR at Lockheed Martin (previously Goodyear Aerospace)," Proc. SPIE **5788**, 1–12 (2005).
17. A. Ahmad, N. D. Shemonski, S. G. Adie, H. Kim, W. W. Hwu, P. S. Carney, and S. A. Boppart, "Real-time *in vivo* computed optical interferometric tomography," Nat. Photonics **7**, 444–448 (2013).

18.   N. D. Shemonski, F. A. South, Y.-Z. Liu, S. G. Adie, P. Scott Carney, and S. A. Boppart, "Computational high-resolution optical imaging of the living human retina," Nat. Photonics **9**, 440–443 (2015).

19.   K.-S. Lee, H. Zhao, S. F. Ibrahim, N. Meemon, L. Khoudeir, and J. P. Rolland, "Three-dimensional imaging of normal skin and nonmelanoma skin cancer with cellular resolution using Gabor domain optical coherence microscopy," J. Biomed. Opt. **17**, 126006 (2012).

20.   B. A. Standish, K. K. C. Lee, A. Mariampillai, N. R. Munce, M. K. K. Leung, V. X. D. Yang, and I. A. Vitkin, "In vivo endoscopic multi-beam optical coherence tomography," Phys. Med. Biol. **55**, 615–622 (2010).

21.   Z. Ding, H. Ren, Y. Zhao, J. S. Nelson, and Z. Chen, "High-resolution optical coherence tomography over a large depth range with an axicon lens," Opt. Lett. **27**, 243–245 (2002).

22.   C. Blatter, J. Weingast, A. Alex, B. Grajciar, W. Wieser, W. Drexler, R. Huber, and R. A. Leitgeb, "In situ structural and microangiographic assessment of human skin lesions with high-speed OCT," Biomed. Opt. Express **3**, 2636 (2012).

23.   J. M. Beckers, "Adaptive optics for astronomy: Principles, performance, and applications," Annu. Rev. Astron. Astrophys. **31**, 13–62 (1993).

24.   R. Davies and M. Kasper, "Adaptive optics for astronomy," Annu. Rev. Astron. Astrophys. **50**, 305–351 (2012).

25.   D. T. Miller, D. R. Williams, G. M. M. Morris, and J. Liang, "Images of cone photoreceptors in the living human eye," Vision Res. **36**, 1067–1079 (1996).

26.   Y. Zhang, B. Cense, J. Rha, R. S. Jonnal, W. Gao, R. J. Zawadzki, J. S. Werner, S. Jones, S. Olivier, and D. T. Miller, "High-speed volumetric imaging of cone photoreceptors with adaptive optics spectral-domain optical coherence tomography," Opt. Express **14**, 4380–4394 (2006).

27.   M. J. Booth, "Adaptive optical microscopy: the ongoing quest for a perfect image," Light Sci. Appl. **3**, e165 (2014).

28.   Y. Yasuno, J.-I. Sugisaka, Y. Sando, Y. Nakamura, S. Makita, M. Itoh, and T. Yatagai, "Non-iterative numerical method for laterally superresolving Fourier domain optical coherence tomography," Opt. Express **14**, 1006–1020 (2006).

29.   L. Yu, B. Rao, J. Zhang, J. Su, Q. Wang, and S. Guo, "Improved lateral resolution in optical coherence tomography by digital focusing using two-dimensional numerical diffraction method," Opt. Express **15**, 7634–7641 (2007).

30.   A. Kumar, W. Drexler, and R. A. Leitgeb, "Numerical focusing methods for full field OCT: A comparison based on a common signal model," Opt. Express **22**, 16061 (2014).

31.   J. Mo, M. de Groot, and J. de Boer, "Focus-extension by depth-encoded synthetic aperture in optical coherence tomography," Opt. Express **21**, 123–128 (2013).

32.   J. Mo, M. de Groot, and J. F. de Boer, "Depth-encoded synthetic aperture optical coherence tomography of biological tissues with extended focal depth," Opt. Express **23**, 4935–4945 (2015).

33.   D. Hillmann, C. Lührs, T. Bonin, P. Koch, and G. Hüttmann, "Holoscopy—holographic optical coherence tomography," Opt. Lett. **36**, 2390–2392 (2011).

34.   D. Hillmann, G. Franke, C. Lührs, P. Koch, and G. Hüttmann, "Efficient holoscopy image reconstruction," Opt. Express **20**, 21247 (2012).

35.   T. S. Ralston, D. L. Marks, P. Scott Carney, and S. A. Boppart, "Interferometric synthetic aperture microscopy," Nat. Phys. **3**, 129–134 (2007).

36. T. Colomb, F. Montfort, J. Kühn, N. Aspert, E. Cuche, A. Marian, F. Charrière, S. Bourquin, P. Marquet, and C. Depeursinge, "Numerical parametric lens for shifting, magnification, and complete aberration compensation in digital holographic microscopy," J. Opt. Soc. Am. A **23**, 3177 (2006).

37. L. Miccio, D. Alfieri, S. Grilli, P. Ferraro, A. Finizio, L. De Petrocellis, and S. D. Nicola, "Direct full compensation of the aberrations in quantitative phase microscopy of thin objects by a single digital hologram," Appl. Phys. Lett. **90**, 41104 (2007).

38. S. G. Adie, B. W. Graf, A. Ahmad, P. S. Carney, and S. A. Boppart, "Computational adaptive optics for broadband optical interferometric tomography of biological tissue," Proc. Natl. Acad. Sci. **109**, 7175–7180 (2012).

39. A. Kumar, W. Drexler, and R. A. Leitgeb, "Subaperture correlation based digital adaptive optics for full field optical coherence tomography," Opt. Express **21**, 10850 (2013).

40. T. S. Ralston, D. L. Marks, P. S. Carney, and S. A. Boppart, "Inverse scattering for optical coherence tomography," J. Opt. Soc. Am. A **23**, 1027 (2006).

41. T. S. Ralston, D. L. Marks, S. A. Boppart, and P. S. Carney, "Inverse scattering for high-resolution interferometric microscopy," Opt. Lett. **31**, 3585 (2006).

42. B. J. Davis, S. C. Schlachter, D. L. Marks, T. S. Ralston, S. A. Boppart, and P. S. Carney, "Nonparaxial vector-field modeling of optical coherence tomography and interferometric synthetic aperture microscopy," J. Opt. Soc. Am. A **24**, 2527–2542 (2007).

43. D. L. Marks, T. S. Ralston, S. A. Boppart, and P. S. Carney, "Inverse scattering for frequency-scanned full-field optical coherence tomography," J. Opt. Soc. Am. A **24**, 1034–1041 (2007).

44. T. S. Ralston, D. L. Marks, P. S. Carney, S. A. Boppart, S. G. Adie, B. J. Davis, T. S. Ralston, D. L. Marks, P. S. Carney, and S. A. Boppart, "Real-time interferometric synthetic aperture microscopy," Opt. Express **16**, 2555–2569 (2008).

45. S. G. Adie, N. D. Shemonski, B. W. Graf, A. Ahmad, P. Scott Carney, and S. A. Boppart, "Guide-star-based computational adaptive optics for broadband interferometric tomography," Appl. Phys. Lett. **101**, 221117 (2012).

46. A. Kumar, T. Kamali, R. Platzer, A. Unterhuber, W. Drexler, and R. A. Leitgeb, "Anisotropic aberration correction using region of interest based digital adaptive optics in Fourier domain OCT," Biomed. Opt. Express **6**, 1124 (2015).

47. M. R. Hee, D. Huang, E. A. Swanson, and J. G. Fujimoto, "Polarization-sensitive low-coherence reflectometer for birefringence characterization and ranging," J. Opt. Soc. Am. B **9**, 903–908 (1992).

48. J. F. de Boer, T. E. Milner, M. J. C. van Gemert, and J. S. Nelson, "Two-dimensional birefringence imaging in biological tissue by polarization-sensitive optical coherence tomography," Opt. Lett. **22**, 934–936 (1997).

49. J. F. de Boer, C. K. Hitzenberger, and Y. Yasuno, "Polarization sensitive optical coherence tomography – A review [Invited]," Biomed. Opt. Express **8**, 1838–1873 (2017).

50. F. A. South, E. J. Chaney, M. Marjanovic, S. G. Adie, and S. A. Boppart, "Differentiation of *ex vivo* human breast tissue using polarization-sensitive optical coherence tomography," Biomed. Opt. Express **5**, 3417–3426 (2014).

51. J. Liang, D. R. Williams, and D. T. Miller, "Supernormal vision and high-resolution retinal imaging through adaptive optics," J. Opt. Soc. Am. A **14**, 2884–2892 (1997).

52. S. A. Rahman and M. J. Booth, "Direct wavefront sensing in adaptive optical microscopy using backscattered light," Appl. Opt. **52**, 5523–5532 (2013).

53. P. H. Tomlins and R. K. Wang, "Theory, developments and applications of optical coherence tomography," J. Phys. D. Appl. Phys. **38**, 2519–2535 (2005).

54. W. Drexler and J. G. Fujimoto, eds., *Optical Coherence Tomography: Technology and Applications*, 2nd ed. (Springer, 2015).

55. J. M. Schmitt, A. Knuttel, M. Yadlowsky, and M. A. Eckhaus, "Optical-coherence tomography of a dense tissue: Statistics of attenuation and backscattering," Phys. Med. Biol. **39**, 1705–1720 (1994).

56. A. Unterhuber, B. Považay, B. Hermann, H. Sattmann, A. Chavez-Pirson, and W. Drexler, "*In vivo* retinal optical coherence tomography at 1040 nm-enhanced penetration into the choroid," Opt. Express **13**, 3252–3258 (2005).

57. I. Grulkowski, J. J. Liu, B. Potsaid, V. Jayaraman, C. D. Lu, J. Jiang, A. E. Cable, J. S. Duker, and J. G. Fujimoto, "Retinal, anterior segment and full eye imaging using ultrahigh speed swept source OCT with vertical-cavity surface emitting lasers," Biomed. Opt. Express **3**, 2733–2751 (2012).

58. J. F. de Boer and T. E. Milner, "Review of polarization sensitive optical coherence tomography and Stokes vector determination," J. Biomed. Opt. **7**, 359 (2002).

59. R. C. Jones, "A new calculus for the treatment of optical systems I. Description and discussion of the calculus," J. Opt. Soc. Am. **31**, 488–493 (1941).

60. J. J. Pasquesi, S. C. Schlachter, M. D. Boppart, E. Chaney, S. J. Kaufman, and S. A. Boppart, "*In vivo* detection of exercised-induced ultrastructural changes in genetically-altered murine skeletal muscle using polarization-sensitive optical coherence tomography," Opt. Express **14**, 1547–1556 (2006).

61. J. Strasswimmer, M. C. Pierce, B. H. Park, V. Neel, and J. F. de Boer, "Polarization-sensitive optical coherence tomography of invasive basal cell carcinoma," J. Biomed. Opt. **9**, 292–298 (2004).

62. E. Götzinger, M. Pircher, and C. K. Hitzenberger, "High speed spectral domain polarization sensitive optical coherence tomography of the human retina," Opt. Express **13**, 10217–10229 (2005).

63. S. K. Nadkarni, M. C. Pierce, B. H. Park, J. F. de Boer, P. Whittaker, B. E. Bouma, J. E. Bressner, E. Halpern, S. L. Houser, and G. J. Tearney, "Measurement of collagen and smooth muscle cell content in atherosclerotic plaques using polarization-sensitive optical coherence tomography," J. Am. Coll. Cardiol. **49**, 1474–1481 (2007).

64. R. Patel, A. Khan, R. Quinlan, and A. N. Yaroslavsky, "Polarization-sensitive multimodal imaging for detecting breast cancer," Cancer Res. **74**, 4685–93 (2014).

65. D. Stifter, E. Leiss-Holzinger, Z. Major, B. Baumann, M. Pircher, E. Götzinger, C. K. Hitzenberger, and B. Heise, "Dynamic optical studies in materials testing with spectral-domain polarization-sensitive optical coherence tomography," Opt. Express **18**, 25712–25 (2010).

66. R. S. Jonnal, O. P. Kocaoglu, R. J. Zawadzki, Z. Liu, D. T. Miller, and J. S. Werner, "A review of adaptive optics optical coherence tomography: Technical advances, scientific applications, and the future," Invest. Ophthalmol. Vis. Sci. **57**, OCT51-OCT68 (2016).

67. Y. Jian, J. Xu, M. A. Gradowski, S. Bonora, R. J. Zawadzki, and M. V. Sarunic, "Wavefront sensorless adaptive optics optical coherence tomography for *in vivo* retinal imaging in mice," Biomed. Opt. Express **5**, 547 (2014).

68. V. Lakshminarayanan and A. Fleck, "Zernike polynomials: A guide," J. Mod. Opt. **58**, 1678 (2011).

69. "Zernike polynomials2," https://commons.wikimedia.org/wiki/File:Zernike_polynomials2 .png.

70. S. J. Chiu, X. T. Li, P. Nicholas, C. A. Toth, J. A. Izatt, and S. Farsiu, "Automatic segmentation of seven retinal layers in SDOCT images congruent with expert manual segmentation," Opt. Express **18**, 19413–19428 (2010).

71. D. L. Marks, A. L. Oldenburg, J. J. Reynolds, and S. A. Boppart, "Digital algorithm for dispersion correction in optical coherence tomography for homogreneous and stratified media," Appl. Opt. **42**, 204–217 (2003).

72. M. Wojtkowski, V. J. Srinivasan, T. H. Ko, J. G. Fujimoto, A. Kowalczyk, and J. S. Duker, "Ultrahigh-resolution, high-speed, Fourier domain optical coherence tomography and methods for dispersion compensation," Opt. Express **12**, 2404 (2004).

73. E. C. W. Lee, J. F. de Boer, M. Mujat, H. Lim, and S. H. Yun, "*In vivo* optical frequency domain imaging of human retina and choroid," Opt. Express **14**, 4403–4411 (2006).

74. B. J. Davis, D. L. Marks, T. S. Ralston, P. S. Carney, and S. A. Boppart, "Interferometric synthetic aperture microscopy: Computed imaging for scanned coherent microscopy," Sensors **8**, 3903–3931 (2008).

75. M. Born and E. Wolf, *Principles of Optics*, 7th ed. (Cambridge University Press, 1999).

76. Y.-Z. Liu, N. D. Shemonski, S. G. Adie, A. Ahmad, A. J. Bower, P. S. Carney, and S. A. Boppart, "Computed optical interferometric tomography for high-speed volumetric cellular imaging.," Biomed. Opt. Express **5**, 2988–3000 (2014).

77. T. S. Ralston, S. G. Adie, D. L. Marks, S. A. Boppart, and P. S. Carney, "Cross-validation of interferometric synthetic aperture microscopy and optical coherence tomography," Opt. Lett. **35**, 1683–1685 (2010).

78. H. Hofer, N. Sredar, H. Queener, C. Li, and J. Porter, "Wavefront sensorless adaptive optics ophthalmoscopy in the human eye," Opt. Express **19**, 14160 (2011).

79. J. R. Fienup and J. J. Miller, "Aberration correction by maximizing generalized sharpness metrics," J. Opt. Soc. Am. A. Opt. Image Sci. Vis. **20**, 609–620 (2003).

80. N. D. Shemonski, S. G. Adie, Y.-Z. Liu, F. A. South, P. S. Carney, and S. A. Boppart, "Stability in computed optical interferometric tomography (Part I): Stability requirements," Opt. Express **22**, 19183–19197 (2014).

81. N. D. Shemonski, A. Ahmad, S. G. Adie, Y.-Z. Liu, F. A. South, P. S. Carney, and S. A. Boppart, "Stability in computed optical interferometric tomography (Part II): *in vivo* stability assessment," Opt. Express **22**, 19314–19326 (2014).

82. N. D. Shemonski, S. S. Ahn, Y.-Z. Liu, F. A. South, P. S. Carney, and S. A. Boppart, "Three-dimensional motion correction using speckle and phase for *in vivo* computed optical interferometric tomography," Biomed. Opt. Express **5**, 4131–4143 (2014).

83. J. L. Duncan, Y. Zhang, J. Gandhi, C. Nakanishi, M. Othman, K. E. H. Branham, A. Swaroop, and A. Roorda, "High-resolution imaging with adaptive optics in patients with inherited retinal degeneration," Investig. Opthalmology Vis. Sci. **48**, 3283 (2007).

84. S. Zayit-Soudry, J. L. Duncan, R. Syed, M. Menghini, and A. J. Roorda, "Cone structure imaged with adaptive optics scanning laser ophthalmoscopy in eyes with nonneovascular age-related macular degeneration," Investig. Opthalmology Vis. Sci. **54**, 7498 (2013).

85. M. Pircher, B. Baumann, E. Götzinger, and C. K. Hitzenberger, "Retinal cone mosaic imaged with transverse scanning optical coherence tomography," Opt. Lett. **31**, 1821–1823 (2006).

86. L. N. Thibos, X. Hong, A. Bradley, and X. Cheng, "Statistical variation of aberration structure and image quality in a normal population of healthy eyes," J. Opt. Soc. Am. A. Opt. Image Sci. Vis. **19**, 2329–2348 (2002).

87. J. Liang and D. R. Williams, "Aberrations and retinal image quality of the normal human eye," J. Opt. Soc. Am. A **14**, 2873 (1997).

88. D. R. Williams, "Imaging single cells in the living retina," Vision Res. **51**, 1379–1396 (2011).

89. S. Martinez-Conde, S. L. Macknik, and D. H. Hubel, "The role of fixational eye movements in visual perception," Nat. Rev. Neurosci. **5**, 229–240 (2004).

90. L. Ginner, A. Kumar, D. Fechtig, L. M. Wurster, M. Salas, M. Pircher, and R. A. Leitgeb, "Noniterative digital aberration correction for cellular resolution retinal optical coherence tomography *in vivo*," Optica **4**, 924–931 (2017).

91. O. P. Kocaoglu, B. Cense, R. S. Jonnal, Q. Wang, S. Lee, W. Gao, and D. T. Miller, "Imaging retinal nerve fiber bundles using optical coherence tomography with adaptive optics," Vis. Res. **51**, 1835–1844 (2011).

92. K. Takayama, S. Ooto, M. Hangai, N. Ueda-Arakawa, S. Yoshida, T. Akagi, H. O. Ikeda, A. Nonaka, M. Hanebuchi, T. Inoue, and N. Yoshimura, "High-resolution imaging of retinal nerve fiber bundles in glaucoma using adaptive optics scanning laser ophthalmoscopy," Am. J. Ophthalmol. **155**, 870–881 (2013).

93. J. Fisher, D. Jacobs, C. Markowitz, S. Galetta, N. Volpe, M. Nanoschiavi, M. Baier, E. Frohman, H. Winslow, and T. Frohman, "Relation of visual function to retinal nerve fiber layer thickness in multiple sclerosis," Ophthalmology **113**, 324–332 (2006).

94. S. Saidha, S. B. Syc, M. A. Ibrahim, C. Eckstein, C. V. Warner, S. K. Farrell, J. D. Oakley, M. K. Durbin, S. A. Meyer, L. J. Balcer, E. M. Frohman, J. M. Rosenzweig, S. D. Newsome, J. N. Ratchford, Q. D. Nguyen, and P. A. Calabresi, "Primary retinal pathology in multiple sclerosis as detected by optical coherence tomography," Brain **134**, 518–533 (2011).

95. F. A. South, Y.-Z. Liu, P. S. Carney, and S. A. Boppart, "Computed optical interferometric imaging: Methods, achievements, and challenges," IEEE J. Sel. Top. Quantum Electron. **22**, 186–196 (2016).

96. B. Richards and E. Wolf, "Electromagnetic diffraction in optical systems II. Structure of the image field in an aplanatic system," Proc. R. Soc. A **253**, 358–379 (1959).

97. B. J. Davis and P. S. Carney, "Robust determination of the anisotropic polarizability of nanoparticles using coherent confocal microscopy," J. Opt. Soc. Am. A **25**, 2102–2113 (2008).

98. M. K. Al-Qaisi and T. Akkin, "Optical coherence tomography based on polarization-maintaining fiber," Opt. Express **18**, 2377–2386 (2010).

99. A. Doronin, C. Macdonald, and I. Meglinski, "Propagation of coherent polarized light in turbid highly scattering medium," J. Biomed. Opt. **19**, 25005 (2014).

100. J. A. Kubby, ed., *Adaptive Optics for Biological Imaging* (Taylor & Francis, 2013).

101. S. Gabarda and G. Cristóbal, "Blind image quality assessment through anisotropy," J. Opt. Soc. Am. A **24**, B42–B51 (2007).

102. N. Doble, D. T. Miller, G. Yoon, and D. R. Williams, "Requirements for discrete actuator and segmented wavefront correctors for aberration compensation in two large populations of human eyes," Appl. Opt. **46**, 4501–4514 (2007).

103. A. Kumar, L. M. Wurster, M. Salas, L. Ginner, W. Drexler, and R. A. Leitgeb, "*In-vivo* digital wavefront sensing using swept source OCT," Biomed. Opt. Express **8**, 3369–3382 (2017).

104. D. Hillmann, H. Spahr, C. Hain, H. Sudkamp, G. Franke, C. Pfäffle, C. Winter, and G. Hüttmann, "Aberration-free volumetric high-speed imaging of *in vivo* retina," Sci. Rep. **6**, 35209 (2016).

105. Z. Liu, O. P. Kocaoglu, and D. T. Miller, "In-the-plane design of an off-axis ophthalmic adaptive optics system using toroidal mirrors," Biomed. Opt. Express **4**, 3007–3030 (2013).

106. O. P. Kocaoglu, T. L. Turner, Z. Liu, and D. T. Miller, "Adaptive optics optical coherence tomography at 1 MHz," Biomed. Opt. Express **5**, 4186–4200 (2014).

107. B. A. Shafer, J. E. Kriske, O. P. Kocaoglu, T. L. Turner, Z. Liu, J. J. Lee, and D. T. Miller, "Adaptive-optics optical coherence tomography processing using a graphics processing unit," 36th Ann Int Conf IEEE Eng. Med. Biol. Soc. 3877–3880 (2014).

108. M. Guizar-Sicairos, S. T. Thurman, and J. R. Fienup, "Efficient subpixel image registration algorithms," Opt. Lett. **33**, 156–158 (2008).

109. R. S. Jonnal, O. P. Kocaoglu, Q. Wang, S. Lee, and D. T. Miller, "Phase-sensitive imaging of the outer retina using optical coherence tomography and adaptive optics," Biomed. Opt. Express **3**, 104–124 (2012).

110. "Cone, rod," https://commons.wikimedia.org/wiki/File:Cone_rode.svg.

111. P. Pande, Y.-Z. Liu, F. A. South, and S. A. Boppart, "Automated computational aberration correction method for broadband interferometric imaging techniques," Opt. Lett. **41**, 3324–3327 (2016).

112. M. Gu, C. J. R. Sheppard, and X. Gan, "Image formation in a fiber-optical confocal scanning microscope," J. Opt. Soc. Am. A **8**, 1755–1761 (1991).

113. P. Bedggood, M. Daaboul, R. Ashman, G. Smith, and A. Metha, "Characteristics of the human isoplanatic patch and implications for adaptive optics retinal imaging," J. Biomed. Opt. **13**, 24007–24008 (2008).

114. Z. Liu, O. P. Kocaoglu, T. L. Turner, and D. T. Miller, "Modal content of living human cone photoreceptors," Biomed. Opt. Express **6**, 3378–3404 (2015).

115. S.-H. Lee, J. S. Werner, and R. J. Zawadzki, "Improved visualization of outer retinal morphology with aberration cancelling reflective optical design for adaptive optics optical coherence tomography," Biomed. Opt. Express **4**, 2508–2517 (2013).

116. Z. Liu, O. P. Kocaoglu, and D. T. Miller, "3D imaging of retinal pigment epithelial cells in the living human retina," Invest. Ophthalmol. Vis. Sci. **57**, OCT533-OCT543 (2016).

117. J. W. Goodman, *Introduction to Fourier Optics*, 3rd ed. (Roberts & Company, 2004).

118. C. A. Curcio, K. R. Sloan, R. E. Kalina, and A. E. Hendrickson, "Human photoreceptor topography," J. Comp. Neurol. **292**, 497–523 (1990).

119. ANSI Z80.28, *Methods of Reporting Optical Aberrations of Eyes* (2004).

120. H. Hofer, P. Artal, B. Singer, J. L. Aragón, and D. R. Williams, "Dynamics of the eye's wave aberration," J. Opt. Soc. Am. A **18**, 497–506 (2001).

121. A. Facomprez, E. Beaurepaire, and D. Débarre, "Accuracy of correction in modal sensorless adaptive optics," Opt. Express **20**, 2598–2612 (2012).

122. L. Mariotti and N. Devaney, "Performance analysis of cone detection algorithms," J. Opt. Soc. Am. A **32**, 497–506 (2015).

123. K. Y. Li and A. Roorda, "Automated identification of cone photoreceptors in adaptive optics retinal images," J. Opt. Soc. Am. A **24**, 1358–1363 (2007).

124. J. Porter, H. Queener, J. Lin, K. Thorn, and A. Awwal, eds., *Adaptive Optics for Vision Science* (Wiley, 2006).

125. J. Zeng, P. Mahou, M.-C. Schanne-Klein, E. Beaurepaire, and D. Débarre, "3D resolved mapping of optical aberrations in thick tissues," Biomed. Opt. Express **3**, 1898–1913 (2012).

126. S. W. Anzengruber, S. Bürger, B. Hofmann, and G. Steinmeyer, "Variational regularization of complex deautoconvolution and phase retrieval in ultrashort laser pulse characterization," Inverse Probl. **32**, 35002 (2016).

127. R. A. Muller and A. Buffington, "Real-time correction of atmospherically degraded telescope images through image sharpening," J. Opt. Soc. Am. **64**, 1200–1210 (1974).

128. R. G. Paxman and J. C. Marron, "Aberration correction of speckled imagery with an image-sharpness criterion," Proc. Spie Stat. Opt. **976**, 37–47 (1988).

129. R. Leitgeb, C. K. Hitzenberger, and A. F. Fercher, "Performance of Fourier domain vs. time domain optical coherence tomography," Opt. Express **11**, 889–894 (2003).

130. P. K. Murphy, J. P. Allebach, and N. C. Gallagher, "Effect of optical aberrations on laser speckle," J. Opt. Soc. Am. A **3**, 215–222 (1986).

131. D. Kang, E. Clarkson, and T. D. Milster, "Effect of optical aberration on Gaussian laser speckle," Opt. Express **17**, 3084–3100 (2009).

132. L. Gagnon and A. Jouan, "Speckle filtering of SAR images: A comparative study between complex-wavelet-based and standard filters," in (1997), Vol. 3169, pp. 3112–3169.

133. J. P. McGuire and R. A. Chipman, "Polarization aberrations. 1. Rotationally symmetric optical systems," Appl. Opt. **33**, 5080–5100 (1994).

134. M. Carl, "Influence of polarization aberrations on point images," J. Opt. Soc. Am. A **34**, 967–974 (2017).

135. A. L. Sokolov, "Matrix method for calculating polarization aberrations," J. Opt. Technol. **75**, 79–84 (2008).

136. K. Crabtree, *Polarization Critical Optical Systems: Important Effects and Design Techniques* (2007).

137. J. B. Jonas, U. Schneider, and G. O. H. Naumann, "Count and density of human retinal photoreceptors," Graefe's Arch. Clin. Exp. Ophthalmol. **230**, 505–510 (1992).

138. S. G. Adie, T. R. Hillman, and D. D. Sampson, "Detection of multiple scattering in optical coherence tomography using the spatial distribution of Stokes vectors," Opt. Express **15**, 18033–18049 (2007).